Aggregation of Hybrid Molecules and Film Formation of Colloidal Monolayers

Dissertation

zur Erlangung des Grades
"Doktor der Naturwissenschaften"

am Fachbereich Chemie, Pharmazie und Geowissenschaften
der Johannes Gutenberg-Universität Mainz

Ting Liu
geboren in Heilongjiang (V. R. China)

Mainz – 2011

Dekan:

1. Berichterstatter:

2. Berichterstatter:

Datum der mündlichen Prüfung: 08. Dezember 2011

D77

For my parents

我的父母

“I was born not knowing and have had only a little time to change that here and there.”

Richard Feynman

Contents

1 Introduction and Motivation

Soft matter refers to a class of materials which display mechanical behavior between that of viscous fluids and elastic solids. Soft matter materials are considered “soft” since generally they can be deformed or induced to flow easily at room temperature. Their softness is due to relatively weak interactions between their building blocks.[1] Classical soft matter systems, which have been thoroughly investigated in the last two decades, are dispersions of colloids, amphiphilic molecules and polymers. Compared to classical solids and liquids, which consist of building blocks on the atomic or molecular scale, the components involved in soft matter are a few nanometers to up to a few micrometers in size and thus four to seven orders of magnitude larger than mere atoms or small molecules.

An important characteristic of soft materials is that their molecular kinetic energy is close to the thermal energy k_BT (around 10^{-20} J) at ambient temperature. The weak interactions between the building blocks of soft matter such as van der Waals forces (around 10^{-20} J) and hydrogen bonds ($2\text{-}6\times10^{-20}$ J) are in the same range.[2] The interactions between the molecules, which either hold them together or separate them, can be easily broken, e.g. by small variation of the temperature. As such, entropy is the quantity that should be considered first in soft matter systems. At ambient temperature, systems consisting of soft matter tend to reduce the order of the system, and hence to increase its entropy and minimize the system’s free energy. One consequence of the so called “entropy effect” is the hydrophobic effect.

The term "hydrophobic effect" refers to the phenomenon of aggregation of hydrophobic molecules in aqueous solution and can be understood by taking into account the formation of hydrogen bonds between water molecules (Figure 1). The electronegative oxygen atom attracts the electron cloud around the hydrogen nucleus and leaves the hydrogen atom with a positive partial charge (δ+), which can interact with the negative partial charge of an oxygen atom in another water molecule, thus forming a hydrogen bond by way of electrostatic attraction $\mathrm{O{-}H\cdots O}$. Inserting hydrophobic molecules into water breaks the hydrogen bonding network between water molecules. By arranging water molecules around the hydrophobic molecule as a “cage”, the hydrogen bonds are partially rebuilt. However, the mobility of the water molecules in the “cage” is substantially restricted. This process reduces the entropy of these water molecules and is therefore unfavorable to the free energy of the system. Therefore, hydrophobic molecules tend to assemble together in such a way as to reduce the contact area between the hydrophobic and hydrophilic phases.

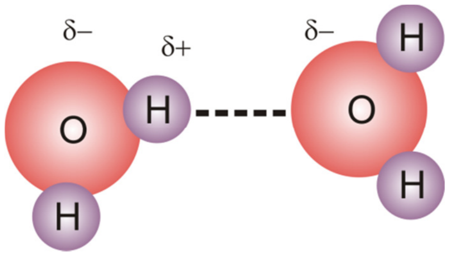

Figure 1: Illustration of a hydrogen bond between two water molecules when a hydrogen atom is covalently bonded to an electronegative atom such as nitrogen, oxygen and fluorine.

Amphiphilic molecules have a hydrophobic part and a hydrophilic part. They self-assemble into micelles when the concentration of the molecules exceeds a critical value, the "critical micelle concentration" (CMC). In aqueous solution, the hydrophobic parts aggregate and form the centers of the micelles to avoid contact with the water phase. The hydrophilic parts of the molecules form the shells and have direct contact with the surrounding water molecules. Although micelle formation also induces a decrease of entropy by ordering the amphiphilic molecules, more entropy is gained by releasing water molecules from the “cages” around the hydrophobic parts. The gain in entropy is large enough to compensate the entropy loss from aggregation and is sufficient to reduce the free energy of the solution.

Hydrogen bond formation is one of the important forces for retaining the double helix structure of deoxyribonucleic acid (DNA). DNAs are long, strand-like molecules which are constituted of linear polymer backbones formed by alternating phosphate and sugar groups, and by four different types of bases, one of which is attached to each sugar moiety (Figure 2). The four bases are adenine (A), thymine (T), guanine (G) and cytosine (C) and they encode the genetic information.

Hydrogen bonds may form only between bases A and T as well as between G and C. The respective moieties forming base pairs are called complementary. Between A and T, two hydrogen bonds, $N-H\cdots O$ and $N-H\cdots N$, can be generated (Figure 2). Between G and C, three hydrogen bonds can form, two of which are $N-H\cdots O$ and the third one is $N-H\cdots N$.

The combination of non-complementary bases does not lead to pair formation. Likewise, a single strand (ss) of DNA can pair with another strand of DNA when their sequences are complementary to each other (Figure 2). In such double stranded (ds) DNA, the base pairs connect both single DNA strands like rungs in a rope-ladder, and the double stranded molecule adopts the shape of a double helix.

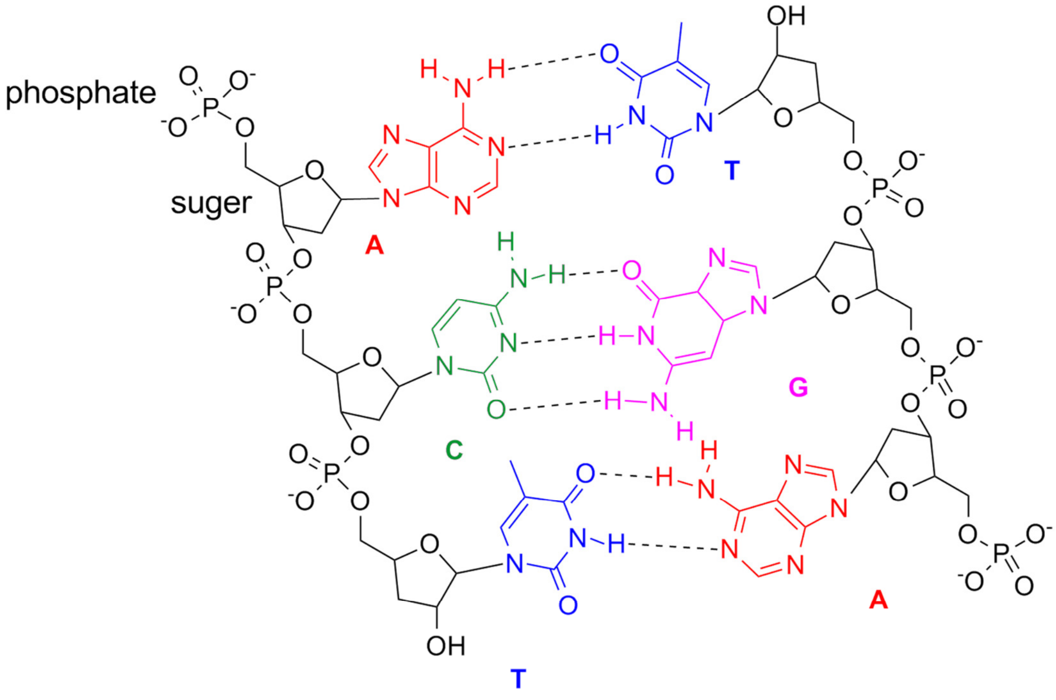

Figure 2: Structures of DNA with bases adenine (A), thymine (T), guanine (G), and cytosine (C) and the base paring between A and T via two hydrogen bonds, and between G and C via three hydrogen bonds.

This ability of DNAs to be paired (hybridized) with their complementary sequence has allowed the construction of a wide range of DNA nanostructures. For instance, Seemann and coworkers were able to produce branched DNA molecules by appropriately designing the sequences of single stranded (ss) DNA.[3] By means of extending individual ssDNAs beyond the end of the double helix structures, “sticky” ends can be produced that specifically stick to complementary ends. Such “sticky” ends can guide the pairing of DNA molecules into even more complex supramolecular structures, such as polyhedra, knots and networks.[4]

1.1 DNA Hybrid Materials

In the first part of my thesis I investigate molecules which are designed to allow formation of supramolecular structures both by hybridization and aggregation due to the hydrophobic effect. These molecules are conjugates of DNAs and synthetic polymers.[5] The so-called DNA block copolymers are mostly amphiphilic in nature, since the DNAs are hydrophilic and the polymers are commonly hydrophobic. Both the DNA blocks and the polymer blocks can be designed in every desired form. The sequences and the length of the DNA can be varied since they can be built step by step from synthetic oligodeoxynucleotides (ODN) via solid phase DNA synthesis. Polymer blocks with different lengths and units can also be synthesized.

Driven by the hydrophobic interaction, DNA block copolymers can also form complex structures such as bilayers, vesicles or micelles, which may exhibit spherical or cylindrical shape.[6] Conjugates of ssDNA and polystyrene (PS) are found to assemble into spherical micelles with hydrophobic polymer cores and hydrophilic ssDNA shells in aqueous solution. The existence of the micelles was verified by Scanning Force Microscopy (SFM).[7]

The shape and the size of DNA block copolymer micelles can be tuned by varying the nature of the DNA- and polymer blocks. For instance, DNA can be used in the more flexible, single stranded form (persistence length: a few nanometers[8]) or in the more rigid double stranded form (persistence length: 35 nm[9]). The length of the hydrophilic DNA block can be adjusted by varying the number of nucleotide units.

The properties of the polymer part can be tuned by using different polymers such as polypropylene oxide (PPO), polyethylene oxide (PEO) or poly(N-isopropylacrylamide) (PNIPAAM) which can be linked to the DNA covalently. Additionally, polymers with different molecular weights or with linear or branched structures can be used.

As for the spherical micelles formed from block copolymers of ssDNA and polypropylene oxide (ssDNA-*b*-PPO), the shape of micelles can be tailored subsequently by hybridizing the ssDNA blocks with different complementary DNA templates (Figure 3).[7b, 7c] Hybridization of ssDNA-*b*-PPO micelles with short DNA strands of complementary sequences yields micelles with a dsDNA corona, maintaining a spherical shape (Figure 3a). Hybridization of the same micelles with long complementary DNA templates, on the other hand, results in aggregates with rod-like structures (Figure 3b). It is also possible to manipulate the shape and size of already existing micelles by subsequent treatment with enzymes,[7d, 10] which can either cleave the DNA chains or elongate them by addition of bases. These micelles have found application as three dimensional scaffolds for DNA-templated organic reactions[11], in gene and drug delivery systems[12], in the purification of biomaterials[13], and in the detection of DNA by means of hybridization.[14]

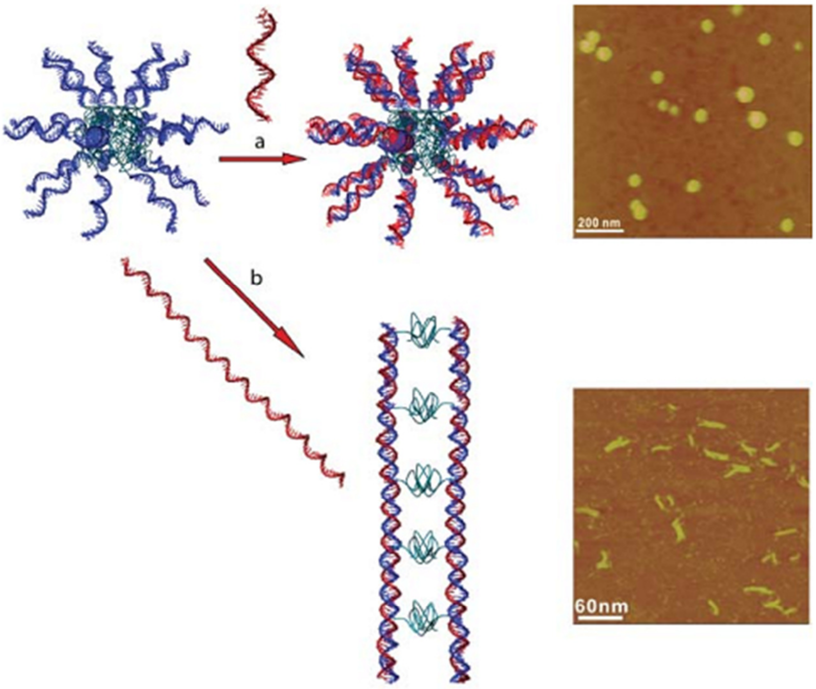

Figure 3: Scheme for hybridization of ssDNA-*b*-PPO with complementary DNAs, which yields micelles in different shapes and the corresponding SFM images.[7b, 7c]

In **Chapter** 3 (**FCS Study of DNA Hybrid Micelles**), I investigate whether it is possible to apply this strategy to tailor the shape of micelles based on a conjugate of perylenediimide (PDI) and DNA (DNA-PDI). PDI is a fluorophore with an aromatic planar structure. Due to its structure and aromaticity, it can interact with other PDIs via π–π interaction and form stacks. This interaction enables the formation of intermolecular structures of DNA-PDI as sketched in Figure 4. PDI also has high photo stability and high fluorescence quantum yield.[15] Hence, the DNA-PDIs can be directly tracked in the solution by exciting and detecting the PDI fluorescence. I study the shape of aggregates formed from dsDNA-PDI in aqueous solution by means of fluorescence correlation spectroscopy (FCS, introduced in chapter 2). In particular, the question whether aggregates with dimeric structure can be generated by using a strategy similar to that shown in Figure 3b is addressed (Figure 4).

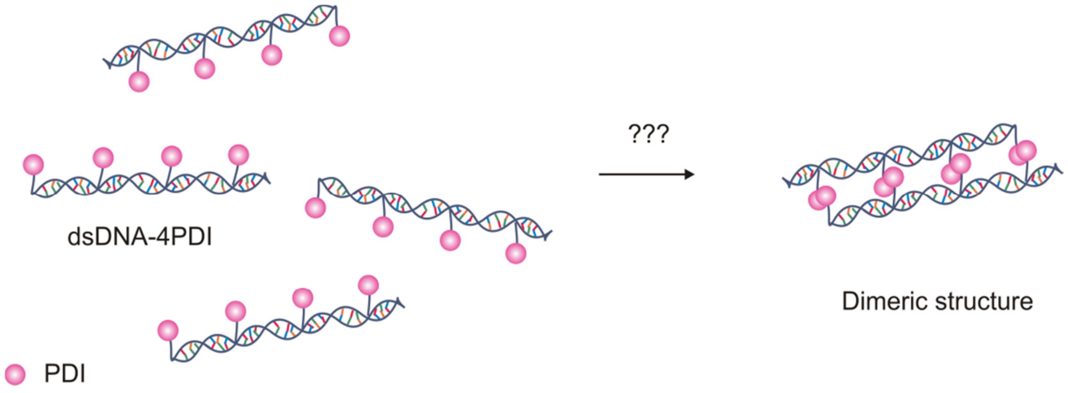

Figure 4: Illustration of the question: is it possible to tailor the structure of the aggregates of DNA-PDI?

FCS is a powerful tool to study the diffusion of newly designed hybrid materials in solution. Very small quantities of newly designed molecules (a few nanomoles to picomoles) are sufficient to perform the measurements. FCS is also a complementary technique to SFM. Characterization with SFM requires immobilizing hybrid materials on surfaces and is time consuming, especially when the measurement is carried out in solution. In addition, an exact size estimation of the micelles via SFM is not an easy task due to tip convolution, which occurs when the micelles have sizes smaller than the tip curvature (20-30 nm).[7d] The solution-based FCS technique has the advantage that the sample preparation only requires dissolving the molecules of interest in aqueous solution. The measurement takes only about 5 minutes. The size assessment is based on the diffusion coefficient of the molecules.

Micelles are generally dynamic structures since single amphiphilic molecules enter and exit the micelles continuously. The residence time of an amphiphilic molecule in a micelle is strongly dependent on the length of its hydrophobic part. The residence time of surfactant molecules with a short hydrophobic part (hydrocarbon chain with 5~20 carbon atoms) is in the range of 10^{-8}~10^{-6} s.[16] Block copolymers with long hydrophobic parts (hydrocarbon chains with about 10000 carbon atoms) have residence times of about 10^{3} s.[17] The average residence time of unimers plays an important role for the formation and dissociation of micelles and is of interest for the application of micelles in dispersant technology and controlled drug release.[18] In **Chapter** 4 (**FCCS Study of Size and Residence Time of DNA-b-PPOs**) I develop a strategy to estimate the residence time of DNA-*b*-PPO in a micelle by means of fluorescence cross-correlation spectroscopy (FCCS).

1.2 Polymeric Colloidal Monolayer

In the second part of my thesis, I investigate colloidal monolayers deposited on a micromechanical cantilever. A micromechanical cantilever coated with an active layer can be used as a sensor to detect target molecules. Here, the active layer refers to a molecular layer with considerable affinity for the target molecules. Polymer layers have often been used as active layers for micromechanical cantilevers to detect various organic solvent vapors and other target molecules.[19] Upon absorption or adsorption of target molecules, the elasticity and the mass of the polymer layer changes, which in turn induces a physical change, such as a deflection of the cantilever (Figure 5a) or in a shift of its resonance frequency (f_1-f_0, Figure 5b).

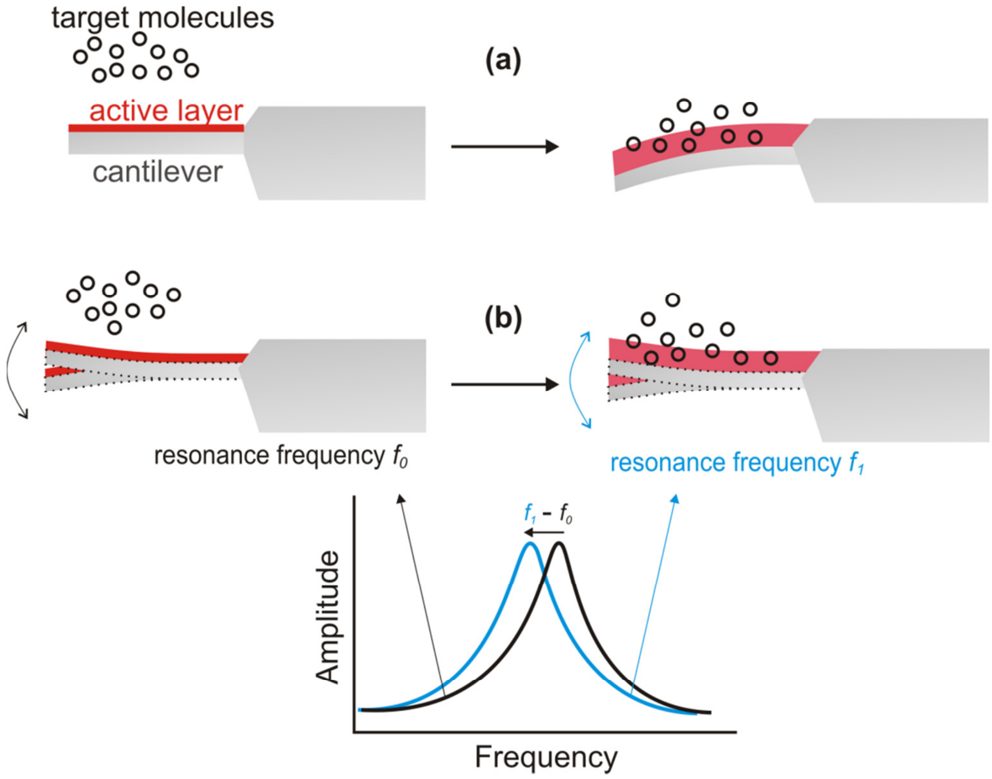

Figure 5: Schematic drawing of the work principle of a cantilever as sensor to detect target molecules: (a) deflection (b) resonance frequency shift as the physical change of cantilever upon absorption/adsorption the target molecules in the active layer.

It has been predicted that the sensitivity of cantilevers to the change of the elasticity of the coating layer will be enhanced by thicker coating layers.[20] According to a finite element (FE) analysis, greatest sensitivity occurs at a polymer to silicon thickness ratio of two,[21] which means that polymer coating films of a few microns thickness are required.

Coating the micromechanical cantilever with thick polymer films is challenging due to its small surface (length: a few hundred nanometers, width: less than one hundred nanometers). Classical coating methods such as spin coating cannot be used since the rotation damages the fragile cantilever. Other method such as inkjet printing has been developed to functionalize the cantilever with polymer films.[22] However, the resulting films are not homogenous (Figure 6). They are thicker at the edge and thinner in the center because of the solvent drying effect.[22b]

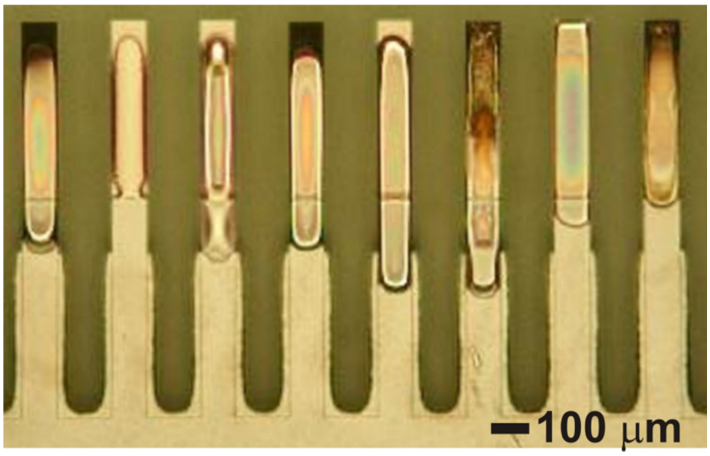

Figure 6: Optical microscope image of cantilevers coated with different polymers by inkjet printing of dilute solutions.[22b]

In **Chapter** 5 (**Coating Cantilever with Colloidal Monolayer**), I take the approach to coat the cantilevers with colloidal monolayers. Polymer colloids are mostly synthesized by miniemulsion[23] and emulsion polymerization.[24] These colloids are chosen as starting materials to coat the cantilevers owing to their sizes in range of tens of nanometers to several micrometers, which corresponds to the desired thickness of the active layer. In addition, these colloids can undergo self-assembly and form two dimensional arrays of hexagonally packed colloids once they are brought to the air/water interface.[25] Due to the wetting of colloids, the interface between the air and water is deformed and a meniscus is formed at the interface between colloids, air and water (Figure 7). Upon driving the colloids to a close-packed monolayer (Figure 7a-b), the total area of meniscus and thus the surface energy is minimized.[26]

Figure 7: (a) Meniscus formation at the colloid, air and water interface. (b) The total meniscus decrease due to the formation of closely packed colloids.

Colloidal monolayers have drawn attentions due to their great potentials for coating applications. Homogenous polymer films can be formed from polymeric colloidal monolayers either via thermal annealing or organic vapor annealing.[27]

In **Chapter** 6 I focus on the film formation from colloidal monolayers coated on the micromechanical cantilevers by means of thermal and organic vapor annealing. During the film formation, the elasticity of the colloidal layer and the contact between the coating layer and cantilever change. In addition, the mass of the film also varies during organic vapor annealing. Can the cantilever sense these changes in the coating layer (Figure 8a)? If yes, how do these changes evolve during the film formation? And do these changes exhibit the same development during both annealing processes? After the film formation is complete, is it possible to characterize the resulting film? Do the films formed by thermal annealing and organic vapor annealing have the same elastic properties? In which direction does the cantilever bend during the film formation (Figure 8b)? These questions are addressed in **Chapter** 6 (**Film Formation of Colloidal Monolayers on a Micromechanical Cantilever**).

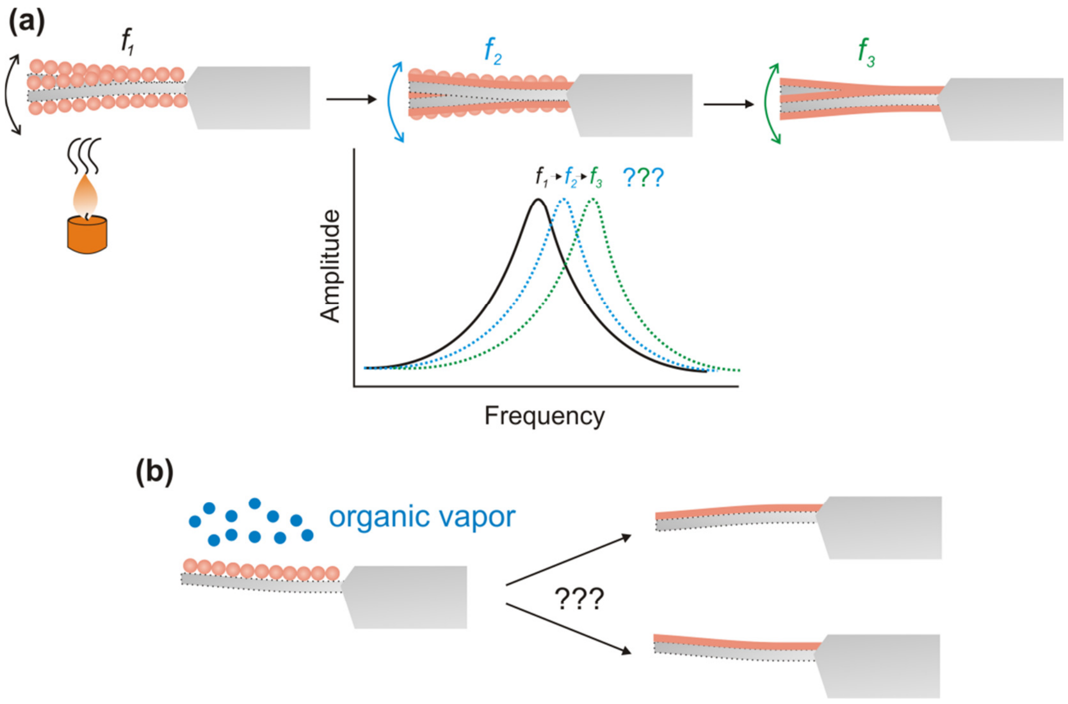

Figure 8: Illustration of the addressed question: (a) is it possible to sense the change of the coating layer during film formation? Can the evolution of the film formation be monitored? (b) In which direction does the cantilever bend?

In the last part of my thesis (**Chapter** 7**: Polymeric Functionalized Cantilevers as Glucose Detectors**), I demonstrate the sensing ability of a micromechanical cantilever functionalized with an active polymer layer for detecting glucose. Here, cantilevers are coated with polymer brushes incorporated with phenylboronic acid (PBA) moieties. PBA can bind glucose via ester formation. Monolayers of PBA are also coated on the cantilevers. The deflection of these two differently functionalized cantilevers upon binding glucose will be measured and compared.

The description of all the experimental and methods can be found in **Chapter** 8 (**Experimental**). At the end I give some summary and conclusion for the future projects (**Chapter 9**).

2 Theory and Methods

In this chapter, I introduce the work principle and the theoretical background for fluorescence correlation spectroscopy (FCS), fluorescence cross-correlation spectroscopy (FCCS) and cantilever sensors in both dynamic and static mode.

2.1 Fluorescence Correlation Spectroscopy

Fluorescence correlation spectroscopy (FCS) was first introduced in 1972 by Magde, Elson, and Webb[28] by monitoring the fluorescence fluctuations in the binding of ethidium bromide (a fluorescent dye) to a deoxyribonucleic acid (DNA). This technique has been further developed and the theory has been established in the 1990s. Nowadays, FCS has been qualified as a very sensitive method to characterize biomolecules in extremely low concentration.

The concept of FCS is to correlate the fluctuation of the fluorescent signals emitted from fluorophores passing through a small focused laser beam spot also called as observation volume in the size of only a few femtoliters (fl). The small observation volume as well as a low concentration of fluorophores is important to yield good signal-to-noise ratios and thus to ensure the single molecule detection. The correlation curve can be analysed to yield the average particle number in the observation volume and the average diffusion time (residence time), which is the time a molecule needs to move through the observation volume.

FCS has already been used to study binding of DNA,[29] ligand-receptor interaction,[30] binding of substrate molecules to the cell membrane in living cell,[31] interaction between membrane receptor and protein.[32] For instance, Kinjo and Rigler were able to monitor the hybridization of a fluorescently labelled short DNA with 18 bases with a larger DNA with 7530 bases containing complementary sequences.[29a] Upon hybridization, the labelled species became larger and the diffusion time of the species through the observation volume became longer. The increase in diffusion time is evidence of the hybridization. Recently, FCS was also used to study micelle formation of amphiphilic copolymers.[33] Similarly as above, the amphiphilic copolymers were labelled with fluorescent dyes. Upon micelle formation, the diffusion of the labelled species became slower and thus, the existence of the micelles can be confirmed by FCS and the size of the micelle can be estimated.

Other techniques used to study micelles of block copolymers are scanning force microscopy (SFM), dynamic and static light scattering (DLS and SLS)[34] and fluorescence resonance energy transfer (FRET).[35] SFM is able to visualize micelles on a surface down to the nanometer scale without labeling the molecules, but it limits the investigation of micelles in a very small volume. Normally SFM is carried out for an area of 1×1 μm^2 on a mica or graphite surface. DLS and SLS can provide information about the diffusion (and thus size) and the geometry of micelles. The required amount of molecules for DLS and SLS is in the micromole range,[36] which is challenging because the yields of newly designed bioorganic materials are typically very low. Using FRET, formation and degradation of micelles in the solution can be monitored in real time.[35]However, to enable the investigation of molecules via FRET, they firstly have to be labeled with two different kinds of fluorophores, a donor and an acceptor, whose emission (donor) and absorption spectra (acceptor) overlap. In addition, the distance between the two flurophores has to be in the range of 1 to 10 nm to enable sufficient energy transfer. Those requirements limit the applicability of FRET to only specifically labeled species.

In contrast to the above mentioned methods, FCS offers direct investigation of the molecules in solution with only a small demand (nanomoles) for sample molecules. Meanwhile, the required fluorescence labeling of the target molecule is not as sophisticated as for an investigation using FRET and are commercially available.

2.1.1 Fluorescence Process

Fluorescence process describes the absorption of light energy (photon) by certain molecules at one wavelength and its re-emission at another wavelength. These molecules are called fluorophores or fluorescent dyes. The fluorescence process involves three processes, which can be well described by Jablonski diagram; a diagram illustrates the electronic states of molecules (Figure 9a). In the first step, the molecule in the ground state S_0 absorbs one photon and enters to an excited electronic state S_1' with higher energy level. In the second step, the exited molecule transfers its thermal energy to the surroundings and takes the relaxed excited state S_1. The exited state is normally occupied for an average time of 0.1-10 ns. In the third step, the molecule emits a photon from the relaxed excited state S_1 and inverts to the ground state S_0.

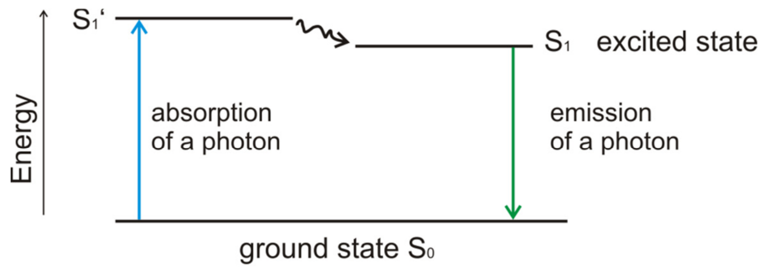

(a)

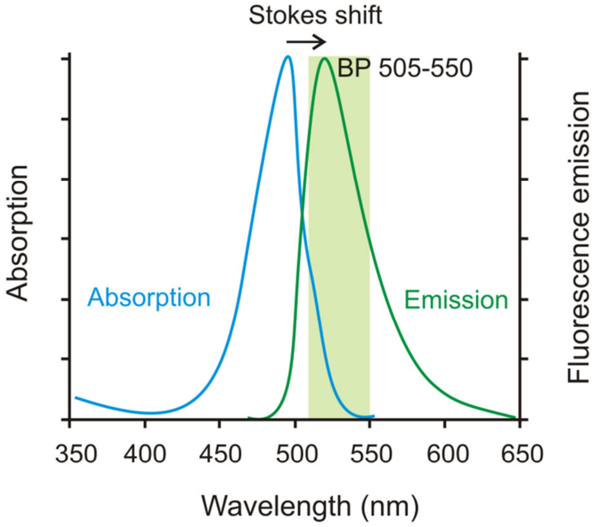

(b)

Figure 9: (a) The Jablonski diagram illustrates the three processes involved fluorescence; (b) the absorption and emission spectrum of Alexa488 and the band pass BP505-550.

Due to the energy loss at the exited state, the energy of emitted photon is always lower than that of the absorbed photon. Therefore the wavelength of emitted light shifts to a longer wavelength compared to the absorbed light. Taking the dye Alexa488 as example, the absorption maximum is at 499 nm and emission maximum is at 519 nm (Figure 9b). This so called Stokes shift can be used to separate the emission light from the excitation light by means of an optical filter. Alexa488 can be efficiently excited at 488 nm and a bandpass BP505-550 is a good filter, since light with wavelength between 505 and 550 nm will be collected without disturb signal from the excitation light. Besides the bandpass, long-pass filter is also widely utilized; in this case light above a certain wavelength is collected.

2.1.2 Fluorescence Correlation Spectroscopy

The FCS setup is schematically illustrated in Figure 10. The laser beam is directed into a numerical aperture objective with a dichroic mirror and focused on the sample solution. The light emitted by the samples is collected by the same objective and passes through the dichroic mirror, so that the excitation light is reflected and only the emitted light from the sample is transmitted. The emitted light is filtered by a band pass filter or a long pass filter to block the light not in the emission wavelength. The filtered light is then focused by a lens onto a confocal pinhole to reach finally the detector, an avalanche photodiode (APD) operated in the photon counting mode.

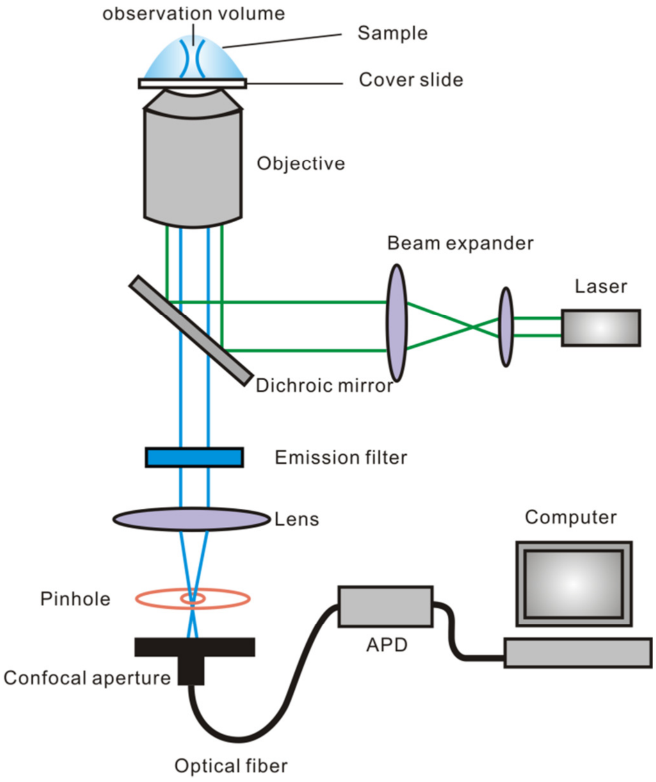

Figure 10: Illustration of a FCS setup.

The profile of the confocal observation volume *V* can be described as an ellipse with *z* and ω as the radial and axial half axes (Figure 11a). The radius of the observation volume ω is related to the wavelength λ_0 of the laser and the numerical aperture *NA* of the optic objective:

$$\omega = \frac{\lambda_0}{2\pi \cdot NA} \tag{2.1}$$

Observation volume *V* can be described with the following equation:

$$V = \pi^{3/2} \cdot \omega^2 \cdot z \tag{2.2}$$

For a regular FCS measurement, ω and *z* takes value of about 0.2 µm and 1 µm, yielding an extreme small observation volume with dimension of about 10^{-15} L (fL).

The signal fluctuation induced by fluorescence species diffusing in and out of the observation volume is recorded as $F(t)$ (Figure 11b). The fluorescence signal $F(t)$ is then correlated to itself $F(t+\tau)$ with a lag time τ to create the autocorrelation curve $G(\tau)$ (Figure 11c). The autocorrelation function is mathematically defined with as follows

$$G(\tau) = \frac{\langle F(t)F(t+\tau)\rangle}{\langle F(t)\rangle^2} \tag{2.3}$$

To track the movement of a single molecule, it is essential that there are only a few molecules in the observation volume, which can be realized by keeping the concentration of the molecules low. An ideal concentration is between nanomolar (10^{-9} M) and micromolar (10^{-6} M). In an observation volume in the range of femtoliter, the amount of labeled molecules is between 1 and 1000.

The autocorrelation curve can be analyzed by a fitting algorithm, which is designed as a mathematical representation of the correlation curve. The values calculated by the algorithm are compared to the autocorrelation curve repeatedly and approximated until the difference between the two curves is minimized.

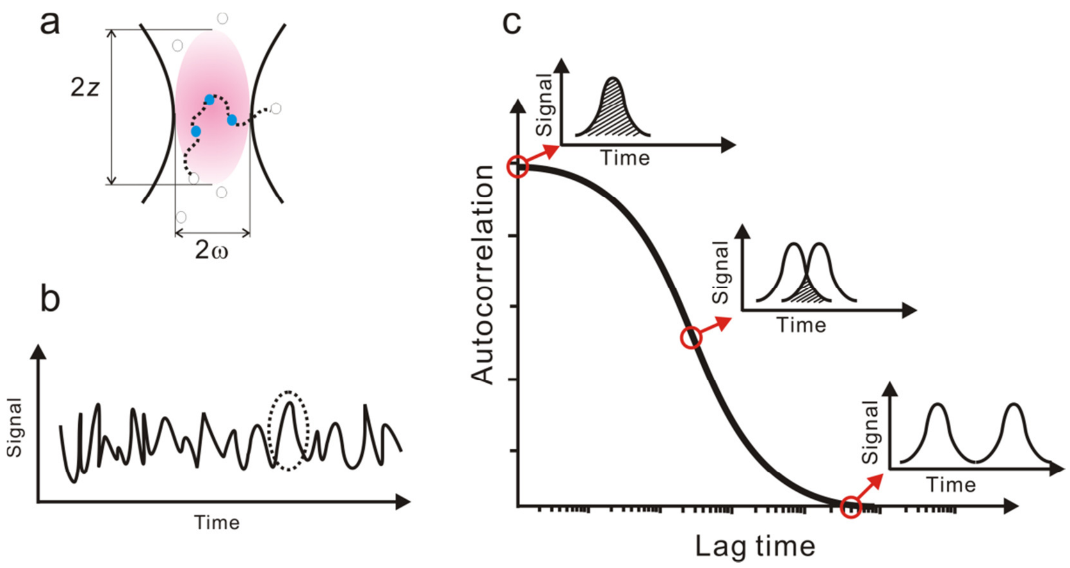

Figure 11: The basic principle of correlation. a) a close-up view of the observation volume; b) the evolution of the fluorescence signal of one dye molecule in the observation volume with time ; c) the autocorrelation function of the fluorescence signals.

For a system contains only one kind of molecules, the diffusion time of these molecules are similar or identical to each other. Such a system can be fitted by a one-component model with one diffusion time. Here, the autocorrelation function can be mathematically analyzed with the following equation (2.4):

$$G'(\tau) = 1 + \frac{1}{N}\left(1 + \frac{t}{\tau_D}\right)^{-1} \cdot \left(1 + \frac{t}{S^2\tau_D}\right)^{-1/2} \qquad (2.4)$$

Where N is the average number of excitable molecules in the observation volume, τ_D the diffusion time, S the structure parameter given by $S=z/\omega$. Knowing N and V, the concentration c of the excitable molecules can be calculated as

$$c = N/V \qquad (2.5)$$

The diffusion time τ_D that a molecule needs to move through the observation volume is related to the diffusion coefficient *D*,

$$\tau_D = \frac{\omega^2}{4D} \tag{2.6}$$

The dimensions of z, ω and thus V are obtained from a calibration measurement with dye molecules, whose diffusion coefficient is already known, such as Rhodamine 6G (Rh6G) for laser 488 nm (D_{Rh6G}=2.8·10^{-10} m^2/s[37]).

When there are two types of fluorescent molecules in the solution, for instance labeled macromolecules and the dye molecules, they may have different diffusion behaviours for instance different residence time in the observation volume. Therefore, the measured autocorrelation contains information for both different molecules and needs to be fitted by a corrected function. A weighted sum model of two single components with different diffusion times can be used:

$$G'(\tau) = 1 + \frac{1}{N}\left[\begin{array}{c} Y\left(1+\frac{t}{\tau_{D1}}\right)^{-1}\left(1+\frac{t}{S^2\tau_{D1}}\right)^{-1/2} + \\ (1-Y)\left(1+\frac{t}{\tau_{D2}}\right)^{-1}\left(1+\frac{t}{S^2\tau_{D2}}\right)^{-1/2} \end{array}\right] \tag{2.7}$$

Here, Y is the fraction of particles with diffusion time τ_{D1} and 1-Y is the fraction of the particles with diffusion time τ_{D2}.

For a globular molecule with hydrodynamic radius *r* the diffusion coefficient *D* is given by the Stokes-Einstein equation:

$$D = \frac{k \cdot T}{6 \cdot \pi \cdot \eta \cdot r} \tag{2.8}$$

Where k is Boltzmann constant, *T* the absolute temperature, η the viscosity of the solution and *r* the hydrodynamic radius of the molecule. For globular molecules the diffusion time is proportional to the hydrodynamic radius of the molecule. Since the samples for FCS measurement have very low concentration (10 nM-1 µM) the viscosity of the solution can be mostly considered as the viscosity of the solvent, in this work water.

For molecules with rod-like structures, the diffusion coefficient can be described with the following equation:[38]

$$D_{rod} = \frac{k \cdot T}{3 \cdot \pi \cdot \eta \cdot L} \ln(x + 0.312 + \frac{0.565}{x} + \frac{0.1}{x^2}) \qquad (2.9)$$

where x is the ratio of the molecular length L to its diameter.

2.1.3 Fluorescence Cross-Correlation Spectroscopy

By means of fluorescence cross-correlation spectroscopy (FCCS) measurements samples containing two dyes can be studied. To explain the working principle of FCCS, I name one dye as red dye and the other one blue dye. The samples are excited and detected at two different wavelengths simultaneously by using overlapping laser beams and separated detection pathways (Figure 12a). Only if the two different dyes are tethered to the same molecule, their movements in the solution are cross-correlated to each other (Figure 12b-d). FCCS selectively detects such combined and thus cross-correlated species.[39]

In particular, two laser beams of different wavelength are coupled to generate two superimposed focal spots of excitation laser light in the sample. The lights are reflected by a dichroic mirror towards the microscope objective and focused in the sample. The lights emitted by the samples are collected by the same objective and pass through the dichroic mirror, so that the excitation light is reflected and only the emitted lights are transmitted. The light emitted by the two samples is split by a dichroic mirror. After passing through the filters, the two emission signals are led through the pinholes to clock the emission photons produced outside the laser spot and then focused on two separate APDs operated in the photon counting mode. The cross-correlation of the output signals were calculated by a two-channel correlation in a PC board. Meanwhile, the autocorrelation of the red dye and the blue dye can also be calculated.

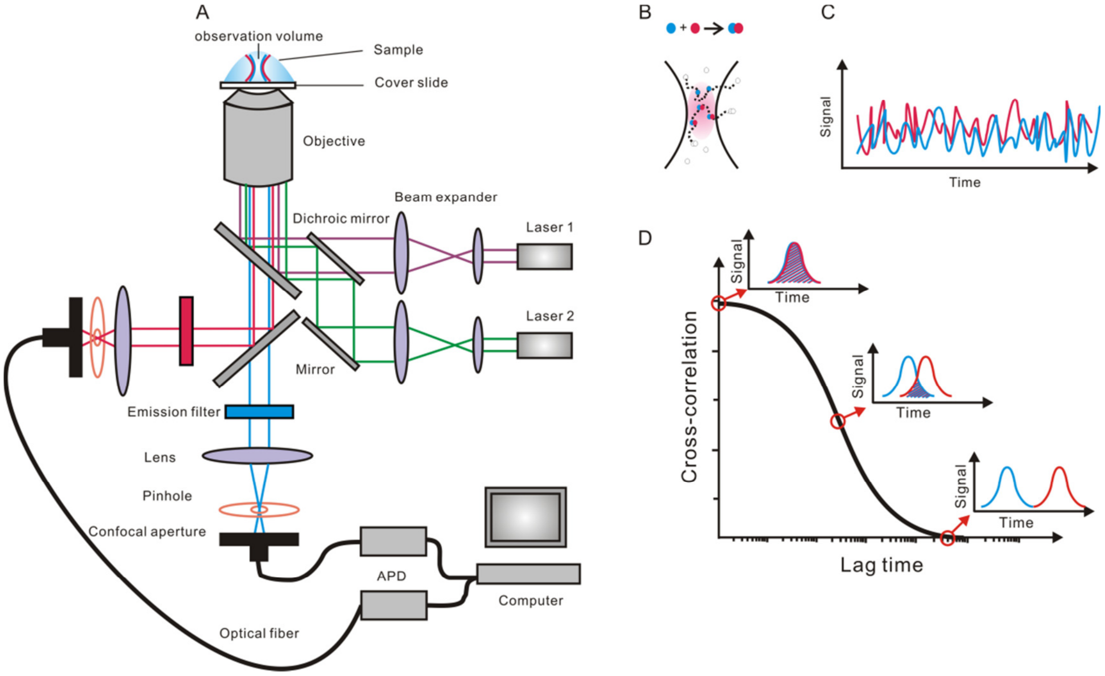

Figure 12: Illustration of FCCS setup and the basic principle of correlation. a) FCCS setup; b) a close-up view of the observation volume; c) the evolution of the Fluorescence signals of two dye molecules, which are linked together; d) the cross-correlation function of the emission signals in both wavelengths.

To perform FCCS properly, the confocal volumes generated by excitation light in both wavelengths have to overlap (Figure 13). The radius of observation volume for laser increases with the wavelength of the laser (equation (2.1)). Ideal for the cross-correlation is the maximal overlap of the two volumes. To adjust the overlap, one dye molecule, which can be excited at both wavelengths, is used. First, the dye molecules are excited at 488 nm and the confocal volume location can be determined with help of the FCS software. Then the dye molecules are excited at 633 nm, the confocal volume location will be compared with the previous one. When the locations of the both confocal volumes are identical, the adjustment of the excitation lights is satisfactory. If not, the pinholes for the both path ways will be adjusted once more till the confocal volume locations are identical.

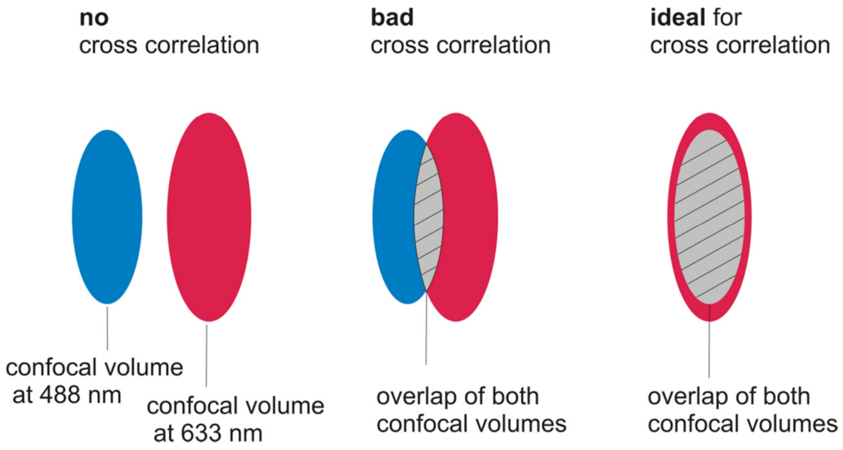

Figure 13: Illustration of two confocal volumes at 488 nm and 633 nm and the ideal overlap of the two volumes for cross-correlation.

The cross-correlation $G_{12}(\tau)$ of fluorescence signals F_1 and F_2 is defined as:

$$G_{12}(\tau) = \frac{\langle F_1(t)F_2(t+\tau)\rangle}{\langle F_1(t)\rangle\langle F_2(t)\rangle} \tag{2.10}$$

The amplitude of the cross-correlation function is directly proportional to the concentration of doubly labeled molecules. The particle number N in the cross-correlation consists of both correlated and uncorrelated species:

$$\frac{1}{N} = \frac{N_{br}}{(N_b + N_{br}) \cdot (N_r + N_{br})} \tag{2.11}$$

N_{br} is the particle number of the molecules with both dyes; N_r and N_b are the particle numbers of molecules labeled with only red dye and blue dyes, respectively. They can be obtained from the autocorrelation of each dye.

2.2 Micromechanical Cantilever

A micromechanical cantilever is a very small spring, mostly in a rectangular form with length L, width w ($w<<L$) and thickness t_s ($t_s<<L$) in dimension of micrometers, mostly made of silicon or silicon nitride. One end of the cantilever is fixed on a chip and the other end is free. Cantilevers are originally an essential part in scanning force microscopy (SFM).[40] For the SFM performance, a sharp tip is attached at the end of the cantilever. In *contact mode*, the cantilever scans over the sample and the surface topography can be generated by the deflection of the cantilever induced by the interaction between sample and tip; in the *tapping*- or *intermittent contact mode*, [41] the cantilever is oscillated close to its resonance frequency slightly above the sample surface. The interaction between the tip and the sample surface can be reflected by the shift of the amplitude or of the resonance frequency the cantilever.

In the early 1990s, it has been found that the cantilevers respond to variation of the ambient, for instance humidity, temperature [42] and chemical vapor,[43] which broadened their applications as chemical sensors. Cantilevers exhibit high sensitivity due to their high surface area to volume ratio. The following up experiments extended the applications of cantilever to detect the surface stress change,[44] mass loading on cantilever [45] and DNA molecules detection via hybridization [46] based on different detection principles. The design of cantilever array (Figure 14) with eight separate cantilevers on one chip enables measurements of cantilever with different coatings simultaneously and gives rise to the application of cantilevers as sensors.[47] Presently, arrays with about 1000 cantilevers are available,[48] which enables even more simultaneous measurements.

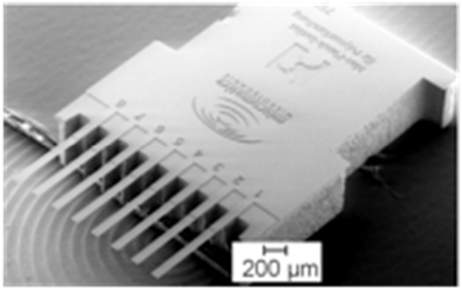

Figure 14: Scanning Electron Microscope (SEM) image of a micromechanical cantilever array with eight cantilevers on one chip.[49]

2.2.1 Dynamic Mode

In the dynamic mode, the resonance frequency of the cantilever is measured. The resonance frequency f_0 of a cantilever is given by [50]

$$f_0 = \frac{1}{2\pi}\sqrt{\frac{k}{nm_0}} \tag{2.12}$$

Here, m_0 is the mass of the cantilever, $n = 0.2427$ is a factor converting a point mass to the real mass of the cantilever in the first vibration mode, and k is the spring constant of the cantilever. For a cantilever with a rectangular cross-section k can be calculated with

$$k = \frac{E_0 w h_0^3}{4L^3} = \frac{3E_0 I_0}{L^3} \tag{2.13}$$

Here, w is the width, h_0 is the thickness, L is the length of the cantilever, E_0 is the *Young's* modulus of the cantilever and $I_0 = wh_0^3/12$ is the moment of inertia. Combining equation (2.12) and (2.13), the following expression can be obtained:

$$f_0 = \frac{1}{2\pi L^2}\sqrt{\frac{3E_0 I_0}{nw\rho_0 h_0}} \tag{2.14}$$

Here, ρ_0 is the density of the cantilever.

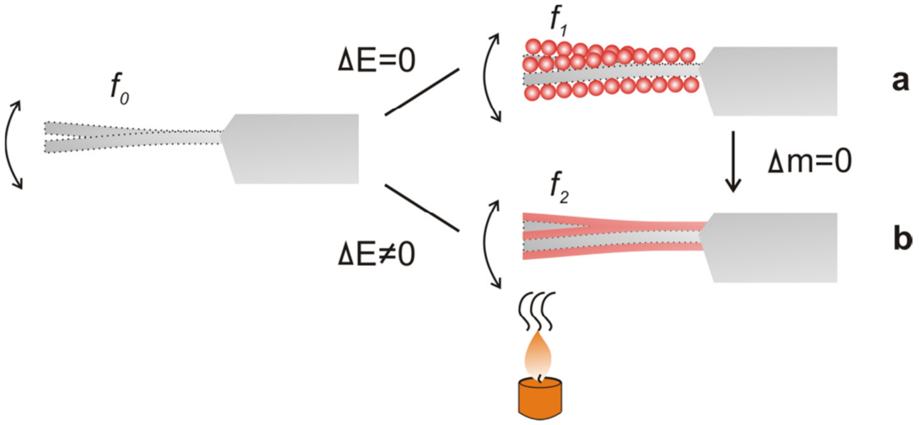

Figure 15: Illustration of work principle the cantilever in dynamic mode. (a) A blank cantilever with resonance frequency of f_0 is coated with a monolayer of particles. Due to the mass of the coating layer the resonance frequency of the cantilever changes to f_1. (b) For the case that the elastic contribution of the coating layer has to be taken into account, for example for the continuous coating film formed after thermal annealing the particles. Here the contact between the coating layer and the cantilever is large enough to couple the polymer elasticity to the spring constant of the cantilever. The resonance frequency of the cantilever shifts from f_1 to f_2, although the mass on the cantilever is constant.

According to equation (2.12) both mass change and elasticity change of cantilever can induce a resonance frequency shift of the cantilever. In the case that only the mass of the cantilever changes, for instance loading the cantilever with resonance frequency of f_0 with a homogeneously distributed layer of thickness h_1 and density ρ_1 on both sides (Figure 15a), the resonance frequency decreases to f_1

$$f_1 = \frac{1}{2\pi}\sqrt{\frac{k}{n(m_0+m_1)}} = \frac{1}{2\pi L^2}\sqrt{\frac{3E_0 I_0}{nw(\rho_0 h_0 + 2\rho_1 h_1)}} \qquad (2.15)$$

The added mass m_1 can be determined by measuring the different resonance frequencies by combining equations (2.12) and (2.15):

$$m_1 = \frac{k}{4n\pi^2}\left(f_0^{-2} - f_1^{-2}\right) \qquad (2.16)$$

Equation (2.16) is valid under the condition that the spring constant k of the cantilever does not change upon the mass loading of m_1. This is a valid assumption if the *Young's* modulus of the cantilever material E_0 is much higher than the *Young's* modulus of the material added E_1 (Figure 11a) or if the coating layer is very thin compared to the cantilever. We will use the relation to calculate the mass added by coating the cantilever with a monolayer of particles which are not connected.

For the case that the elastic contribution of the coating layer has to be taken into account (Figure 15b), supposing that a cantilever is coated on both sides with homogenous layers, which have a thickness of h_2, Young's modulus of E_1 and density of ρ_1.The resonance frequency of this coated cantilever can be described by

$$f_2 = \frac{1}{2\pi}\sqrt{\frac{k_0 + 2k_1}{n(m_0 + 2m_1)}} = \frac{1}{2\pi L^2}\sqrt{\frac{3(E_0 I_0 + 2E_1 I_2)}{nw(\rho_0 h_0 + 2\rho_1 h_2)}} \tag{2.17}$$

with

$$I_2 = \frac{wh_2}{12}(3h_0^2 + 6h_0 h_2 + 4h_2^2) \tag{2.18}$$

Here, the cantilever with spring constant k_0 and the coating layers with spring constant k_1 are assumed as springs connected in parallel. According to the Hook's law, the effective spring constant of the parallel aligned springs is the sum of all spring constants involved.

2.2.2 Static Mode

In the static mode, the deflection is mostly measured by a beam deflection setup (Figure 16). Here, light is focused on the free end of the cantilever. The reflected light is collected by a position sensible detector (PSD). When a displacement of cantilever takes place, the position of the reflected light in the PSD changes and thus the displacement can be recorded.

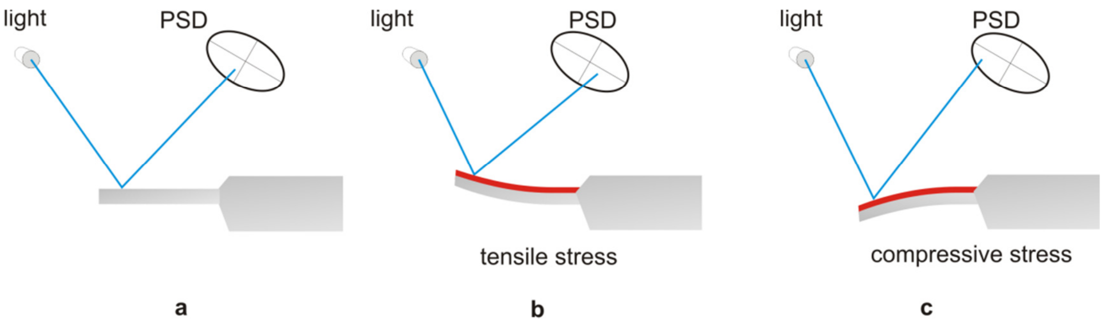

Figure 16: (a) Work principle of a beam deflection setup in static mode. The red lines denoted the coating layer. (b) Tensile stress bends the cantilever towards coating layer and the reflected laser changes to another position. (c) Compressive stress bends the cantilever away from the coating layer.

To operate the cantilever as a sensor to target molecules, the cantilever has to be coated on only one side with an active layer, which has high affinity to the target molecules in the environment. The other side can be left uncoated or can be coated with a passive layer, i.e. a surface that does not exhibit affinity to the target molecules. Upon absorption of the target molecules in the active layer, the surface stress in the active layer changes and induces elastic deformation of cantilever beams.[51]

The direction of the bending of cantilevers depends on the stress exerted by the coating film. Under a **tensile stress** the surface of the coating layer tends to shrink and the cantilever bends towards the coating layer (Figure 16b); under a **compressive stress** the surface of the coating layer tends to expand and the cantilever bends away from the coating layer (Figure 16c). Both tensile and compressive stresses can be induced by elastic property change, conformational change, volume change or surface charge variation in the coating layer.

The deflection Z of the cantilever is related to the thickness of the cantilever h_0, its length L, its *Young's* modulus E_0 and its Poisson's ratio υ_0. If the coating layer with thickness of h_1 is much thinner than the cantilever ($h_1/h_0 \leq 5\%$), the relation between the surface stress change and the deflection of the cantilever can be described by Stoney's equation.[51-52]

$$\sigma = \frac{E_0 h_0^2}{6(1-\upsilon_0)} \cdot \frac{2Z}{Z^2 + L^2} \tag{2.19}$$

For thicker film (h_1/h_0>5%), the thickness of the film has to be considered for the expression of the surface stress:[53]

$$\sigma = \frac{E_0 h_0^3}{6(1-\upsilon_0) h_1^2 (1 + h_0/h_1)} \cdot \frac{2Z}{Z^2 + L^2} \tag{2.20}$$

On the basis of the correlation between the surface stress change and the deflection of cantilever, the surface stress of self-assembled alkanethiols on gold has been measured,[44c] the hybridization of DNAs on the cantilever has been monitored, [46c] and the absorption of mercury to the gold layer, which was deposited on a cantilever, was observed.[44b]

The above mentioned two equations and examples are all based on one presumption that the material is linear elastic, which means that the stress is simply the deformation multiplied by the elastic modulus, and the relationship is valid for every moment e.g. time independent. If the coating materials of cantilever are viscoelastic materials, for instance polymers, the stress change in the films induced by absorption of target molecules is time dependent, even if the concentration of the absorbed target molecules is constant.[54]

In most cantilever applications as chemical sensors, only the response of cantilever in the equilibrium state was considered for target molecule detection. In this work I will focus on the process before the cantilever reached the equilibrium state – the transition process, which may contain information crucial to the sorption process for the target molecule/active layer pair. In return, this information can be used to optimize the functionalized cantilever sensor for fast recognition process or larger response to target molecules.

3 FCS Study of DNA Hybrid Micelles

Amphiphilic molecules form micelles in aqueous solution, if the concentration of the single molecules also called as unimers is higher than the critical micelle concentration (CMC). Under the CMC, the unimers tend to absorb at the air/water interface to minimize the contact of water and the hydrophobic part. Above the CMC, the capacity of the interface to hold the unimers exceeds and the unimers go into the solution and form aggregates or micelles. The micelles mostly take the spherical shape; they can also be bilayers and vesicles (Figure 17).

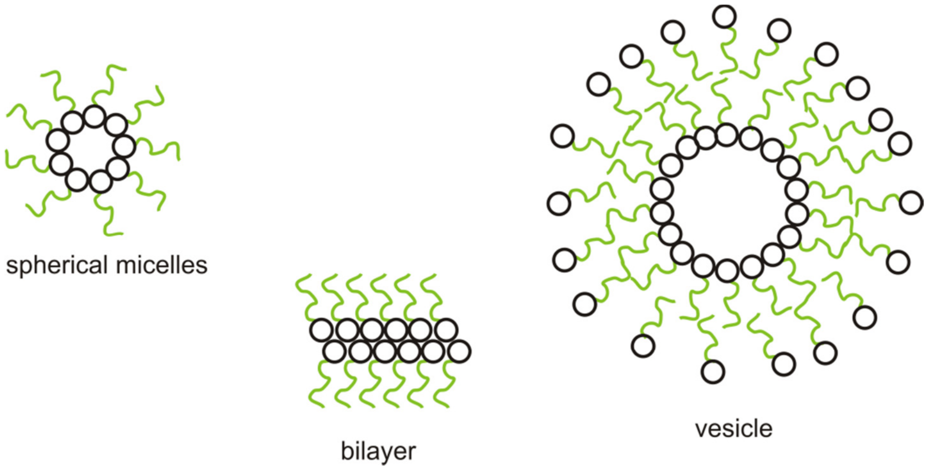

Figure 17: Micelles formed of amphiphilic molecules in different shapes.

The shape of the micelles has a tremendous impact on their applications - the drug loading and release, circulation time of the micelles in bloodstream,[55] targeting and cellular uptake. Several desirable features have been observed for micelles with different structures, such as enhanced drug loading and better cellular uptake.[6c, 56] For instance, rod-like micelles of dsDNA-*b*-PPO show a better uptake by cells than spherical micelles formed by the same molecules.[56] The confocal laser scanning microscopy image of the cells incubated with fluorescently labeled rod-like micelles (Figure 18a) reveals a homogenous micelle distribution in the cells and no adsorption of micelles onto the cell surfaces. In contrast, the cells incubated with spherical micelles are only partly stained (Figure 18b). In micelles with a rod-like shape, the hydrophobic PPO block is less shielded than in the spherical micelles and might thus be better able to interact with the cell membrane. The authors suggested that the difference in shape between rod-like and spherical micelles is a possible reason for the different uptake rates of micelles into cells. These results indicate that design and characterization of the shape of DNA block copolymer micelles is crucial for their applications.

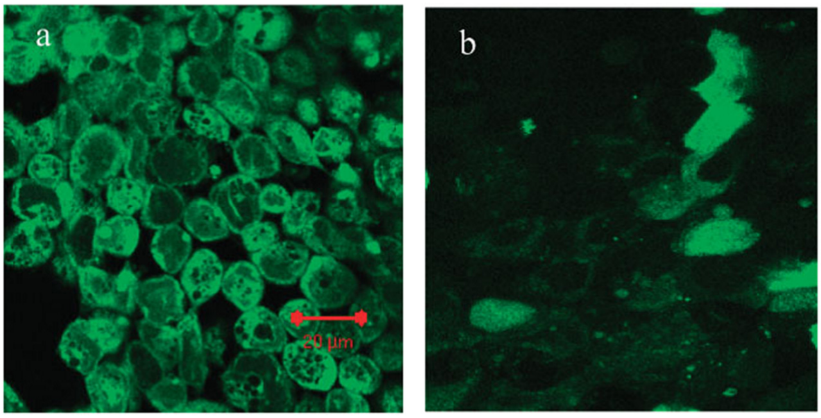

Figure 18: Confocal laser scanning microscopy images of Caco-2 cells incubated with fluorescently labeled (a) rod-like and (b) spherical dsDNA-*b*-PPO micelles.[56]

This section, I discuss shape of aggregates formed from a conjugated of DNA and fluorophore perylenediimide (PDI). The conjugate consists of a PDI chromophore covalently linked to single stranded (ss) DNA at one of the two imide ends of the PDI (Figure 19a).[57] A PDI is a fluorescent dye with high photo stability and high fluorescence quantum yield. [15] Functionalized with sulfonic acid water soluble PDI is also water soluble. Hence PDI-based DNA conjugates have good solubility in water and they can self-assemble into functional supramolecular architectures in the aqueous solution, since PDI is planar and tend to stack via π–π interaction (Figure 19b).[58]

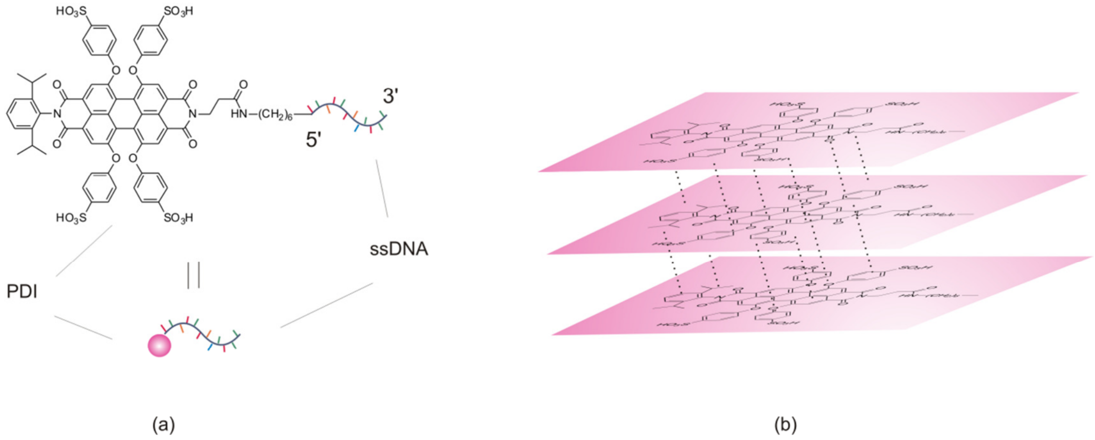

Figure 19: (a) Structure of PDI in the PDI-DNA conjugate and the symbol for PDI used in this work; (b) Illustration of the stacking between planar PDI molecules via π–π interaction.

It is confirmed by fluorescence absorption spectra that PDIs conjugated with DNAs have maintained their chromophoric characteristics and the absorption maximums of PDIs linked to ssDNAs with different sequences are around 550 nm and the emission maximum is at about 640 nm (Figure 20). Also aggregates formation of dsDNA with PDI incorporated in the helix structures such as Dimers and Hexamer were observed by temperature dependent fluorescence spectrum and infrared (IR) spectrum. [58e, 59]

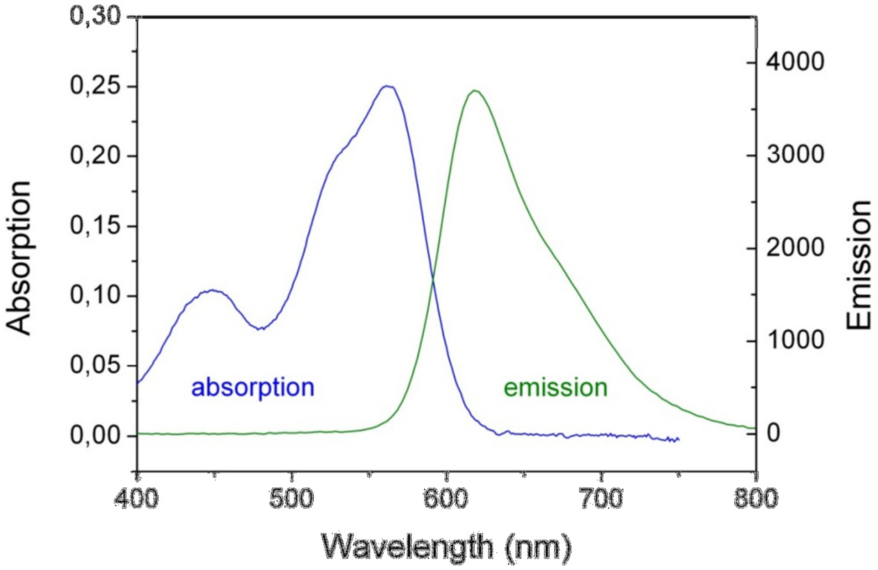

Figure 20: Fluorescence absorption and emission spectrum of PDI.

Details of the micelle formation of PDI labeled DNAs can be explained as follows. For the sake of simplicity, in the text the **conjugates consisting of PDI and ssDNA** is denoted as **ssDNA-PDI**, the **ssDNA** containing complementary sequences to the ssDNA-PDI is denoted as **template ssDNA**, and **dsNDA-PDI**stands for the **conjugates of PDI and dsDNA** obtained upon hybridization of ssDNA-PDI and template ssDNA (Figure 21a). Upon hybridization ssDNA-PDI with different template ssDNA, dsDNA differently labelled with PDI can be generated. When the template ssDNA and the ssDNA-PDI conjugates have the same length (the same amount of bases), upon hybridization a dsDNA conjugated with one PDI (dsDNA-PDI) will be achieved (Figure 21a); when the template ssDNA contains four repeat complementary units to ssDNA-PDI, dsDNA labeled with four PDIs will be formed upon hybridization (Figure 21b) under the assumption of complete hybridization. I named the dsDNA labeled with four PDIs as dsDNA-4PDI.

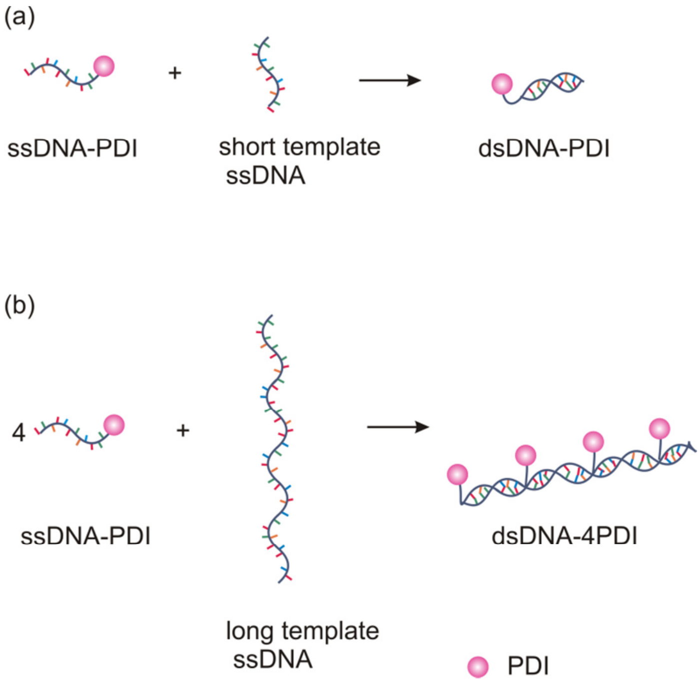

Figure 21: Illustration of hybridization of ssDNA-PDI with (a) complementary ssDNA in the same length and (b) template ssDNA with 4 complementary units.

The dsDNA-4PDI, which has four planar PDI sticking out of the side, resembles the dsDNA-PPO copolymer in structure, which has been investigated already by Ding *et al.* Similarly, ssDNA-b-PPO was first hybridized to a template ssDNA with four complementary units and dsDNA-*b*-PPO with four PPO on the side. Via hydrophobic interaction between the PPOs, micelles with rod-like structure are formed. [7b]

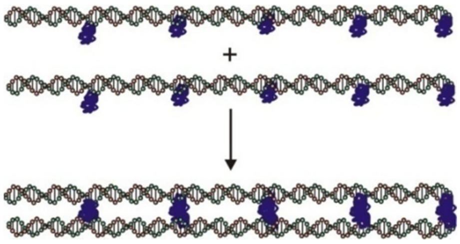

Figure 22: Illustration of dsDNA-*b*-PPO and the formation of a dimer in rod-like structure.[7b]

The rod-like aggregates can be observed by SFM in tapping mode on a mica surface in aqueous environment (Figure 23). Different models to interpret the aggregation formation are also shown in Figure 23.

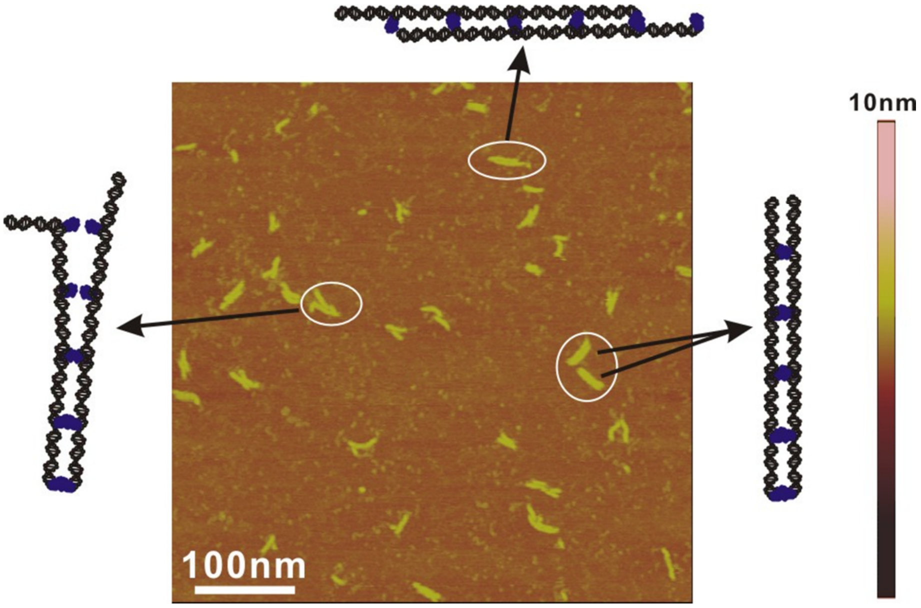

Figure 23: Tapping mode height image (520X520 nm^2) of DNA-*b*-PPO on mica in buffer solution. Three models illustrating partly paired and totally paired rods are shown.[7b]

Due to the similarity in the structure of the dsDNA-4PDI conjugates and the dsDNA-PPO, it is expected that aggregates with rod-like structure can also be formed from the dsDNA-4PDI. Previous investigation on dsDNA-4PDI with 4 PDI moieties stacking out of the side by means of SFM has been performed by Wang*et al.* and it has revealed that there are indeed rod-like structures formed from dsDNA-4PDI on a mica substrate (Figure 24).

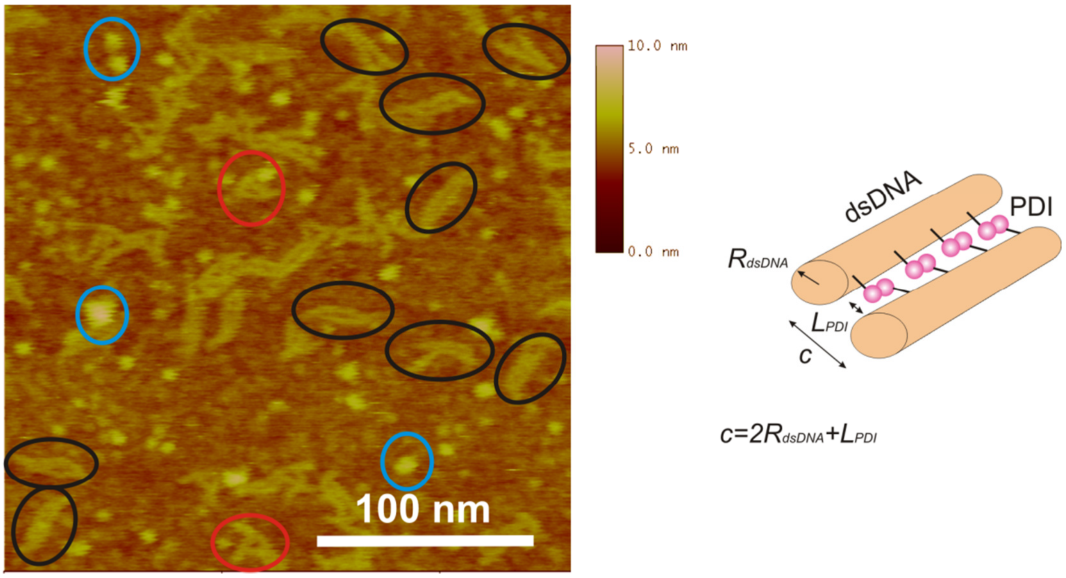

a **b**

Figure 24: SFM images of micelles formed from dsDNA88mer-PDI on a mica surface (a) and a sketch of the aggregate showing the distance between the two parallel aligned dsDNA helixes (b).

Here, the concentration of the dsDNA88mer-4PDI was about 2 µM ($8 \cdot 10^{-5}$ g/mL) with assumption of complete hybridization. Several dimeric structures were observed (black marked areas in Figure 24a), which indicated a parallel alignment of two helices of dsDNA-4PDI. The contour length of the rod structure was 33±5.3 nm. This yields a length per base pair of 0.37 ± 0.06 nm, which is in good agreement with the expected value for dsDNA (0.33 nm).[60] The distance c from the center of one dsDNA to the center of the adjacent dsDNA was 4.1±0.4 nm. This distance c (Figure 24b) is the sum of the diameter of the dsDNA ($2R_{dsDNA}$) and the size of PDI (L_{PDI}).

$$c = 2R_{dsDNA} + L_{PDI} \tag{3.1}$$

The diameter of dsDNA $2R_{dsDNA}$ is known as 2.2 to 2.6 nm [60] and the diameter of PDI L_{PDI} is known as 1.0-1.8 nm. Hence, the distance c has a theoretical value of 3.2 to 4.4 nm.

The SFM image in Figure 24not only shows the aggregates of dsDNA-4PDI in dimeric structure, but also other structures like spherical structures (blue marked areas) and irregular structures (red marked areas) on the mica substrate.

To be able to image the molecules on a mica surface, the DNA structures have to be attached to the surface. Otherwise they may be moved away by the cantilever tip. This is achieved by using buffer solution containing Mg^{2+} and Ni^{2+} cations to bind the negative charged DNA structures to the negative charged mica surface. Hence, the mobility of the dsDNA-4PDI is restricted compared to the dsDNA-4PDI in solution.

For most of the practical applications, dsDNA-4PDI will not be attached on a surface but will be dissolved in an aqueous solution, such as the cell uptake study mentioned in the introduction. A direct confirmation of the aggregates formation would be desirable. Therefore, I investigated the aggregates formation of the dsDNA-4PDI in an aqueous solution by means of FCS.

3.1 Calibration of Observation Volume with Rh6G

In this work, Rh6G was used to calibrate the observation volume generated by He-Ne laser at 488 nm. As an example, the autocorrelation curve obtained by measuring Rh6G was shown inFigure 25. The solution contains only Rh6G dyes and therefore a one-component model was used to analyse the autocorrelation function. According to the fit, the diffusion time of Rh6G τ_{Rh6G} is 21 µs and the structure parameter S was 7. The radius of the observation volume ω was 0.15 µm according to equation (2.6) and the observation volume V is 0.14 fL.

Upon analysing the autocorrelation curve, also the particle number can be obtained. According to the equation (2.4), with the lag time τ approaching 0, the autocorrelation function G(τ) corresponds to (1+1/N). Generally, the greater the amplitude of the autocorrelation, the smaller the particle number N and the concentration of the investigated molecules. For the autocorrelation shown in Figure 25the particle number N is 1±0.1 and the concentration of the Rh6G is 12±4 nM. This value is consistent with the adjusted concentration of about 20 nM for the Rh6G.

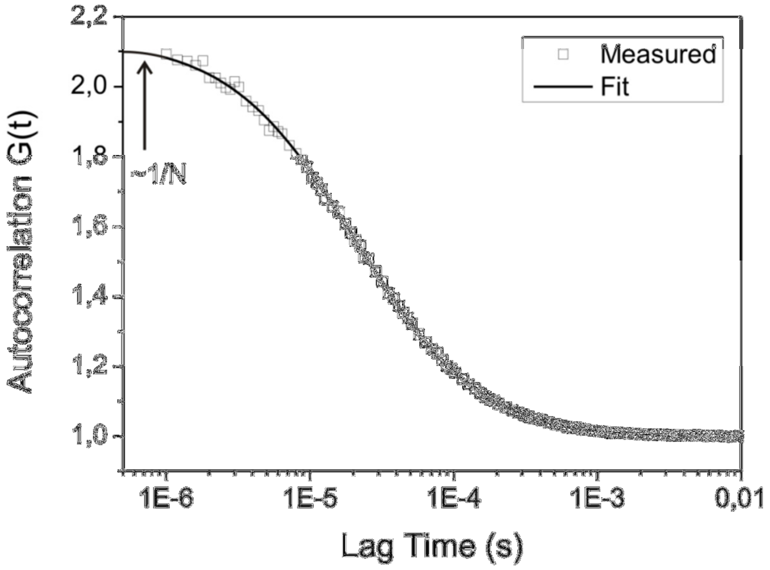

Figure 25: Autocorrelation curve and the fit analysis for Rh6G as reference.

The structure parameter S is particular for the adjusted observation volume and should be used to fit the autocorrelation curve measured in the same observation volume for molecules with diffusion time τ_{sample} and diffusion coefficient D_{sample}. Since the radius of the observation volume ω is also constant for the same adjustment, corresponding to equation (2.6) the diffusion coefficient D_{sample} and D_{Rh6G} correlates to each other as follows:

$$\frac{\tau_{Rh6G}}{D_{Rh6G}} = \frac{\tau_{sample}}{D_{sample}} \qquad (3.2)$$

Knowing D_{Rh6G}, τ_{Rh6G} and τ_{sample}, the diffusion coefficient D_{sample} of the measured molecules can be obtained.

3.2 Diffusion Coefficient of Reference DNAs

In order to better understand mixtures of labeled molecules, it is necessary to know the diffusion behavior of all the components, which can possibly contribute to the autocorrelation curve. In this work it refers to the ssDNA22mer-PDI and dsDNA88mer-PDI. The diffusion coefficients of both molecules are estimated. To avoid the micelle formation via π–π interaction between the PDI moieties, I measure FCS of ssDNA22mer and dsDNA88mer labeled with another dye: Alexa488, which is commercially available. The dsDNA88mer is prepared by hybridization of ssDNA88mer-Alexa488 to complementary ssDNA88mer template.

The autocorrelation curves and the corresponding fits are shown in Figure 26. Since the concentration and thus the particle number N of the ssDNA88mer and dsDNA88mer are different, the amplitude of the autocorrelation curves is also different.

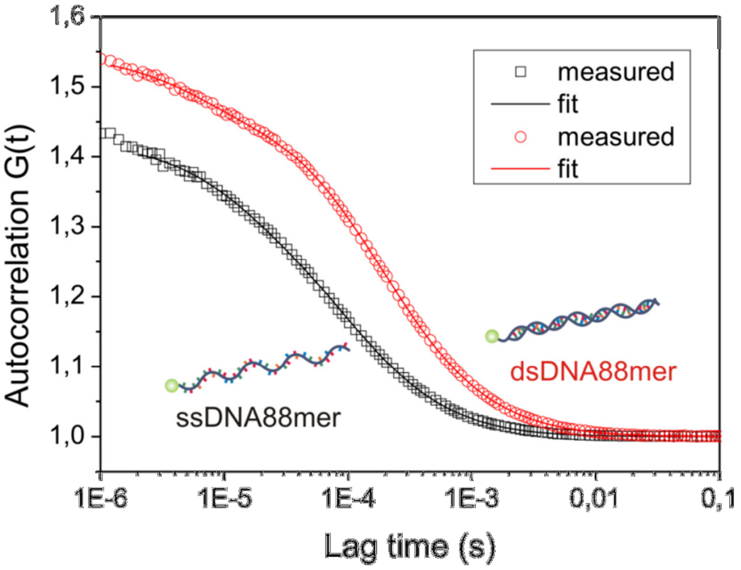

Figure 26: Autocorrelation curves and the corresponding fitting curves of ssDNA88mer and dsDNA88mer.

To have a direct comparison of the both autocorrelation despite of the different concentration of samples, the autocorrelation curves are normalized. This can be done by plotting (G'(t)-1)/(1/N) as function of lag time. The term (G'(t)-1)/(1/N) is obtained by converting the equation (2.4) as follows

$$\frac{G'(\tau)-1}{1/N}=\left(1+\frac{t}{\tau_D}\right)^{-1}\cdot\left(1+\frac{t}{S^2\tau_D}\right)^{-1/2} \tag{3.3}$$

The particle number N can be obtained by fitting the autocorrelation curve. For ssDNA88mer N is 2.8 and for dsDNA88mer N is 2.1. The normalized curves are shown in Figure 27. First impression can be gained by comparing the decay time of the both curves, which allows for a rough estimation of the diffusion time of the molecules. The correlation for ssDNA88mer decays to the half of the maximal amplitude faster than the dsDNA88mer, which indicated that ssDNA88mer have a shorter diffusion time than dsDNA88er.

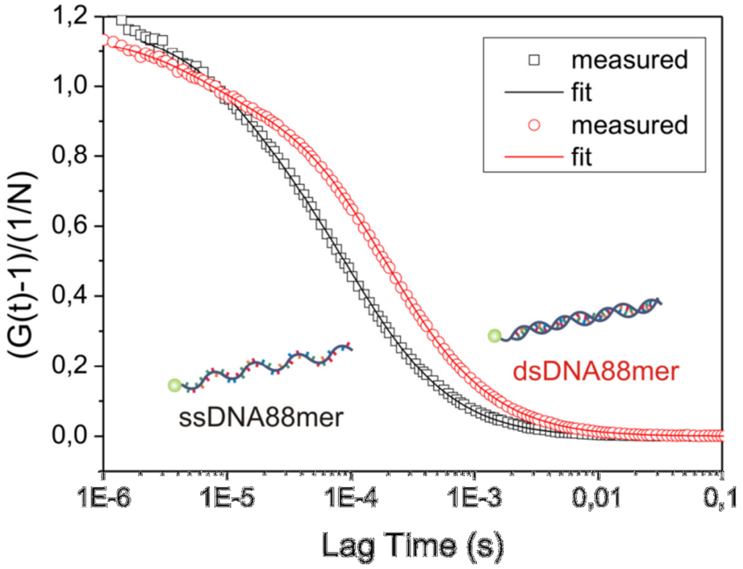

Figure 27: Normalized autocorrelation curves and the corresponding fitting curves of ssDNA88mer and dsDNA88mer.

More details of the diffusion time can be obtained based on the fitting date for the autocorrelation curves. The autocorrelation curve of ssDNA88mer-Alexa488 (black curve) is fitted with a single diffusion time of 94 µs, which corresponds to a diffusion coefficient of 63±5 $\mu m^2/s$. Here, one-component fit is used since the solution only had one component: ssDNA88mer-Alexa488. The hydrodynamic radius R_h corresponding to this diffusion coefficient is 3.4±0.4 nm. The radius of gyration $\bar{R}_g$ for a free joint chain can be calculated with equation (3.4) and it was 2.7 nm for ssDNA88mer with l_0=0.7 nm for one unit of ssDNA, which includes one phosphate and sugar unit with one base.[61]

$$\bar{R}_g^2 = \frac{N \cdot l_0^2}{6} \qquad (3.4)$$

The hydrodynamic radius obtained by analyzing FCS data is consistent with the theoretical radius of gyration for ssDNA88mer.

After hybridization, the autocorrelation curve of dsDNA88mer shifts to the right, indicating a longer diffusion time. The autocorrelation curve of dsDNA88mer-Alexa488 (red curves) is fitted with a single diffusion time of 189 µs, which corresponds to a diffusion coefficient of 41±4 $\mu m^2/s$. For a dsDNA88mer with a length of 30 nm and diameter of 2.4 nm, the theoretical diffusion coefficient calculated with equation (2.9) for molecules with rod-like structure is 38 $\mu m^2/s$. The diffusion coefficients obtained from FCS (41±4 $\mu m^2/s$) and from the theory are in the same range.

Here, also a one-component fit is used since the fit gives a satisfied result. The absolute fit deviation obtained by comparing the autocorrelation curve and the fit curve (Figure 28) shows a smooth curve.

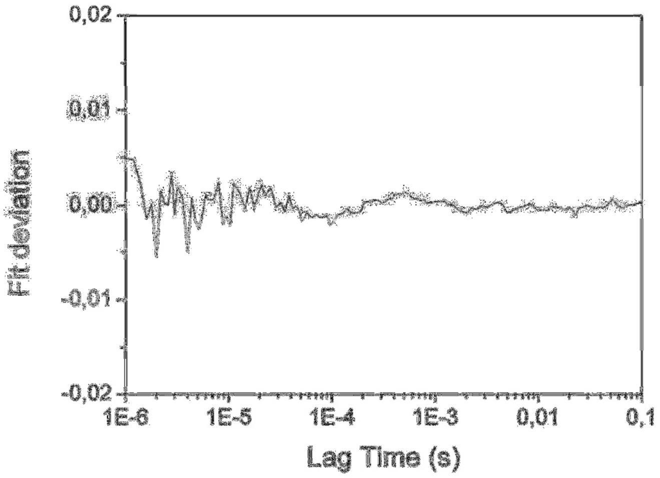

Figure 28: Absolute fit deviation obtained upon comparing the autocorrelation curve and the fit curve for dsDNA88mer labeled Alexa488.

3.3 Diffusion Coefficient of dsDNA88mer-4PDI

According to the investigation of dsDNA-*b*-PPO, aggregates in rod-like structure with two dsDNA helices aligned parallel to each other is observed at concentration of dsDNA-*b*-PPO above its CMC.[7b] The typical CMC of copolymers ranges from 10^{-8} to 10^{-3} M.[18, 62] In principle, the CMC of dsDNA-*b*-PPO should be estimated first though measuring a series of solution containing dsDNA-*b*-PPO at different concentration. The formation of aggregates of dsDNA-*b*-PPO should be reflected by an increased diffusion time of the samples. However, practically it is not feasible since the concentration of the dye molecule have to stay under about 100 nM to perform FCS properly.

First, I choose to measure an aqueous solution of dsDNA88mer-PDI at a concentration of 15 nM, since this concentration is an ideal concentration for FCS. For the hybridization, 60 nM ssDNA-PDI and 15 nM template ssDNA is used to yield 15 nM dsDNA-4PDI. Also this concentration is in the range of the typical CMC of copolymers, and aggregates formation of dsDNA-PDI molecules can be expected.

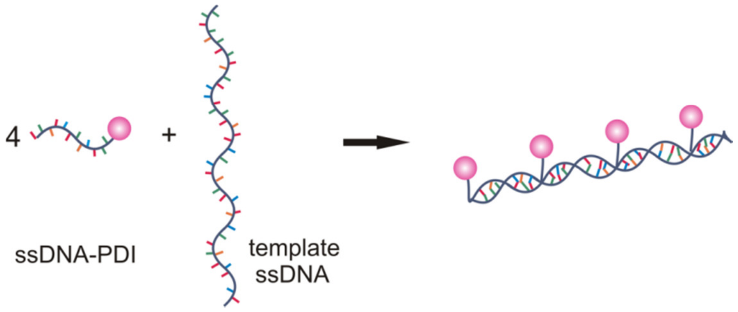

Figure 29: Illustration of sample for dsDNA88mer with PDI

The ssDNA22mer-PDI is hybridized with template ssDNA88mer and yields dsDNA88mer-PDI (Figure 29). The autocorrelation curve is fitted with one single diffusion time of 178±10 µs, yielding a diffusion coefficient of 42±3 µm^2/s. The diffusion coefficient is in agreement with the one obtained for dsDNA88mer-Alexa488 (41±4µm^2/s), which indicates that there is no aggregate of dsDNA88mer-PDI formed. Compared to the dsDNA88mer used for the reference measurement with only one Alexa488 attached to each ss88mer, dsDNA88mer-4PDI has four PDI units, which means three more dye molecules per molecule. However the diffusion coefficients of the both molecules are the same, this can be understood by taking account of the small contribution of the PDIs to the diffusion of dsDNA88mer due to the relative low molecular weight of PDI (1311 g/mol) compared to the dsDNA88mer (54250 g/mol).

Here, the observation volume *V* obtained from reference measurement with Rh6G is 0.17 fL. The particle number *N* for dsDNA88mer-PDI is 2±0.2 and thus the concentration is 19±5 nM according to equation (2.6), which is in agreement with the adjusted concentration of 15 nM.

Since no aggregate of dsDNA-PDI is observed, the concentration of dsDNA88mer-PDI at 15 nM is probably under the CMC. For the next step, the concentration of dsDNA-PDI has to be increased.

3.4 Design of Concentrated Solution of dsDNA88mer-4PDI

While the concentration of dsDNA-PDI is increased, the concentration of dye molecule has to be kept low for a good signal-noise ratio. This can be achieved by adding a second dye to dsDNA-PDI, which can be detected separately than PDI, as the fluorescence signal source. Hence, the PDI would not be detected and the concentration of PDI can be as high as desired for the form of aggregates. Alexa488 is chosen as the second dye, the maximal emission of Alexa488 is at 519 nm, which can be well separated with the emission of PDI with maximum at about 620 nm.

The system is designed as follows: ssDNA22mer-PDI is mixed with not labeled ssDNA88mer and ssDNA88mer-Alexa488 (Figure 30a), the ratio between ssDNA88mer and ssDNA88mer-Alexa488 is kept at 9:1 to keep the concentration of Alexa488 low. The concentration of the hybridization product dsDNA88mer-4PDI can be adjusted by the concentration of ssDNA22mer-PDI and the concentration of the both template ssDNA88mers. Hence it is possible to obtain dsDNA88mer-4PDI in higher concentration (possibly higher than CMC), while the concentration of dsDNA88merlabeled with Alexa488 is kept low for the FCS measurement (Figure 30b).

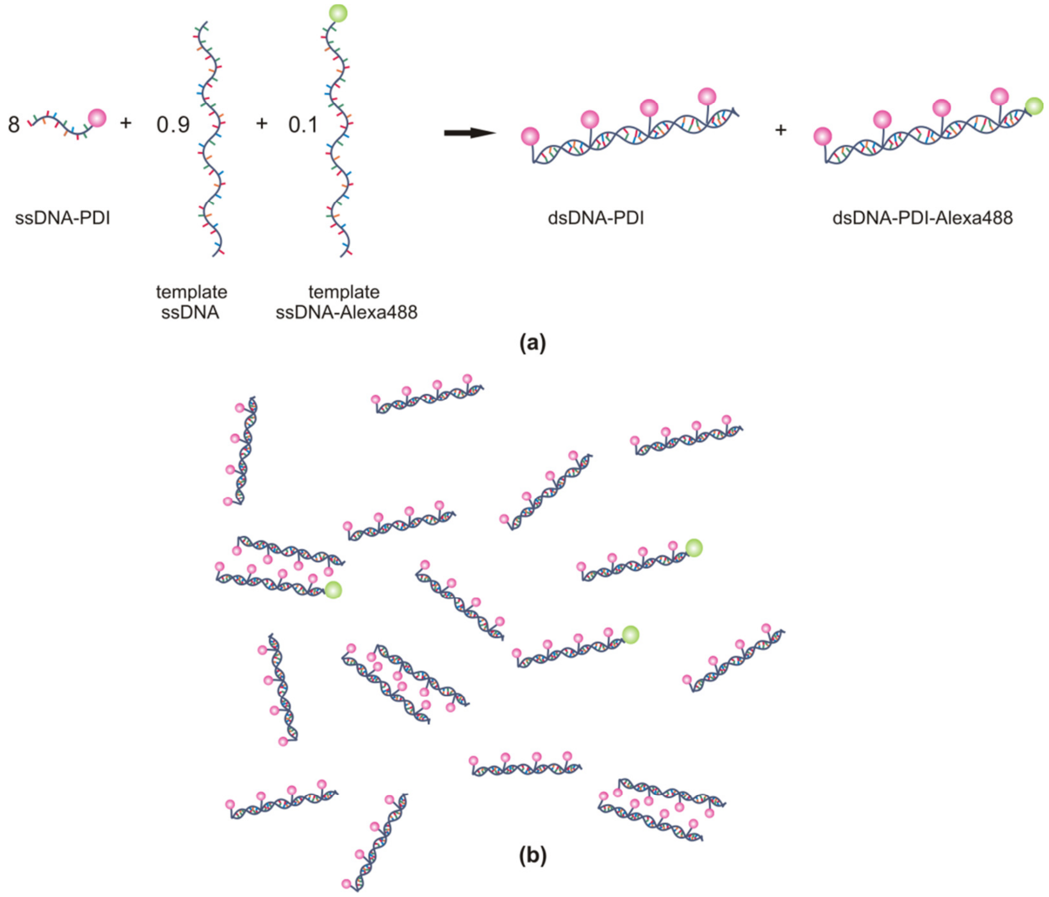

Figure 30: Illustration of the strategy to obtain dsDNA-4PDI in higher concentration and to keep the dye molecules in low concentration: (a) ssDNA22mer is hybridized with a mixture of ssDNA88er-PDI and ssDNA88mer-Alexa488; (b) setting the ratio between ssDNA88mer-PDI to ssDNA88mer-Alexa488 at 9:1 yields a solution with only 10% dsDNA88mer labeled with Alexa488.

3.5 Diffusion Coefficient of Concentrated Reference Sample

With the above introduced strategy, the concentration of dsDNA88mer-4PDI can be increased up to micromolar range. Increasing the concentration of dsDNA88-PDI also increases the viscosity of the aqueous solution. In order to assess the effect of the increased viscosity on the diffusion of target molecules, a reference sample was prepared. Here, instead of ssDNA22mer-PDI, unlabeled ssDNA22mer was hybridized with the mixture of template ssDNA88mer and ssDNA88mer-Alexa488 (Figure 31). Precisely, the total concentration of dsDNA88mer was increased to 1.5 µM. Only 90 nM of these dsDNA88mer were labeled with Alexa488.

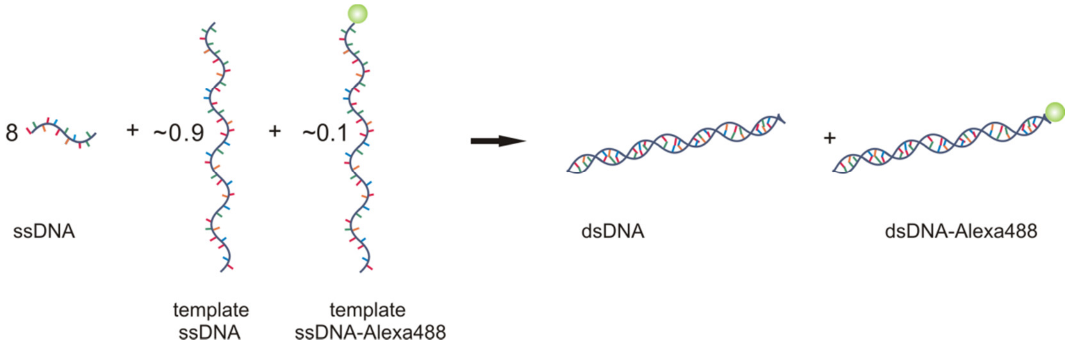

Figure 31: Illustration for the mixture of dsDNA88mer and dsDNA88mer-Alexa488 as reference sample.

The normalized autocorrelation curves for dsDNA88mer at both 15 nM and 1.5 µM are shown in Figure 32. The correlation for dsDNA88mer at 1.5 µM decays to the half of the maximal amplitude slower than the dsDNA88mer-Alexa488 at 15 nM, which indicates that dsDNA88merat 1.5 µM have a longer diffusion time than at 15 nM.

The autocorrelation curve is fitted with a single diffusion time of 287 µs, since there is only one fluorescent component in the solution. As compared to dsDNA88mer-Alexa488 at15 nM with diffusion coefficient of 41±4 µm^2/s, the diffusion coefficient decreases to 23±4 µm^2/s at 1.5 µM. The formation of aggregates can be excluded, since there are no PDIs connected with the dsDNA88mer. The decrease of the diffusion coefficient of dsDNA88mer with concentration could be the result of decreased mobility of the dsDNA88mer induced by the crowded surroundings.

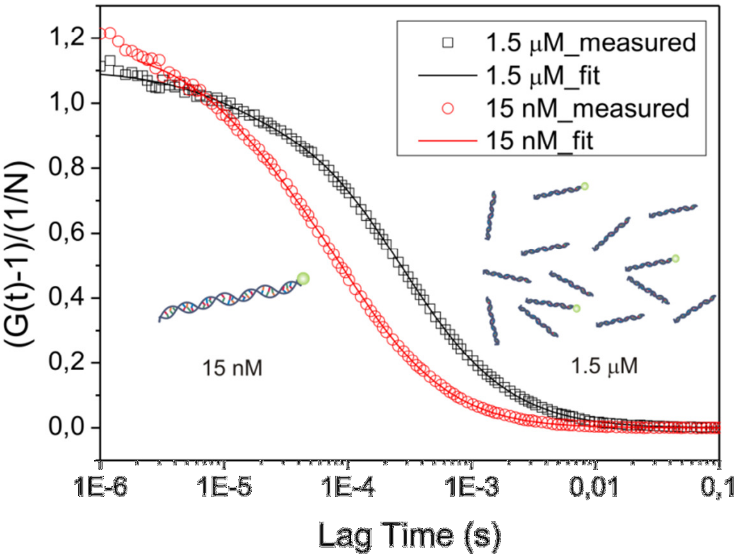

Figure 32: Normalized autocorrelation curves and the corresponding fit curves for dsDNA88merat 15 nM (red) and 1.5 µM (black).

A similar phenomenon has been observed by a FCS study of polystyrene (PS) tracers diffusing through a PS matrix at different concentration.[63] Here, unlabeled PSs with different molecular weight are solved in acetophenone as matrix. The fluorescently labeled PS as tracer is added into the matrix and the diffusion of the labeled PS in matrix is monitored by means of FCS. As shown in Figure 33there is a critical concentration of the PS matrix at about 10^{-2} g/mL, above which the diffusion coefficient of the tracer PS decreases with increasing concentration of the matrix PS. The concentration of dsDNA88mer-PDI with M_w at 59494 g/mol used in this work varied from 15 nM to 1.5 µM, which corresponded to 9×10^{-7} g/mL and 9×10^{-5} g/mL, which is much lower than the critical concentration mentioned above.

Here, the radius of gyration of PS is about a few hundred nanometers, i.e. much longer than the dsDNA used in my work. Hence these two systems cannot not be compared directly in terms of the critical concentration, at which the diffusion coefficient of the studied molecules decreases.

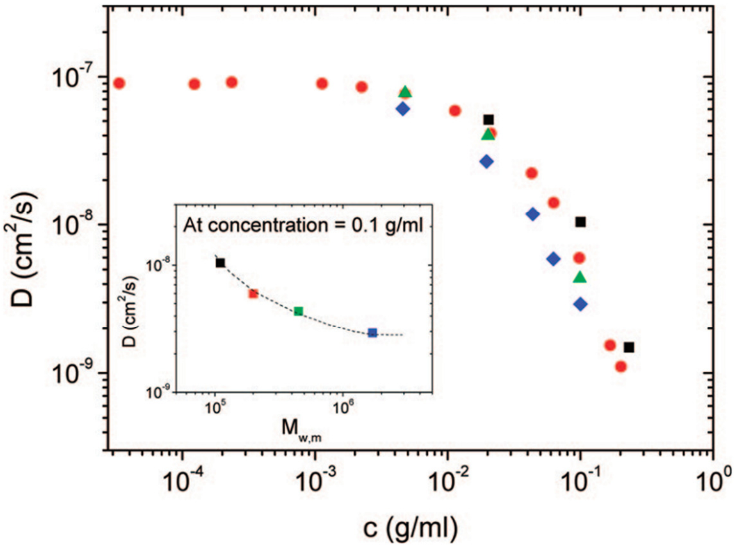

Figure 33: Diffusion coefficient of PS tracer as a function of the concentration of the matrix PS with different molecular weight in acetophenone. Black data: M_w=110K; red data: M_w=220 K; green data: M_w=450 K; blue data: M_w=1700 K.

Here, the concentration obtained from the fit for dsDNA88mers labeled with Alexa488 was 80±5 nM, which is consistent with the adjusted concentration for the labeled dsDNA88mers (90 nM).

3.6 Diffusion Coefficient of Concentrated dsDNA88mer-4PDI

The autocorrelation curves produced by dsDNA88mer-Alexa488 and dsDNA88mer-4PDI at concentration of 1.5 µM are shown in Figure 34. The autocorrelation curve shifts lightly to the right, indicating a longer diffusion time of dsDNA88mer-4PDI. The autocorrelation of dsDNA88mer-Alexa488 has been already discussed before.

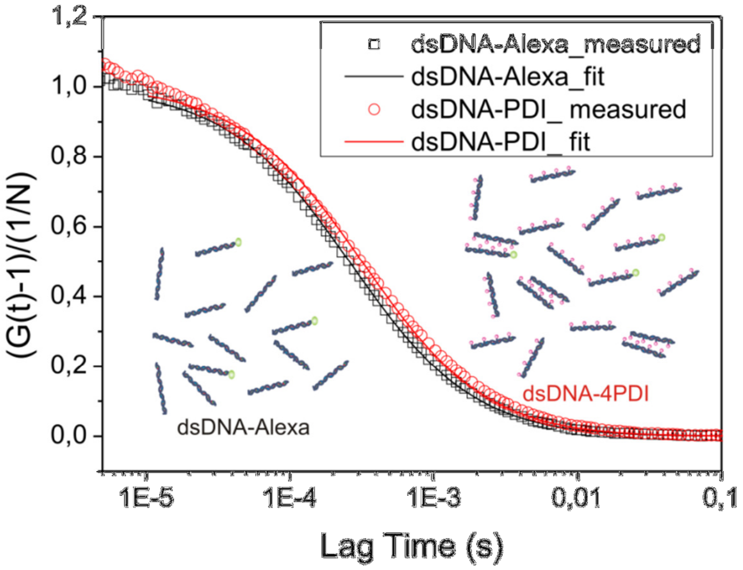

Figure 34: Normalized autocorrelation functions and the corresponding fit curves of dsDNA88mer-Alexa488 (black) anddsDNA88mer-4PDI (red) at concentration of 1.5 µM.

The fit of autocorrelation curve obtained for concentrated dsDNA88mer-4PDI (Figure 34, red solid curve) with one-component model is not satisfactory due to the wavy form of the deviation curve (Figure 35).This fact indicates that there is probably more than one component in the solution.

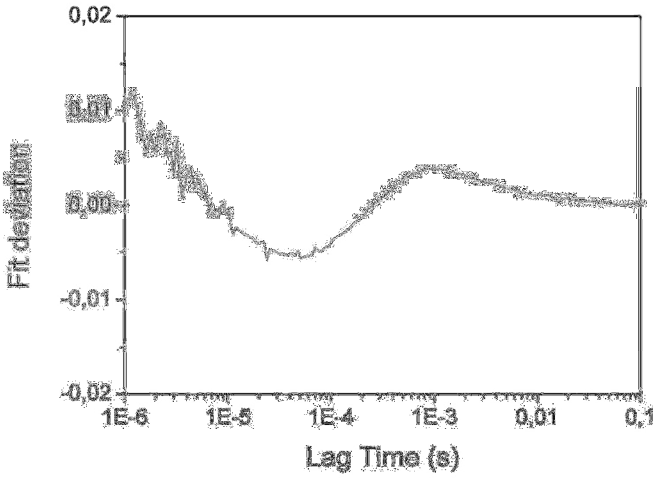

Figure 35: Absolute fit deviation obtained upon comparing the auto-correlation curve and the fit curve using one-component fit.

The next step for the data treatments is to fit the autocorrelation curve with a two-component model. It is reasonable to assume that one of the components is the dsDNA88mers-4PDI. For the fit, one of the diffusion coefficients should be set at 23 $\mu m^2/s$ for the dsDNA88mers-4PDI according to the reference measurement. Hence, the second diffusion coefficient obtained is 2 $\mu m^2/s$, which corresponds to a hydrodynamic radius of 80 nm. However, such a large component is hardly to be constructed in a system containing single molecules with length of about 30 nm (Figure 36). Therefore, I considered the fit with a two-component model is not appropriate.

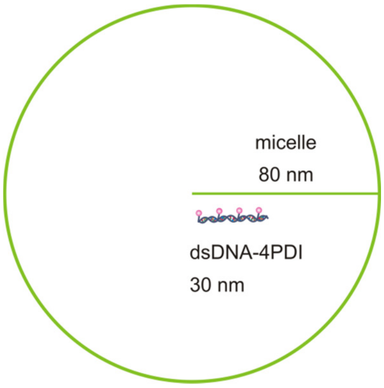

Figure 36: Illustration of a spherical micelle with hydrodynamic radius of 80 nm and a dsDNA88mer-4PDI molecule.

As a summary, the autocorrelation curve cannot be analyzed appropriately either with a one-component fit or with a two-component fit. This can be explained by taking following facts into account: (i) the diffusion coefficient of dsDNA88mer-4PDI (38 $\mu m^2/s$) and the dimeric aggregates (27 $\mu m^2/s$) are close to each other. Therefore it is difficult to distinguish the two components upon fitting the autocorrelation curve;[64] (ii) as observed already in the concentrated solution of the dsDNA88mer-Alexa488 in section 3.4, the diffusion coefficient of dsDNA88mer decreases with increasing concentration. This can induce extra difficulty to distinguish the two components in addition to the effect (i); (iii) in the solution the chance of the dsDNA88mer-4PDIs to meet each other is lower than the case when dsDNA88mer-4PDIs are attached on a surface as in the SFM experiments. Therefore, despite of the similar concentration used for FCS and SFM experiment (FCS: 1.5 μM; SFM: 2 μM), it is possible that there are barely aggregates formed in the solution for the FCS study.

3.7 Summary

In this chapter, the aggregation of the DNA hybrid material dsDNA88mer-4PDI in aqueous solution has been investigated by means of FCS. Earlier SFM studies on the same material demonstrated the formation of dsDNA88mer-4PDI dimers at concentrations around 1.5 to 2 μM due to π-π stacking of their PDI moieties. Using FCS, only single dsDNA88mer-4PDI molecules were found at the relatively low concentration of 15 nM. To be able to perform FCS measurements at higher concentrations, a small fraction of the hybrid molecules was labeled with a second dye, Alexa488 and the measurements were carried out by tracking Alexa488 instead of PDI. Also, dsDNA88mer molecules which are not functionalized with PDI moieties and hence do not aggregate via π-π stacking were measured as a single molecule reference for the diffusion coefficient. It was found that the diffusion coefficient of single molecules decreased drastically (from 41 $\mu m^2/s$ to only 23 $\mu m^2/s$) upon increasing their concentration a hundredfold (from 15 nM to 1.5 μM). This decrease of diffusion coefficient can be explained by the largely increased likelihood of temporary entanglements between single molecules at higher concentration. The correlation curve obtained for dsDNA88mer-4PDI at 1.5 μM shifted lightly to the right side of the curve obtained for single dsDNA88mer single molecules, which could be considered as a hint of a slightly larger component present in the solution. However, when the curve was fitted with a two-component model with one diffusion coefficient set at $23 \mu m^2/s$ for single molecules, the second component was too large to be possibly formed in such a system. Hence, the existence of aggregates in rod-like shape cannot be directly approved by FCS.

An interesting effect observed here is that the diffusion coefficient of dsDNAs decreased with its concentration. In the future, it will be interesting to measure a series of solutions with different concentration of dsDNAs and to generate a diagram with the diffusion coefficient as a function of its concentration, similar as the diagram shown in Figure 33. In particular, a critical concentration for the dsDNAs can be obtained, above which the diffusion coefficient changes upon concentration variation. It will be interesting to see whether the critical concentration of dsDNAs depends on its length and sequences of the base pairs. This kind of diagram can be helpful regarding applications of DNA molecules in general.

4 FCCS Study of Size and Residence Time of DNA-*b*-PPOs

Recently, a novel bioorganic molecule ssDNA-*b*-PPO has been developed, which is constituted of a hydrophobic PPO block and a hydrophilic DNA block.[5] The CMC of this molecule has been determined to be about 400 nM. In aqueous solutions above the CMC, spherical micelles with a PPO core and a DNA shell are formed. After hybridization of the ssDNA-*b*-PPO to a template ssDNA of the same length, the micelles retain their spherical form (Figure 3a).[7b, 7c, 65] These micelles have promising potential for drug delivery. The drugs can be loaded within the hydrophobic core, while the DNA shells can be used to transfer the micelles to the target cells or tissues.

The advantage of this ssDNA-*b*-PPO is that the PPO has a relatively low glass transition temperature (T_g=-70°C). Most block copolymers with a hydrophobic part exhibiting high glass transition temperature (higher than room temperature) dissolve poorly in aqueous solution and need the addition of organic solvent to form micelles. After the extra solvent is removed, the hydrophobic part becomes glassy and the micelles is "frozen", which means the single molecules are trapped in the micelles and cannot move out. Moreover, the single molecules swimming around in the solution cannot enter these "frozen" micelles. Using PPO as the hydrophobic part, the formation of "frozen" micelles can be avoided and the micelles can be characterized in their thermodynamic equilibrium state.

To characterize the micelles formed from dsDNA22mer-*b*-PPO, SFM and FCS have been used.[7b] The SFM images proved the spherical form of the micelles and FCS measurements in solution showed that their diameter was about 11 nm.

It is known from the SFM measurement that dsDNA-*b*-PPO have a rod-like structure.[7b] The length L of a single molecule can be predicted by the following empirical equation

$$L = N_{bp} l_{bp} + 2R_{PPO} \tag{4.1}$$

Where N_{bp} is the number of base pairs, l_{bp} is the length per base pair, and R_{PPO} is the gyration radius of PPO. For dsDNA, l_{bp} takes the value 0.33 nm;[60] for PPO with a molecular weight of 6800 g/mol, R_{ppo} was 2.0 nm.[66] Hence the total length of dsDNA22mer-*b*-PPO was 11 nm.

Here I address a question, why do the micelles have a diameter in the same range as the length of single molecules? For the micelles illustrated in Figure 37, a larger diameter is expected. Now let us consider the solution which contains the micelles formed from dsDNA22mer-*b*-PPO, there are at least two components: the single dsDNA22mer-*b*-PPOs and their micelles. When the concentration of single dsDNA22mer-*b*-PPOs is much higher than that of the micelles, it is possible that only single dsDNA22mer-*b*-PPO is detected by FCS. It is also possible that FCS cannot distinguish between different components in a solution if their diffusion coefficients are too similar (see also chapter 3).

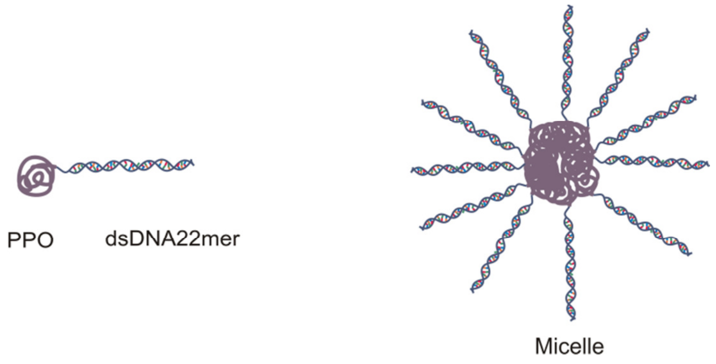

Figure 37: Illustration of a single dsDNA22mer-*b*-PPO and a micelle formed from dsDNA22mer-*b*-PPO with spherical shape.

Can one only detect the micelles without interference of the single molecules? The answer is yes and the method to be used is the FCCS. Here, ssDNA-*b*-PPO is first hybridized separately with a short template ssDNA either labeled with Alexa488 or Alexa633 (Figure 38 a, b) to become fluorescently labeled. After mixing the both labeled dsDNA-*b*-PPO at 37°C, dsDNA-*b*-PPOs can exchange between the micelles and their environment. Thus micelles labeled with both Alexa488 and Alexa633 can be formed (Figure 38 d). By means of FCCS, only the micelles containing both dyes can be observed since the signal of the red dye and the green dye from one micelle cross correlate with each other. In contrast, the single dsDNA-*b*-PPOs labeled only with Alexa488 or Alexa633 cannot be detected, because their movements are independent and the two signals do not cross-correlate with each other. To keep the concentration of the dyes low, not labeled dsDNA-*b*-PPO is also added to the system to supply enough single molecules to form micelles (Figure 38c).

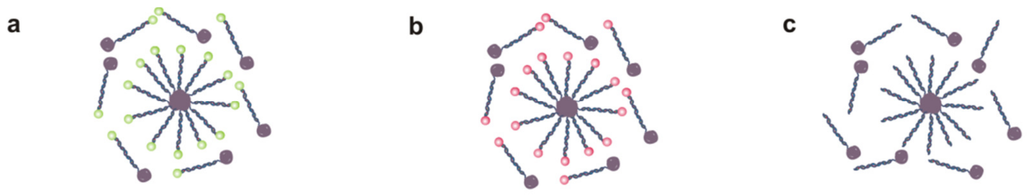

dsDNA-*b*-PPO labeled with Alexa488

dsDNA-*b*-PPO labeled with Alexa633

not lablled dsDNA-*b*-PPO

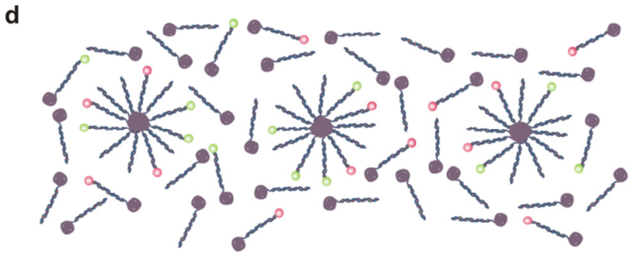

mixture of **a**, **b** and **c** for FCCS

Figure 38: Illustration of the micelle formation of dsDNA-*b*-PPO via hybridization of ssDNA-*b*-PPO with template ssDNA. (a) ssDNA-*b*-PPO was hybridized with template ssDNA labeled with Alexa488; (b) ssDNA-*b*-PPO was hybridized with template ssDNA labeled with Alexa633; (c) ssDNA-*b*-PPO was hybridized with template not labeled ssDNA; (d) both labeled and not labeled ssDNA templates were used to adjust the concentration of the dsDNA-*b*-PPO appropriate for FCCS.

Since the dsDNA-*b*-PPO micelles are not “frozen”, this above designed strategy should work. In addition, this strategy also offers the opportunity to estimate the residence time of dsDNA-*b*-PPO in the micelles. As mentioned, an excess amount of not labeled dsDNA-*b*-PPO will be added (Figure 38c). When the exchange of dsDNA-*b*-PPO between the micelles and the solution takes place, after enough time the probability that the micelles contain only the not labeled dsDNA-*b*-PPO is high. Then the micelles will not be detectable for FCCS anymore. Measuring the time the fluorescent labeled micelles needs to transform to unlabeled micelles can give direct information of the residence time of unimers in micelles.

4.1 Estimation of Micelle Size

The correlation curves obtained for the mixture of labeled and not labeled micelles are shown in Figure 39. The autocorrelation curve (blue curve) obtained for Alexa488 can be fitted with a diffusion time of 166±8 µs, which corresponds to a diffusion coefficient of 40±5 $\mu m^2/s$. The autocorrelation curve (black curve) obtained for Alexa633 can be fitted with a diffusion time of 252±10 µs, which is longer than the diffusion time obtained for Alexa488. This is a result of the observation volume increase, which is 17 fL generated at wavelength of 488 nm and 26 fL generated at wavelength of 633 nm. The corresponding diffusion coefficient is also 40±5 $\mu m^2/s$. The satisfactory fits with one-component model indicate that only single molecules can be observed by autocorrelation.

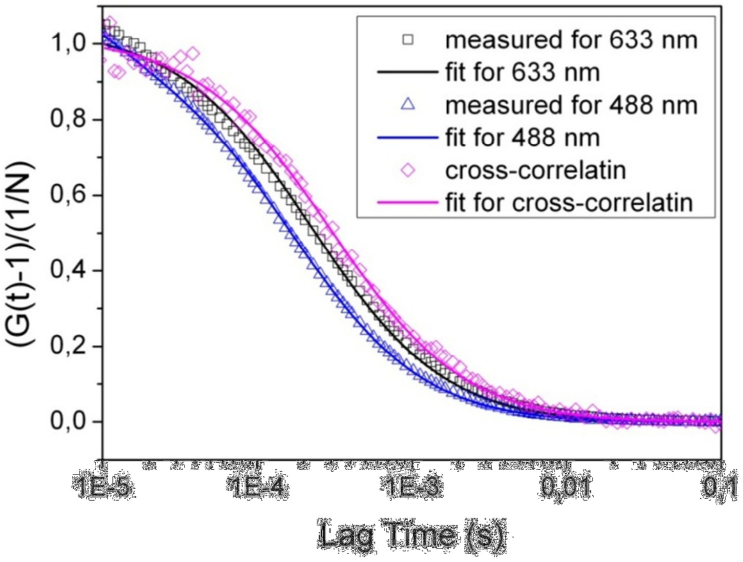

Figure 39: Normalized autocorrelation curves (black and blue) and cross-correlation curve (magenta) of 100 nM dsDNA-*b*-PDI labeled with Alexa488 and Alexa633.

As already mentioned, the length of dsDNA22mer-*b*-PDI is about 11 nm. The diameter of the dsDNA segment is 2.2~2.6 nm,[60] and the diameter of PPO segment is 4.0 nm. According to equation (2.9), the diffusion coefficient (40±5 $\mu m^2/s$) obtained by autocorrelation corresponds to a molecule with length of 12 nm and with diameter of 4 nm. These values are consistent with the literature reported values.

The cross-correlation curve (Figure 39 magenta curve) can be fitted with a diffusion time of 305±8 µs, which corresponds to a diffusion coefficient of 22±3 $\mu m^2/s$ and a hydrodynamic radius of 11.2±0.7 nm according to equation (2.8). As mentioned earlier, via cross-correlation only micelles obtained both Alexa488 and Alexa633 can be observed. The micelles have a radius corresponding to the length of the dsDNA-*b*-PPO.

The particle number of the micelles N_{br} can be obtained by equation (2.11) and the concentration of the labeled molecules and micelles can be obtained by equation (2.6). The original solution containing labelled dsDNA-*b*-PPO is 10 µM and after adding excessive amount not labelled dsDNA-*b*-PPO in to the solution, the total concentration of dsDNA-*b*-PPO increases to about 28 µM. For the FCCS measurement, the solution is diluted 100 fold with water and thus the final concentration of the labelled dsDNA-*b*-PPO is prepared 280 nM. The concentration obtained by autocorrelation curve for Alexa488 and Alexa633 labeled dsDNA-*b*-PPO is 260±35 nM and 274±25 nM, which are consistent with the set values. The concentration of micelle is about 38±5 nM.

The FCCS data makes more sense to estimate the size of the micelles. The micelles can be described as illustrated in Figure 37. The fact that the radius of the micelles corresponds to the length of the single molecule is confirmed by FCCS result. Also the concentration of the micelles is much lower than that of the single molecules according to FCCS, which can probably explain why FCS fails to detect the micelles: the single molecules makes a dominate contribution to the autocorrelation due to the large amount so that the contribution of the micelles is concealed.

4.2 Estimation of Residence Time of dsDNA-*b*-PPO

The concentration (10 μM) of the two starting solutions containing differently labeled dsDNA22mer-*b*-PDI is higher than the CMC (~400 nM) of the molecules and the micelles should have already formed before the both solutions are mixed. Therefore the existence of doubly labeled micelles in the mixed solution strongly supports the fact that the dsDNA22mer-*b*-PDI molecules exchange between the solution and the micelles. The residence time of a dsDNA22mer-*b*-PDI, which has also been called as the “life time” of a unimer in a micelle, is an important parameter, which gives information about the kinetic of the micelle formation.

The FCCS measurements have been carried out for about two days. The cross-correlation has been observed thoroughly (Figure 40). After 48 hours, there are still micelles containing both dyes in the solution.

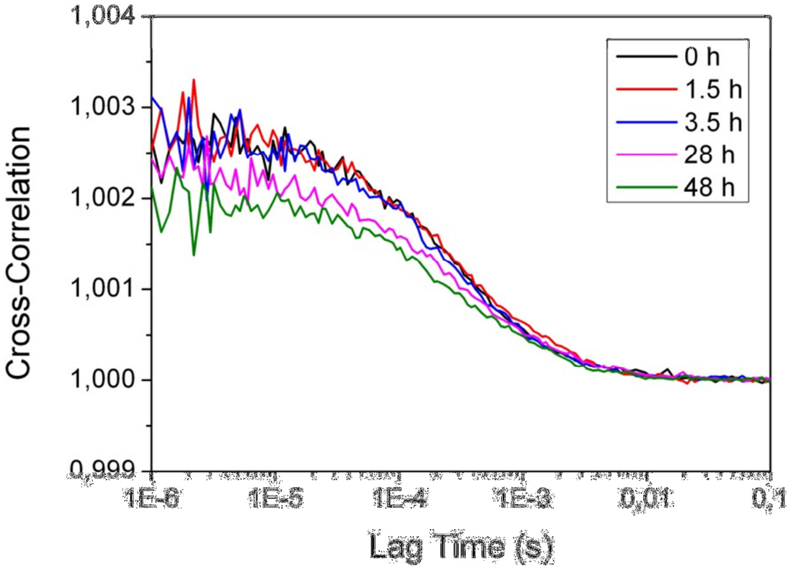

Figure 40: The chronological evolution of the cross-correlation curves of the micelles.

The hydrodynamic radius of the micelles keeps constant at about 11 nm for at least 48 hours (Figure 41a). The concentration however, increases with time (Figure 41b). The concentration of single dsDNA-*b*-PPOsalsoincreases according to the autocorrelation. The increase in concentration for both dsDNA-*b*-PPOs and micelles can be only understood by taking water evaporation into account.

As a matter of fact, the micelle containing both Alexa488 and Alexa633 does not disappear for FCCS measurement lasts for 48 hours. This indicates that the residence time of the unimers in the micelles can be counted in days. Due to the uncontrollable water evaporation, a precise residence time of the dsDNA-*b*-PPOs cannot be estimated.

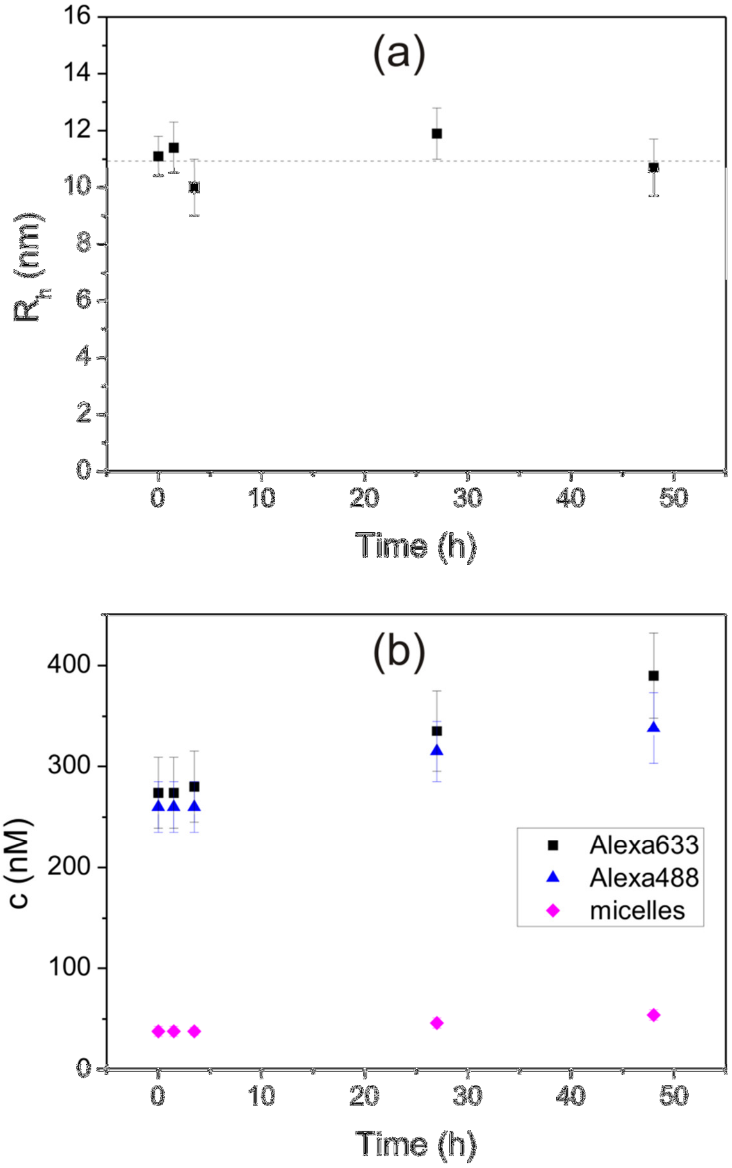

Figure 41: (a) The chronological evolution of hydrodynamic radius obtained for micelles; (b) the concentration variation of dsDNA-*b*-PPO labeled with Alexa488, Alexa633 and the doubly labeled micelles as function of time.

4.3 Summary

FCCS has been used to study the micelle size formed from dsDNA22mer-*b*-PPO and the residence time of the dsDNA22mer-*b*-PPO in the micelles. Previous FCS results for the same micelles estimated their radius to be about 5.5 nm.[7b] In contrast, the hydrodynamic radius of the spherical micelles obtained by FCCS is about 11.2±0.7 nm. I consider the hydrodynamic radius of 11.2 nm is reasonable since (i) it corresponds to the length of the single DNA-*b*-PPOs; (ii) FCCS detects the doubly labeled micelles directly without any disturbance from singly labeled single DNA-*b*-PPOs.

For the estimation of the residence time ofdsDNA22mer-*b*-PPO molecules in their micelles, an excess of non-labeled single molecules was added to the doubly labeled micelles and the resulting solution was monitored by FCCS. Even after two days, however, doubly labeled micelles were still present in the solution despite potential exchange with non-labeled molecules. The measurements imply that the residence time of dsDNA22mer-*b*-PPO molecules in their micelles is in the order of several days. However, due to the evaporation of water from the sample holder, the experiment had to be terminated.

I am generally convinced that the strategy of using FCCS and differently labeled amphiphilic molecules is an adequate and elegant method to determine the residence time of such amphiphilic molecules in their micelles. This strategy should first be tested with a model system, for instance fluorescently labeled PS-PEO block copolymers.[67] The synthesis of this polymer is well established and the amount of the samples is not limited. Hence the concentration of non-labeled amphiphilic molecules can be increased to accelerate the exchange process. Also a better sealed sample holder should be purchased or built, which ensures that the water would not leave the chamber.

5 Coating Cantilever with Colloidal Monolayer

To operate the cantilever as sensor, it has to be functionalized with an active layer or active layers, which can either absorb, adsorb or interact with target molecules. The absorption/adsorption of target molecules has to be transduced to a physical change of the cantilever, which can be detected. The change can be the deflection or resonance frequency change of the cantilever. The process where the cantilever bends as response to external stimuli is defined as static mode. The process where the resonance frequency of the cantilever changes upon the external stimuli is called dynamic mode. In static mode, the absorption/adsorption of target molecule induced the differential surface stress ($\Delta s = s_1 - s_2$, where s_1 and s_2 are the induced stresses on the top and bottom surface of the cantilever) of the cantilever and the cantilever bends. In dynamic mode, the absorption/adsorption of target molecule either induce a change of the mass of the active layer or a change of the elastic property of the cantilever, which can be reflected by the resonance frequency shift.

Recently, cantilevers coated with polymer film as active layer have drawn scientists' attention. These functionalized cantilevers are not only suitable as chemical recognition element to detect organic vapors[68] and other chemicals,[19a] they can also be used to analyze the properties of the polymer films. For instance, the glass transition temperature (T_g) of the polymer thin film is determined by operating the cantilever in static mode.[69] The deflection of the cantilever coated with polymer is recorded during heating. The change of elastic properties of polystyrene (PS) during glass transition induced different bending of the cantilever and thus marks the T_g. Operating cantilevers in dynamic mode enables the investigation of the mechanical properties of poly(vinyl acetate),[70] since the resonance frequency and the quality (Q) factor of cantilever are related to elastic properties the coating layer. Also cantilever coated with plasma polymerized allylamine (PAA) thin film is used to study the swelling of the polymer in different humidity by means of measuring the deflection of the cantilever. The volume expansion of the polymer coating is transduced into deflection of the cantilever owing to interfacial stress between the functional coating and the cantilever.[71] Thundat et al. measure the crosslinking of a mercaptan-ester-based polymer film upon UV irradiation. In particular, the coupling of the polymer elasticity to the spring constant of the cantilever has been observed by measuring the resonance frequency of the cantilever during the coating polymer is hardened via UV radiation.[72] The increase in resonance frequency of the cantilever reflects the increase of the spring constant, which is induced by the hardening of the polymer coating layer.

Compared to conventional methods like differential scanning calorimetry and rheology, there are several potential advantages by using cantilever to study the thermomechanical properties of polymers: only small amounts of the order of nanograms (ng) of polymer is needed; measurements can be carried out in-situ, for instance during a temperature ramp or a change in humidity. Several samples can be analyzed in parallel; for example the chips used in this study contained eight cantilevers. Hence eight different samples can be measured at the same time.

To analyze a polymer film by means of cantilever or to apply the cantilever functionalized with polymer as sensor, a proper technique for coating the polymer on the cantilever is necessary. So far, techniques used to functionalize cantilever with polymer films can be divided into two groups: **symmetrical** coating and **asymmetrical** coating. Symmetrical coating means the cantilever is coated identically on both faces and asymmetrical coating means the cantilever is coated only on one face. Symmetrical coating is relative easy and can be realized straightforward upon micro capillary coating,[46b] chemical vapor deposition [73] and dip coating. In contrast, the asymmetrical coating is more sophisticated. To asymmetrically functionalize the cantilever with homogenous films thinner than 10 nm, methods such as shadow masking,[74] immobilizing thiol terminated molecules on gold coated cantilever,[44c, 75] in situ growth of polymer brushes[76] have been used. Thicker films with thickness in the range of 1 µm can be achieved by micro capillary coating[46b] and inkjet deposition[22b], however the films are not homogenous due to coffee stain effects during the drying process.[77]

The resonance frequency change of the cantilever as a function of the polymer coating film thickness has been calculated by Sascha Pihan (Figure 42). If only the added mass plays a role on the resonance frequency shift of cantilever, a decrease of the resonance frequency f_1 with increasing layer thickness is obtained (according to equation (2.17), Figure 42, red circles). In case both the added mass and the elastic modulus of coating polymer film (e.g. a PS layer) change the resonance frequency of the cantilever, a decrease in resonance frequency $f_2$is obtained as well (equation (2.17), Figure 42, black squares). Subtracting both contributions solely indicates the contribution of *Young's* modulus (Figure 42, solid line). In particular the difference of the calculated frequency shifts based on (9) and (10) for a 400 nm thick PS layer (E=3.5 GPa) is in the order of 100 Hz for typical cantilever geometries and is measurable with a standard setup. In other words, assuming that a resonance frequency shift (f_1-f_0) of 100 Hz is measured with accuracy of 10 Hz, a polymer film with thickness of hundreds of nanometers is required.

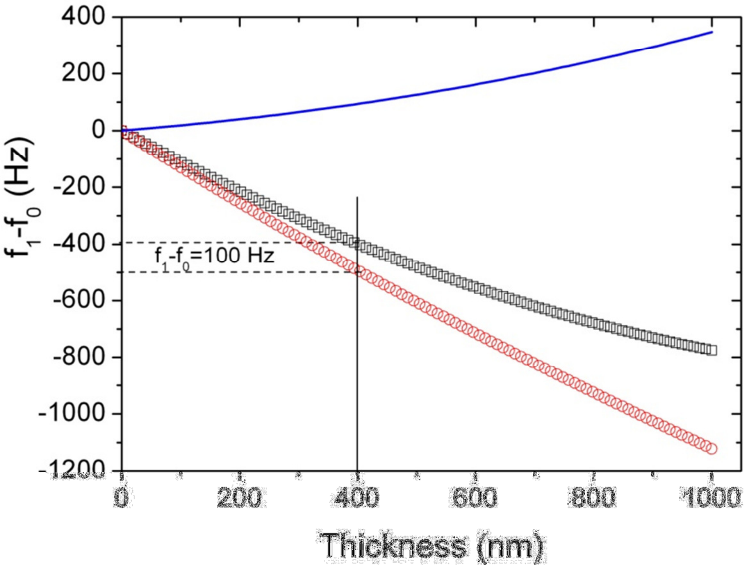

Figure 42: Resonance frequency shift of a cantilever (500 μm long, 90 μm wide and 2 μm thick, resonance frequency f_0 = 11023 Hz) as a function of the coating film thickness. Effect of mass only (red circles), elastic modulus and mass (black squares) and elastic modulus only (blue solid line) are plotted. Figure reprinted by permission from Sascha Pihan.

Due to the ability of polymeric colloids to form close-packed monolayers at the air/water interface, we tried to transfer the closely-packed colloidal monolayer on the cantilevers. Hence, the whole cantilever can be homogenously coated with thick polymer layers. In addition, homogenous polymer films can be generated from the monolayer of colloids upon thermal annealing [27, 78] and organic vapor annealing.[79] With close-packed colloidal monolayer as precursor, it is possible to predict the height of the formed homogenous film. By varying the diameter of PS particles, it is feasible to generate active layers of 300-1000 nm in thickness where the colloidal nature of the monolayer guaranties homogeneity of the film. Candidates as coating materials are for instance polystyrene (PS) particles, polymethylmethacrylate (PMMA) particles and silica colloids.[80] Importantly, I am addressing procedures of coating the cantilever both symmetrically and asymmetrically.

5.1 Coating Cantilever with Colloidal Monolayer

First, a close-packed PS colloidal monolayer is formed at the air/water interface via self-assembly. An organic solvent free method called “dry, sparsely distributed particles” developed by Retsch et al was used.[81]. Aqueous dispersion of PS colloids in concentration of about 0.5-1 wt% was spin coated on a glass parent substrate, which is first functionalized with N-trimethoxysilylpropyl-N,N,N-trimethylammonium chloride to allow the PS spheres to be sparsely distributed on the surfaces (Figure 43a-c). The parent substrate is moved carefully by hand with a pair of tweezers under a shallow angle into a pool of water containing 5×10^{-4} M sodium dodecyl sulfate with pH at 10.5 (pH adjusted by ammonia). While moving the glass slide into the aqueous electrolyte the particles float off. They attract each other, presumably by capillary forces, and form a close-packed monolayer of typically 5×5 mm^2 (Figure 43d, e).

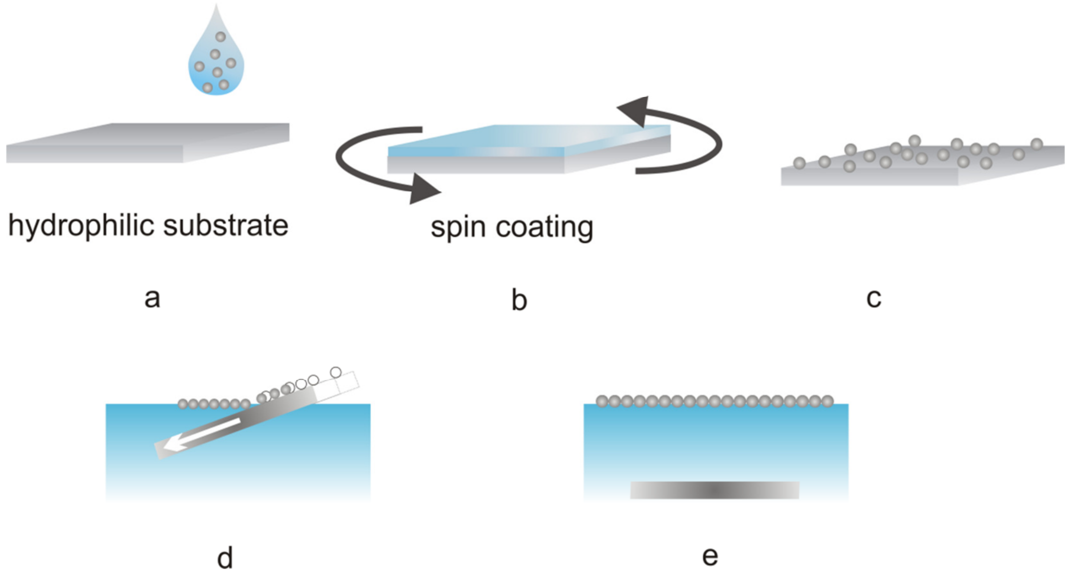

Figure 43: The self-assembly of PS particles at the air/water interface.

In order to transfer monolayer, a cantilever (cleaned in Ar plasma) is immersed in the water by holding the chip with a pair of tweezers by hand. The cantilever is then slowly withdrawn at an angle of about 30° in about 3 seconds through the colloidal monolayer (Figure 44a, b). Then, the cantilevers are dried on a tissue. Under these conditions, the cantilever is coated with colloidal monolayers on both sides, which can be observed both by naked eyes and by an optical microscope due to the color scattered by the colloidal monolayer.

We suggest the reason for the both sides coating could be the free hanging layer between the cantilevers on one chip (Figure 44c, pointed out with arrows). The monolayer is transferred on one side of the cantilever, which has direct contact with the floating monolayer; meanwhile the free hanging layer could fold back to the underside during drying process (Figure 44d, e). The distance between the cantilevers on one array is 160 µm, which is about twice the width of the cantilever (90 µm).

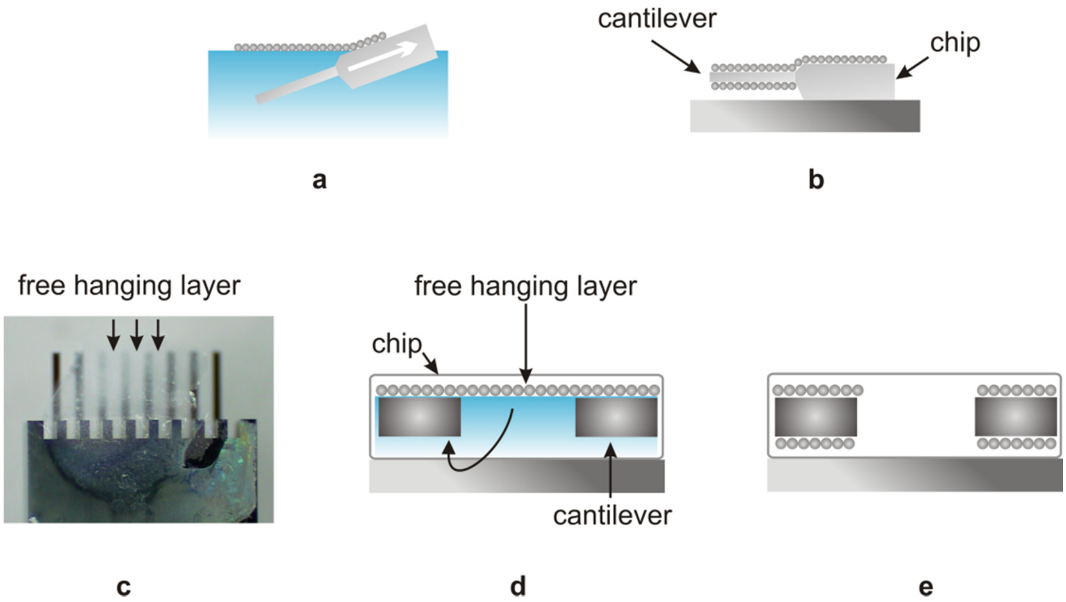

Figure 44: (a, b) Illustration of the symmetrical transfer of the colloidal monolayer onto the cantilever array. (c, d, e) the explanation for the double side coating. (c): microscope image of a cantilever array with large colloidal monolayer attached, the arrows indicates the suggested free hanging layer between the cantilevers. (d) and (e): Illustration of the hanging layer between the cantilevers folding back the back sides of the cantilevers.

The main factor is that both surfaces of the cantilever are hydrophilic and have the same affinity to the PS spheres. Therefore, in order to transfer the colloidal monolayer only on one side of the cantilever, we first functionalized the cantilever with 1H,1H,2H,2H-perfluorodecyltrichlorosilane by chemical vapor deposition to become hydrophobic (contact angle 113°).[82] The hydrophobic cantilever array was placed horizontally on top of the floating monolayer (Figure 45a). Cantilever array and monolayer were transferred onto a hydrophilic substrate e. g. metal (Figure 45b) and the whole assembly was dried in air about one hour (Figure 45c, d).

As confirmed by the microscope image of the leftover monolayer on the hydrophilic substrate (Figure 45g) that there is no monolayer left in the shadow of the cantilever (black frame) and the monolayers in the space between the cantilevers are almost all deposited on the substrate (white frame). The hydrophobic adhesion between the monolayer and cantilever is strong enough to keep them together and the capillary forces drive the particles onto the cantilever in the drying process.

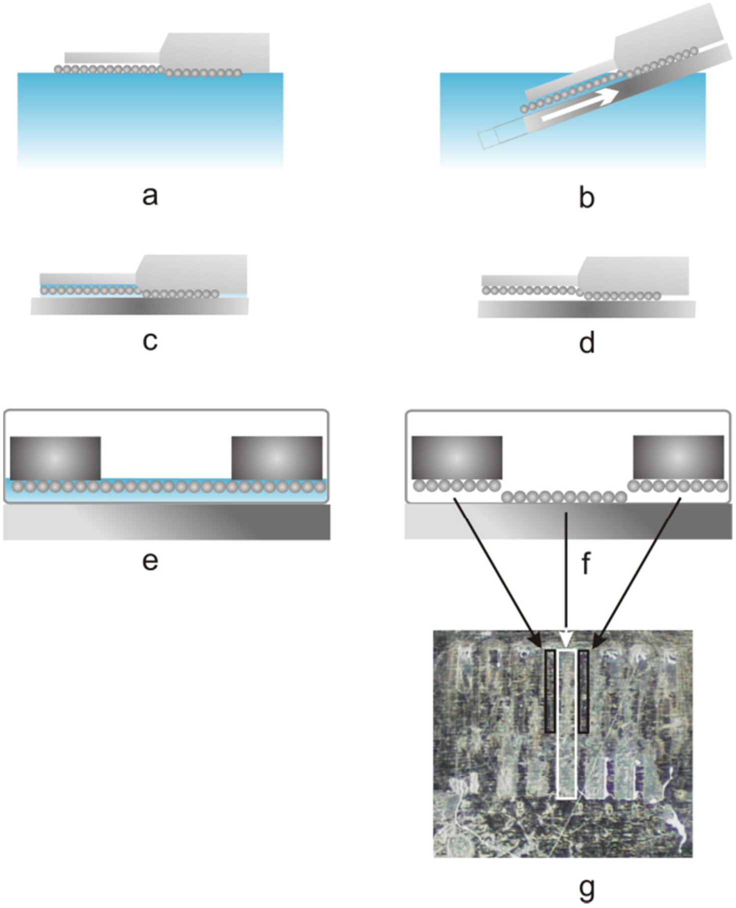

Figure 45: Transfer of colloidal monolayer onto only one side of a cantilever array (a-f). Image (g) was a microscopic image of the substrate after drying, the black marked area is the shadow of the cantilever, and white marked area is the area between the cantilevers.

SEM images of cantilever coated with PS colloidal monolayers on one side (Figure 46a, upper side was coated with monolayer, lower side was free) and both sides (Figure 46b) carried out from the side confirmed the successful coating. The SEM image from above shows an area (36 µm× 26 µm) of the close-packed colloidal monolayer (Figure 46c). Concerning the defect of this area, there are about 40 particles missing and there are two long cracks about 50 µm caused by different orientations of colloidal clusters observed. A SEM image (Figure 46f) of a larger area (100 µm× 90 µm) and a microscope image (Figure 46e) of the whole cantilever (500 µm× 90 µm) show the homogeneity of the coating layer. The density of the PS colloids per area was about 2.24/µm^2. The density of the colloids can also be calculated by means of geometry of the colloids and the cantilever (introduced in next section) and has the value of 2.35/µm^2, which confirms the monolayer coated on the cantilever was indeed close-packed.

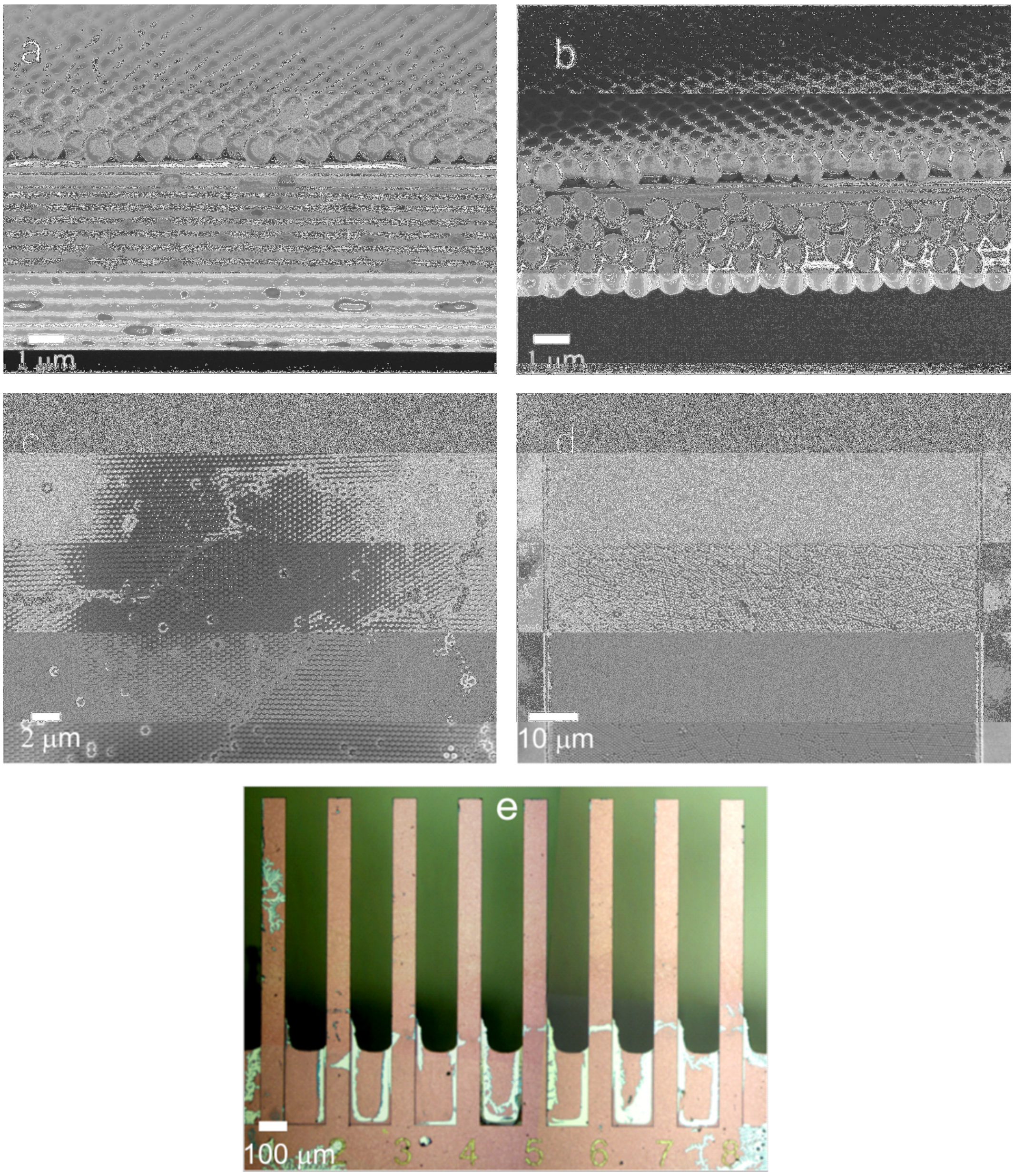

Figure 46: SEM images of colloidal monolayers on one (a) and two sides (b) of two representative cantilevers from the side and from above (c); (d) cantilever tip coated with PS colloids. (e) Microscope image of the whole cantilever array coated with PS colloidal monolayer.

5.2 Adjust Particle Distance by Plasma Etching

After coating the cantilever the close-packed colloids can be adjusted to a non-close-packed order by means of plasma etching. Via plasma etching it is possible to reduce the size of the particles, and thus the distance between the particles can be increased.[83] During the etching process the particles maintain their own position so that the hexagonal order of the colloids remains. Cantilever array coated with PS colloidal monolayer was placed in plasma oven and etched for 2 minutes and 6 minutes. The power of the plasma oven was adjusted at 50 watt and the oxygen supply was set at 5 sccm.

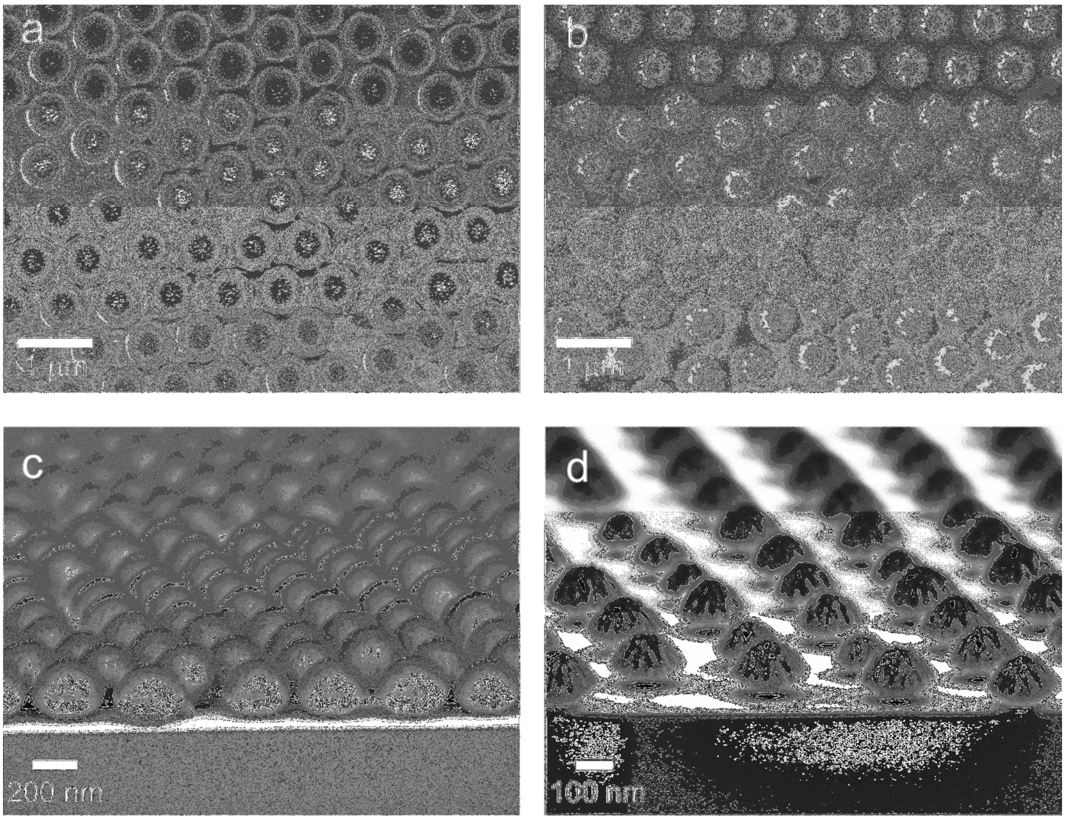

Figure 47: SEM images of plasma etched colloidal monolayers after 2 minutes (a, c) and after 6 minutes (b, d) from above and from the side.

The SEM images (Figure 47a, b) of the monolayer after etching show that the hexagonal structure of the monolayer is maintained. The PS particles have an original diameter of 761±27 nm, which reduces to 616±23 nm after 2 minutes and to

488±25 nm after 6 minutes etching, respectively. In Summary, by varying the etching duration, the particles can be reduced to a desired size.

The SEM images also show that the surface of the particles became creasy after etching. The side view (Figure 47c, d) shows that the surface of the particles from the upper side and the down side are different. This can be understood by taking the anisotropic plasma etching into account. The plasma etching is anisotropic because of the presence of the substrate, which blocks the contact of the oxygen plasma with the down side of the colloids.

5.3 Coating Cantilevers at the End

If the active layers/molecules are coated at the end of the cantilever, their elastic contribution to the spring constant of the cantilever can be neglected. Hence the resonance frequency change of the functionalized cantilever only reflects the mass change of the active layers/molecules.

To coat the PS colloids only at the end of a cantilever, a micro-capillary mounted in a micromechanical manipulator can be used. The capillary is dipped into the aqueous dispersion of PS colloids. Driven by the capillary force the dispersion flows into the capillary. The filled capillary is then mounted in the micromechanical manipulator, which can be moved in three dimensions. The capillary is moved to cover about 50 μm from the end of the cantilever (Figure 48), which has been cleaned before in an Argon plasma oven. After the PS colloids are attached on the cantilever the capillary is driven away and the cantilever is dried in air. With this method all eight cantilevers on one chip can be coated with different colloids. To obtain an average value, at least two of the cantilevers were coated with the same colloids. The colloids are attached on both sides of the cantilever.

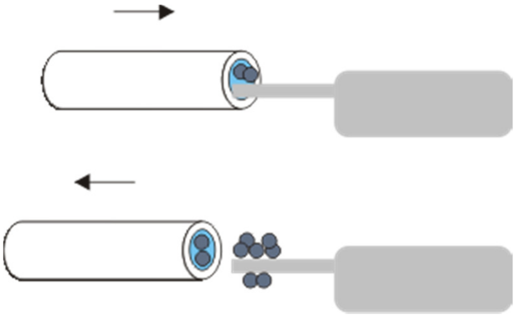

Figure 48: Illustration of coating cantilever only at the end by means of a micro-capillary.

The SEM images confirm that only the end (within a distance of about 50 µm) of the cantilever is coated with colloids (Figure 49a), and the colloids are randomly ordered in one layer or two layers (Figure 49b).

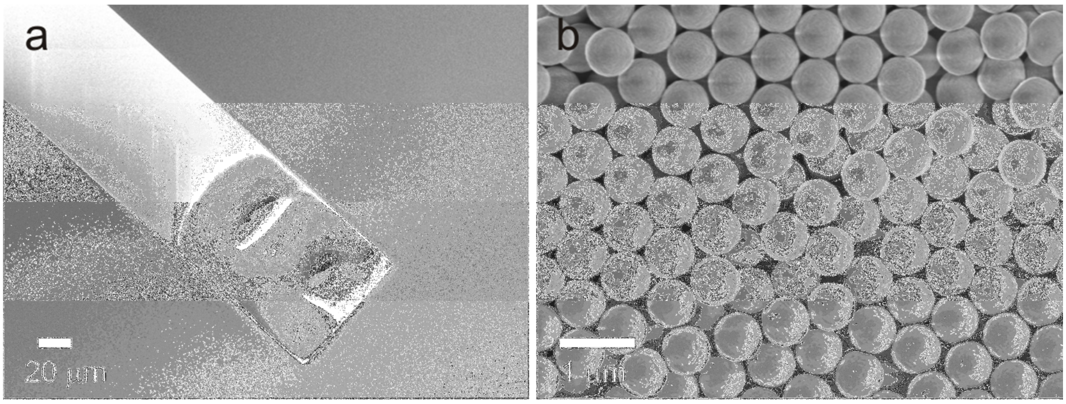

Figure 49: (a) SEM image of cantilever coated at the end with colloids; (b) a close-up view of the coating colloids.

6 Film Formation of Colloidal Monolayers on a Micromechanical Cantilever

After coating the cantilever with colloidal monolayer, I attempt to form homogenous polymer film from the monolayer. For the film formation process from polymer colloids, the glass transition temperature T_g of the polymers plays an important role. Taking film formation via thermal annealing for example, the film formed at temperature above T_g is transparent and mechanical stable, while the film formed below T_g is powdery and fragile.[27, 84] The glass transition denotes the process when polymer materials are heated, they can transfer from their glassy brittle state to a viscoelastic rubbery state. When the polymeric materials are heated close to its T_g, the polymer chains gain enough thermal energy to wiggle first at a small region and to create some free-volume in the material. By further increasing the temperature, the polymer chains become more flexible till the moment they can slide pass each other. For the film formation, when the colloids are heated over their T_g, the polymer chains in a single colloid can easily move out of this particular colloid and start to enter in another adjacent colloid or to entangle with the polymer chains in another adjacent colloid. This step is crucial to generate a mechanically sable film.

As for the investigation of the thermomechanical properties of colloid monolayers by means of the cantilever, following questions are addressed: What kind of information can we obtain on the mechanical properties of particle monolayers? Is it possible to form thick homogeneous polymer layers from colloidal monolayers upon thermal annealing and organic vapor annealing? Can the film formation be detected and the film formation process be monitored? Is it possible to estimate the *Young's* modulus and T_g of the coating layer?

6.1 Dynamic Mode

6.1.1 Mass Loading of PS Colloidal Monolayer

In order to prove the mass loading of the cantilever we measured the resonance frequency shift of micromechanical cantilevers before colloid transfer and afterwards. Using the colloids as coating layer we can estimate the number N of colloids on the cantilever. Assuming a hexagonal close-packing, the area per particle with radius r is $(2r)^2\sin 60°$. Thus the maximal number of colloid particles on one side of the cantilever is

$$N = \frac{wl}{4r^2 sin60°} \tag{6.1}$$

The mass loading of a colloidal monolayer can therefore be described as

$$m = m_P \cdot N = \frac{m_P wl}{4r^2 sin60°} \tag{6.2}$$

with the mass of an individual particle of $m_P{=}4\pi r^3\rho_{PS}/3$ with ρ_{PS} as density of PS, the mass of the particle monolayer is

$$m = \frac{\pi rwl\rho_{PS}}{3sin60°} = 1.21rwl\rho_{ps} \tag{6.3}$$

From the SEM images, the particle number on the surface of the cantilever can be counted. Taking the SEM image shown in Figure 46c as example, the size of imaged area is 36.8×27.5 µm^2 and I counted about 7340 particles on the surface. These particles have a radius of 191 nm. For the same area the particle number calculated by equation (6.1) is 8096. The counted particle number is about 10% less than the calculated particle number, since the monolayer has cracks and defects.

Table 1: The mass of PS colloidal monolayers on both sides of cantilevers calculated from SEM images (m_1) and from the shift in the resonance frequencies (m_2) for three representative cantilevers. In addition, the resonance frequencies of the cantilever before coating (f_0) and after (f_1) coating on both sides are listed. The error of the PS mass m_2 is calculated based on error propagation of the resonance frequencies used in equation (2.16).

	f_0 /Hz	f_1 / Hz	m_1 / ng	m_2/ ng
non crosslinked	13018	12509	22.7	21.8 ± 0.4
1% crosslinked	8994	8061	44.2	44.1 ± 0.3
10% crosslinked	10476	9682	35.2	36.1 ± 0.4

The mass calculated from the shift in resonance frequency and the mass calculated from the geometry of a closed-packed monolayer agree within 4% with no systematic deviation towards higher or lower mass loadings. Therefore we conclude that the colloid monolayer deposition method results in homogeneous and reproducible layers. Furthermore the agreement of the mass loading determined by the resonance frequency change and the SEM imaging indicates that the contribution of the colloid particle monolayer to the elasticity of the coated cantilever is negligible. In other words, the elastic properties of the deposited particle monolayer do not increase the spring constant, despite the fact that its thickness is comparable to the thickness of the cantilever. This finding is not surprising. The particles in the monolayer only have small contact areas with their neighboring particles

6.1.2 Thermomechancial Properties of PS Colloidal Monolayers

Before studying the film formation upon heating the performance of the bare silicon cantilever is tested first. During heating from 23°C to 210°C the resonance frequency decreases linearly with temperature with a slope of-0.24 Hz/K (Figure 50). The resonance frequency shift is completely reversible upon cooling.

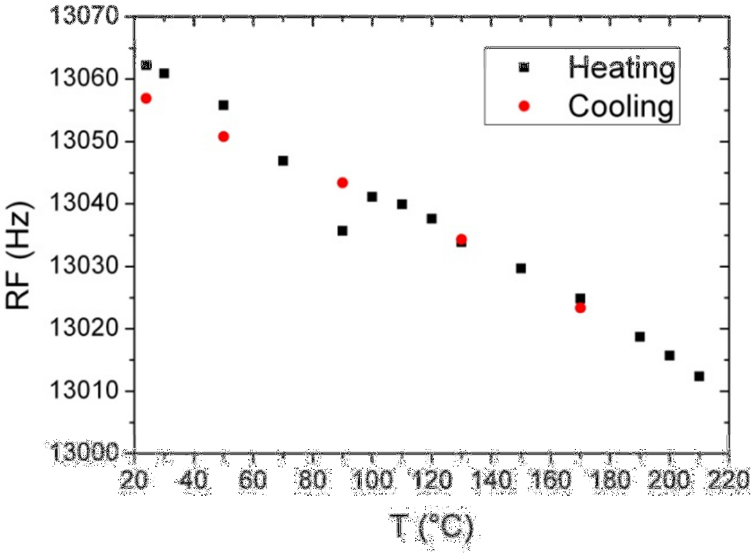

Figure 50: Resonance frequency of blank cantilever measured during thermal annealing plotted against temperature (error: ± 5 Hz).

The PS colloids are heated from ambient temperature to 800°C during the thermal gravimetric analysis (TGA, Figure 51). There was no weight loss of the colloids up to 380°C, which indicates there is no left over solvent from the synthesis in the particles. The particles decompose at temperature of 380°C.

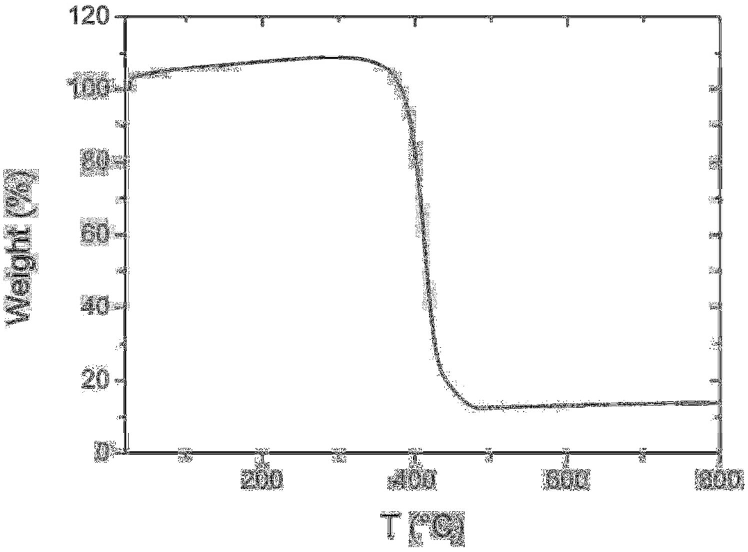

Figure 51: TGA result of the non-crosslinked PS colloids.

To study the film formation, the non-crosslinked PS colloidal monolayers coated on a micromechanical cantilever array are heated from room temperature up to 210 °C and then cooled down to room temperature. The corresponding resonance frequency curve (Figure 52) is not reversible upon heating and cooling during the first cycle.

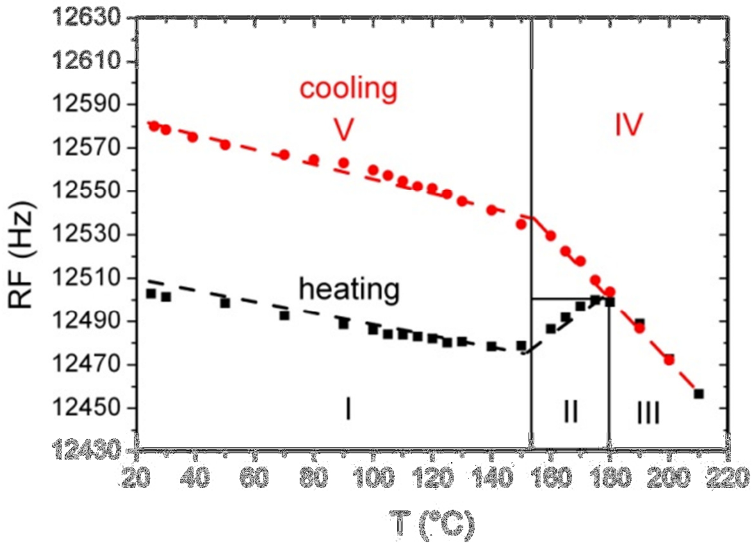

Figure 52: Resonance frequency of a representative cantilevers coated both sides with non-crosslinked PS colloidal film as function of temperature during the thermal annealing.

The resonance frequency shift during the heating can be divided into three regimes (Figure 52, data points in squares). From 25°C to 150°C (regime I) the resonance frequency decreases linearly with temperature at a rate of -0.22±0.06 Hz/K. This is related to the decrease of the *Young's* modulus of silicon.

In regime II, from 150°C to 180°C the resonance frequency increases with a slope of 0.67±0.05 Hz/K. I attribute the transition regime II to the onset of softening of PS.[85] At this temperature the PS colloids start to merge and form mechanical bridges. The increase in resonance frequency upon heating indicates an increasing contribution of the PS colloids to the mechanical properties of the cantilever, as we can exclude a mass change at these temperatures according to the TGA.

To better understand the increase of resonance frequency induced by mechanical coupling between PS colloids, FE simulation of the resonance frequency of a cantilever coated with PS colloidal monolayers on both sides is carried out by Sascha Pihan. By introducing friction at the colloid contact areas an increase in resonance frequency is obtained (Figure 53), which explains the increase of resonance frequency the coated cantilever in the regime II.

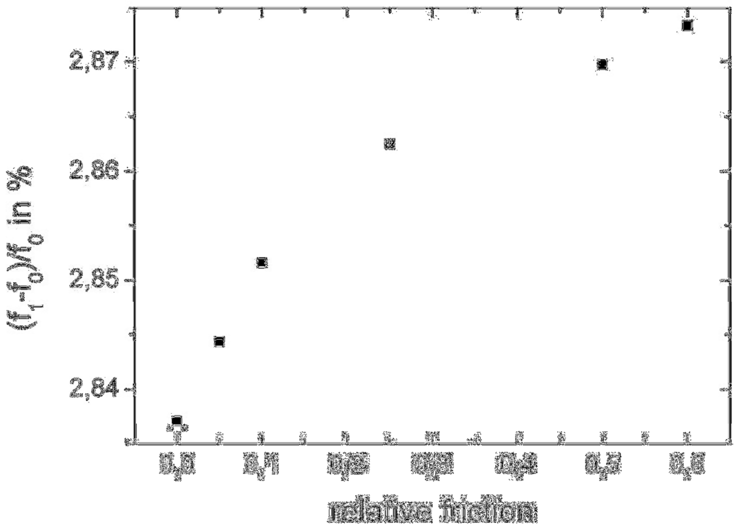

Figure 53: FE simulation of the resonance frequency shift upon increasing the friction between the colloids. Figure reprinted by permission from Sascha Pihan

During the softening of PS the mechanical bridges between the particles can be formed, which is mainly due to the entanglement of PS chains cross the particle-particle interfaces (Figure 54).[85b] Hence the voids between the PS colloids are filled and a homogenous PS film is formed from the colloidal monolayer. At 180°C, the end of the regime, the resonance frequency of the cantilever induced by mechanical coupling reached the maximum, which indicates a complete film formation. This can be confirmed by the SEM images carried out for the sample (Figure 55) after it is cooled down to the ambient temperature. The PS film is smooth and does not show any remains of the particles.

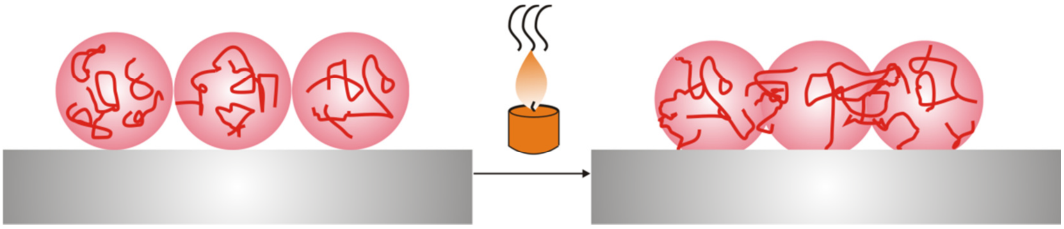

Figure 54: Illustration of the PS chains crossing the interfaces between the colloids upon heating.

In regime III (180°C to 210°C) the resonance frequency decreased again, this time with a slope of -1.45±0.07 Hz/K. The fast resonance frequency decrease in stage III can be addressed to the steep decrease of the *Young's* modulus of the formed continuous PS film above the glass transition temperature T_g, which decreases from ~3 GPa ($T<T_g$) to ~0.002 GPa ($T>T_g$) in the rubbery plateau. [86]

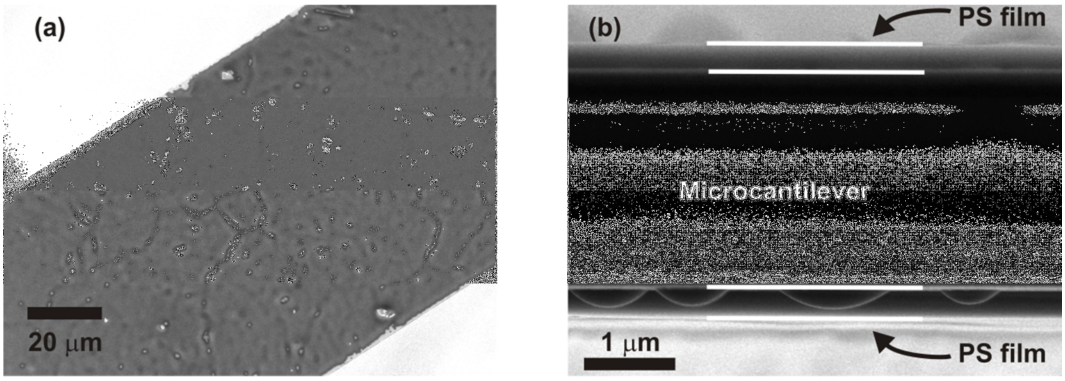

Figure 55: SEM images of film formed from non-crosslinked PS colloidal monolayer: (a): view from the top; b): view from the side.

The resonance frequency shift as a function of the *Young's* modulus of the coating material is simulated by FE analysis (Figure 56). Here, the mass of the coating material is kept constant. The negative shift of the resonance frequency is due to mass loading on the cantilever and the positive shift is due to the contribution of the coating material to the spring constant of the cantilever. At very low moduli ($E < 3$ GPa), the shift of the resonance frequency is negative. Due to the low moduli of the coating layer, the mass effect is dominant. For moduli higher than 3 GPa, the resonance frequency shifts to higher values since the average stiffness of the composite beam increases.

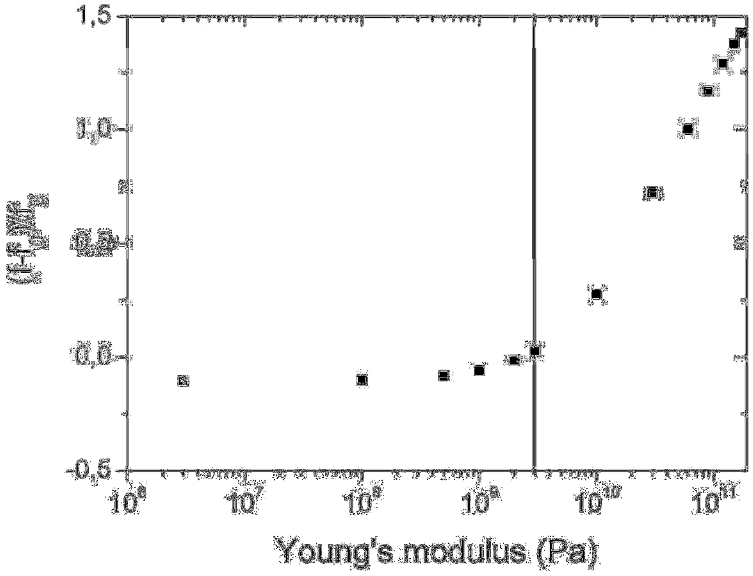

Figure 56: The resonance frequency shift as a function of the *Young's* modulus of the coating material. Figure reprinted by permission from Sascha Pihan.

During cooling the resonance frequency increases (Figure 52, data points in cycles) and can be divided into regime IV and regime V at a temperature of 150°C±5°C. The slope of the regime IV (T>150°C) was -1.45 Hz/K, which corresponds to the slope in the regime III. In both regime III and IV, the fast change of resonance frequency indicates that PS is in its viscoelastic state. The slope in the region V (T<150°C) is -0.34±0.07Hz/K, which is slightly higher than the slope in the regime I. In region V, the coating layer is a continuous PS film, which means the contact areas between the coating film and the cantilever is maximal. Therefore, the elastic property variation of PS upon temperature can be better transduced through the film to the cantilever than through the colloidal monolayer in regime I. The slow change of the resonance frequency signifies a glassy state of PS. The defined temperature of 150±5°C, which separates the regime IV and V, marks the transition of the homogenous PS film from a viscoelastic regime (regime IV) to the glassy regime (regime V).

In other words, the glass transition of the PS film is at 150°C±5°C, which is about 40°C higher than the T_g (95°C~105°C) of PS measured by differential scanning calorimetry.[87] It is not surprising since the heating process of PS in this work is accompanied by an external stress at a high rate - at the resonance frequency of the cantilever of about 12 kHz. As a consequence, the PS chains do not have enough time to move and to flow, so that they maintain their glassy state even at the temperature, which is higher than the conventional T_g. Hence, the glass transition of the polymers happens at a higher temperature, which is also by Jung et al by means of cantilever coated with poly(vinyl acetate).[70]

In order to investigate the shift of T_g at higher frequency, the frequency dependence of storage modulus G' and the loss modulus G"- also called master curve for the bulk PS sample is measured by classical dynamic mechanical analysis using an ARES rheometer. The moduli are measured as a function of frequency at various temperatures. The moduli versus frequency curves at different temperature are subsequently superposed as a master curve by means of frequency/temperature superposition.[86] From the master curve the temperature dependence of G' and G'' are recalculated both at 1 Hz and at 12 kHz (Figure 57).The T_g, at which G' and G" cross, is at 108°C±5°C for 1 Hz and increased to 135°C±5°C for 12 kHz. Taking the temperature gradient around the heating table (-5°C) and the heat transfer of the silicium cantilever to chip into account, I considered the T_g for PS obtained at 150 °C±5°C is reasonable.

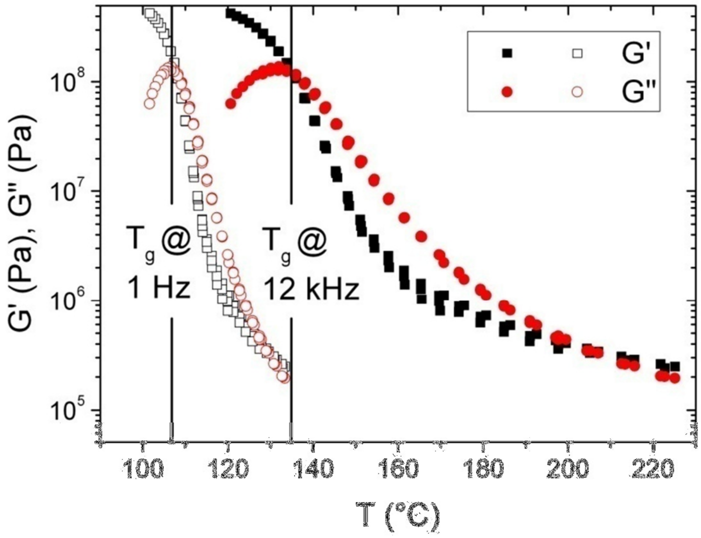

Figure 57: Master curve of non crosslinked PS colloids as a function of temperature, which corresponds to a frequency of 1 Hz (hollow data points) and 12 kHz (solid data points).

Heating this PS coated cantilever for a second time, the resonance frequency shift is reversible upon heating and cooling (Figure 58). Slopes in regime V (-0.35 Hz/K) and in regime IV (-1.54 Hz/K) are identical with the sloped in regime V and IV of the cooling curve obtained in the first cycle (Figure 52). In addition, both heating and cooling process reveal a change in slope at 152°C±5°C, which confirmed this measurement of the T_g of PS film is reproducible. The onset temperature of the film formation from the PS colloids corresponds to the T_g of formed PS film.

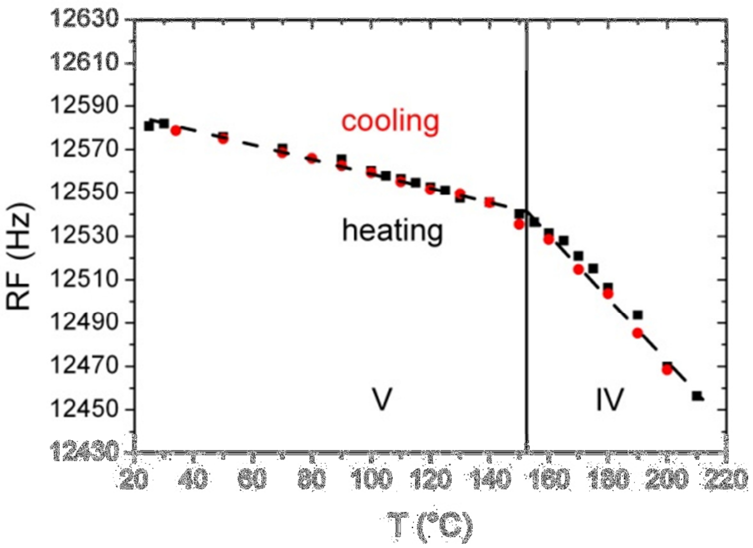

Figure 58: The resonance frequency shift of the cantilever coated with PS film formed from a PS colloidal monolayer during thermal annealing.

6.1.3 Calculation of *Young's* Modulus

After the first heating and cooling cycle, the resonance frequency of the cantilever coated with colloidal monolayers increases by 80 Hz at ambient temperature. The increase in resonance frequency is clearly due to the elasticity contribution of the PS film, e.g. the term E_1I_2 in equation (2.17):

$$f_2 = \sqrt{\frac{3(E_0I_0 + 2E_1I_2)}{nw(\rho_0h_0 + 2\rho_1h_2)}}$$

To study film formation of colloidal monolayer, equation (2.15) describes the cantilever coated with colloidal monolayer and equation (2.17) describes the cantilever coated with homogenous film, i.e. after film formation. The squared ratio of the two equations becomes

$$\left(\frac{f_2}{f_1}\right)^2 = \frac{E_0I_0 + E_1I_2}{E_0I_0} \tag{6.1}$$

Hence, the *Young's* modulus of the coating can be calculated from the ratio of the resonance frequencies

$$E_1 = E_0 \frac{I_0}{I_2}\left[\left(\frac{f_2}{f_1}\right)^2 - 1\right] \tag{6.2}$$

To calculate I_2 according to equation (2.18), the film thickness h_2 of the PS film after thermal annealing needs to be known. It can directly be determined from SEM images. It can also be calculated from the particle diameter h_1, assuming that a densely packed hexagonal monolayer of particles is at the surfaces and that the total volume of the polymer does not change during film formation. The volume V of the colloidal monolayer on a rectangular surface is a sum of all the particles volume:

$$V = NV_p = \frac{wL}{4(h_1/2)^2 sin60°} \times \frac{4}{3}\pi(h_1/2)^3 = \frac{\pi wLh_1}{6sin60°} \tag{6.3}$$

and if those colloids form a film owing the same length and width of the cantilever, the height of the film is expected to be:

$$h_2 = \frac{\pi h_1}{6sin60°} = 60\%h_1 \tag{6.4}$$

For the non crosslinked PS colloids, the diameters and thus h_1 is 382±13 nm. The continuous PS film after the annealing has a height h_2 of 257±10 nm according to the SEM image, which is 63% of the diameter of the PS colloids h_1 and is close to the expected 230 nm according to equation (6.4).

Using equation (6.2), a *Young's* modulus of 2.7 GPa is obtained for the PS film at ambient temperature. This is close to the bulk material of 3-4 GPa.[88] It is also possible to calculate the *Young's* modulus variation as a function of temperature. Here, the variation of resonance frequency of the cantilever induced by *Young's* modulus change of the silicon during temperature increase has also to be considered. As mentioned above, in the regime I the resonance frequency shift reflected mainly the decrease of the *Young's* modulus of silicon. To calculate the *Young's* modulus of PS from ambient temperature to T_g at 150°C with equation (6.2), the resonance frequency in regime I is set as f_1 and the resonance frequency in regime V is set as f_2

at each measured temperature. To calculate the *Young's* modulus of PS higher than T_g, the linear slope in regime I was extended linearly and the resonance frequency f_1 was read from the extension. For f_2 the resonance frequency in regime IV is used. The thus obtained *Young's* modulus of PS is plotted as function of temperature in Figure 59. It is obvious, the *Young's* modulus decreased slower before T_g is reached.

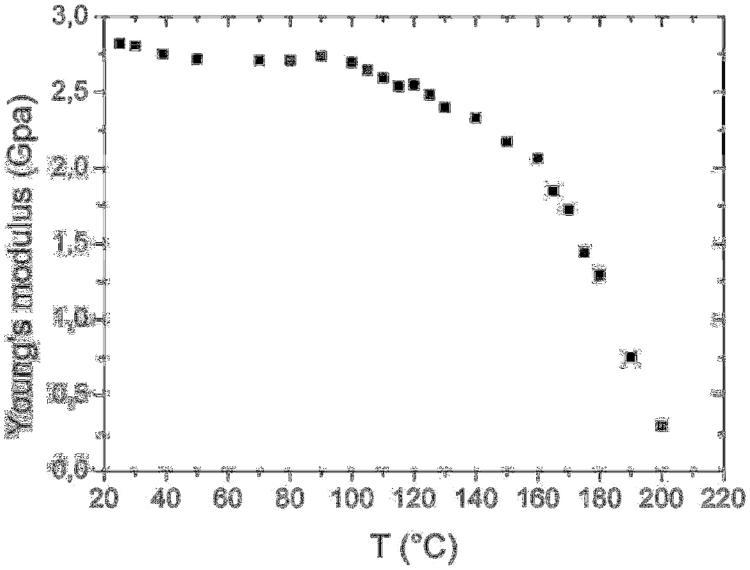

Figure 59: *Young's* modulus of the PS film as function of temperature.

6.1.4 Thermal Annealing of Cross-linked PS Particles

Crosslinked PS colloids are also used to coat the micromechanical cantilevers. The films formed from crosslinked colloids are crucial regarding applications in analytical and preparative separation technique and sensor technologies.[89] The crosslinked films offers several advantages over regular non-crosslinked polymeric coating, such as fast and reversible response to temperature variation and solvent[90] and controlled uptake and releases of drugs based on the expansion and collapse of the responsive polymers.[91]

For the synthesis of these particles, crosslinking agent divinylbenzene (DVB) is added to the emulsion. Inside each individual colloid, the PS chains are crosslinked with DVB. The crosslinking degree corresponds to the ration between the added styrene and DVB.

The film formation process of the crosslinked particles is also investigated by means of cantilever. Once the cantilevers are coated with colloidal monolayers of PS particles with 1% and 10% crosslinking on both sides, similar evolution of resonance frequency shift upon heating and cooling (Figure 60a, b) is observed. The temperatures marking the onset and end of the film formation shifts to higher temperatures, which are 160°C±5°C and 190°C±5°C for the 1% crosslinked colloids and 170°C±5°C and 200°C±5°C for the 10% crosslinked colloids, respectively. The glass transition temperature increases with crosslinking degree since the relaxation of the polymer chains is limited by the crosslink agent.[92]

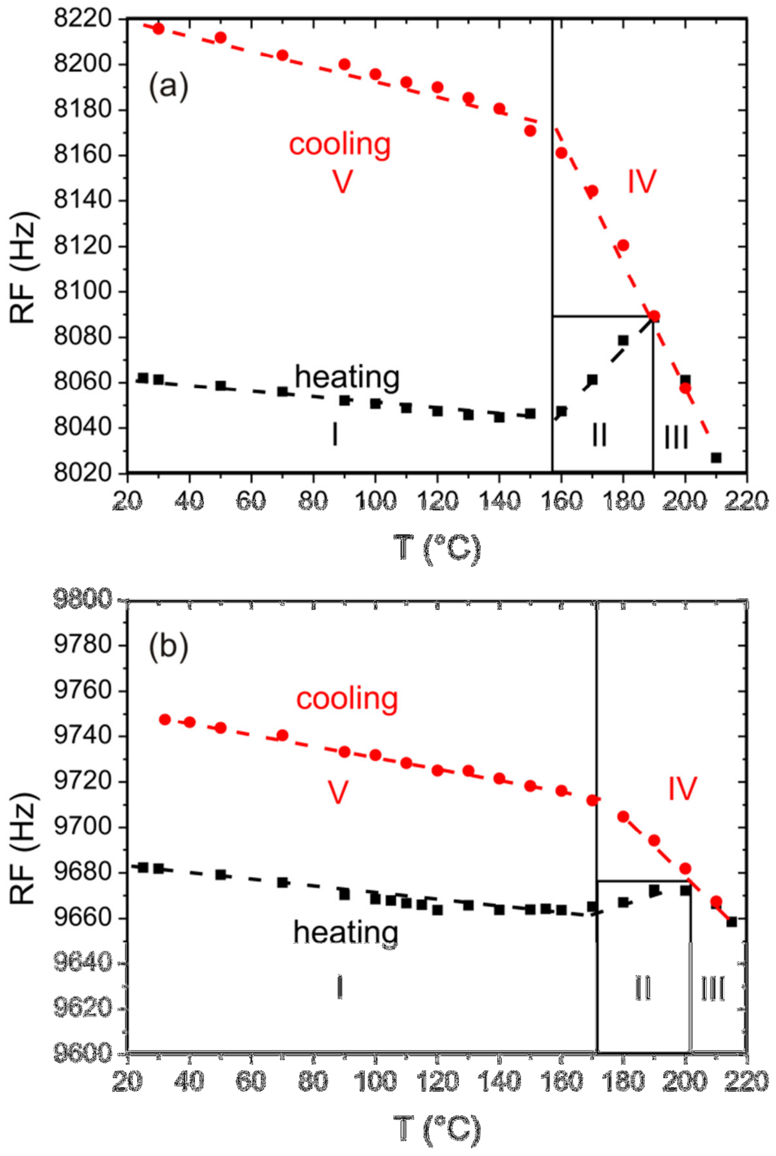

Figure 60: Resonance frequency of cantilevers coated both sides with 1% crosslinked (a) and 10% crosslinked (b) PS colloidal film as function of temperature (error: ± 5 Hz).

The films formed after the heating and cooling cycle (Figure 61) are not homogenous. The colloids are deformed but the boundaries between the colloids are still visible. The colloids are kept in form by the crosslinking agents; the deformation of the colloids takes place during heating due to the expansion of the colloids. During cooling the volume of the colloids actually decreases but the deformation is not reversible. Despite of the crosslinking, there are still some PS chains which can diffuse out of its own colloids and either enter the other colloids or entangle with PS chains in the other colloids in the vicinity. The interaction between PS chains from different colloids keeps the deformation of the colloids. The deformation of the higher crosslinked colloids are more limited by the crosslinking agent than the lower crosslinked colloids.

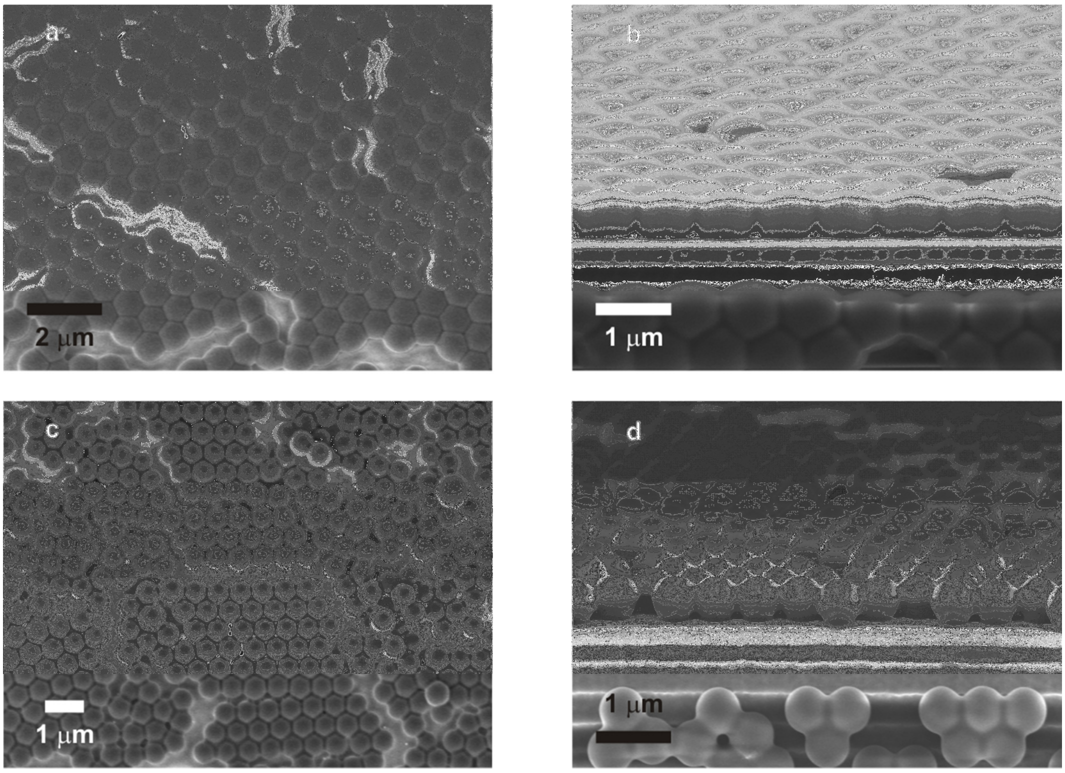

Figure 61: Film formed from 1% crosslinked PS colloidal monolayer (a, b); film formed from 10% crosslinked PS colloidal monolayer (c, d).

6.1.5 Estimation of *Young's* Modulus of Crosslinked PS Films

The film thickness h_1 of the colloidal monolayer and the thickness h_2 of film after thermal annealing for both 1% and 10% crosslinked PSs are listed in Table 2.

Table 2: Film thickness of PS coating layers, before (h_1) and after (h_2) annealing.

	h_1/nm	h_2/nm
1% crosslinked PS	775 ± 35	713 ± 26
10% crosslinked PS	619 ± 25	567 ± 30

For the 1% and 10% crosslinked colloids, the height of the films was about 92% of the diameter of the original particles, which does not satisfy the prediction by the equation (6.4). In the case of 1% crosslinked PS colloids, the voids between the colloids are almost completely filled (Figure 61a, b).As for 10% crosslinked PS colloids, the voids between the colloids are only partially filled (Figure 61c, d). The wavy surface of these films also gives considerable error to define their height.

The *Young's* modulus of the film formed from crosslinked PS is lower than the modulus of the non crosslinked PS film. According to the equation (6.2), they have the values of 1.3 GPa and 0.8 GPa for the 1% crosslinked PS and 10% crosslinked PS, respectively. It is already reported that the film formed crosslinked colloids are brittle and has a lower mechanical strength by measuring the mechanical properties of the film in bulk by means of dynamic mechanical analyzer.[93] This is explained by the lack of the interface diffusion of the polymer chains between the crosslinked colloids. In crosslinked colloids, the mobility of polymer chains is reduced since the crosslinker hold the polymers together.

6.1.6 Film formation via Organic Vapor Annealing

Organic vapor annealing is an alternative method to induce the film formation from a colloidal monolayer, in case the specimen should be annealed at temperature lower than T_g.[79b] Toluene is a good solvent for PS and therefore has been chosen to anneal

PS colloids. To be able to compare with data reported in literature, I introduce here the activity a of toluene, which is defined as the ratio between the used vapor pressure p to the saturated vapor pressure at 20°C of toluene p_{sat}:

$$a = p/p_{sat} \tag{6.1}$$

The first film formation via organic vapor annealing is carried out at activity a of toluene at 1.

Here, the resonance frequency of cantilever coated on both sides with PS colloidal monolayers is monitored during the toluene vapor exposure. First, the resonance frequency decreases by 220 Hz as the cantilever (Figure 62, striped region). The decrease is steep during the first 25 minutes. Then it becomes less steep and reaches a constant plateau at 150 min. After this plateau is reached, air is pumped into the sample cell to dry the film (Figure 62, blank region). After an initial sharp increase (170 min-250 min) the resonance frequency rises only slowly with time to a value 40 Hz higher than the initial resonance frequency before annealing.

Compared to the thermal annealing process the reasons for the resonance shift during toluene vapor annealing are more complex. The colloids absorb toluene molecules from the vapor phase and thus the mass of the coating layer increases, which reduces the resonance frequency of the cantilever. In addition, the mechanical properties of the colloids changes due to the plastifying (softening) effect of toluene on PS. The particles becomes soft and starts to merge together to form a film. This also gives a shift of the resonance frequency. However, these both changes taking places at the same time and the detected resonance frequency shift is induced by both effects and cannot be separated from each other.

The resonance frequency f_1 of cantilever coated with PS colloidal monolayer on both sides is 11.89 kHz and the resonance frequency f_2 of cantilever after annealing was 11.93 kHz. The increase of the resonance frequency after drying can be explained by the film formation of the colloidal monolayer. Hence the spring constant of the cantilever increases and therefore the resonance frequency.

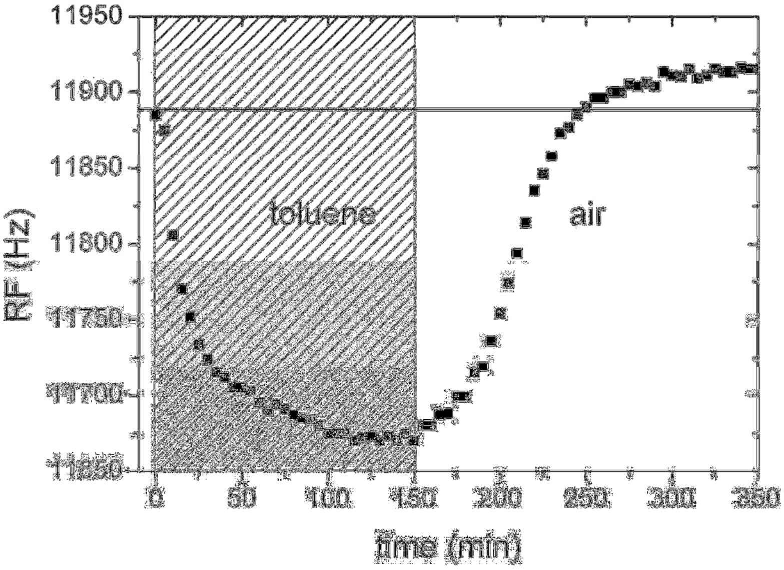

Figure 62: Resonance frequency variation of cantilever coated with PS colloidal monolayer during exposure to toluene and air plotted against time.

The SEM image of the cantilever after the vapor annealing reveals a homogenous coating layer of PS on the cantilever. Compared to the PS film formed via thermal annealing, the PS film formed via organic vapor annealing is even more homogenous, which means the film is without any cracks and voids. The *Young's* modulus of the homogenous film can be calculated according to equation (6.2)and has a value of 1.5 Gpa, which is about 1.2 GPa lower than the film (*Young's* modulus=2.7 GPa) formed from thermal annealing from the sample colloids. The film thickness is 350 nm ± 29 nm and is about 100 nm thicker than the thermal annealed PS film. It is already reported by Zhang et al[23c] that about 10% toluene stays in PS film after drying with N_2overnight. The lower *Young's* modulus and the larger thickness of the film can be attributed to the residual toluene.

Knowing the amount of the residual toluene in the film, the *Young's* modulus of the PS film can be estimated more precisely. For the case that only the mass has an effect on the cantilever during the toluene exposure, the resonance frequency of the cantilever after drying should decrease from 11.89 kHz to 11.85 kHz due to the residual toluene, while the mass of PS does not change. Taking 11.85 kHz forf_1, a *Young's* modulus of 2.3 GPa is obtained for the PS film according to the equation

(6.2). This value is still lower than the *Young's* modulus of thermal annealed PS film and it is due to the plastifying effect of the residual toluene in the film.

6.1.7 Toluene Absorption of PS Colloids

The frequency shift of cantilever coated with PS colloidal monolayer during exposure to toluene vapor is induced both by toluene uptake and spring constant shift of the cantilever due to the coupling of the homogenous polymer film to cantilever. To separate the two effects, the mass change of PS colloids upon absorption of toluene is studied first. For this purpose, the end-coated cantilevers are prepared as introduced in the section 5.3. When the cantilever is only coated at the end (Figure 15 a), the change of the elasticity of the cantilever upon coating is negligible [44b, 45] and the resonance frequency shift reflects only the mass change of the cantilever. Hence the resonance frequency shift reflects only the mass increase of the PS during toluene uptake. To calculate the mass loading for end-coated cantilever, n in equation (2.16) takes the value 1.

A blank cantilever with resonance frequency f_0 of 29866 Hz is coated with PS colloids at the end and hence the resonance frequency f_1 reduces to 28406 Hz (Figure 63). According to the equation (2.16) the mass of the PS colloids is 16 ng. During the exposure to toluene with the activity a at 1, the resonance frequency shifts further to lower values (f_2=27774 Hz) due to the absorption of toluene in PS colloids. The absorbed toluene calculated with is 8 ng.

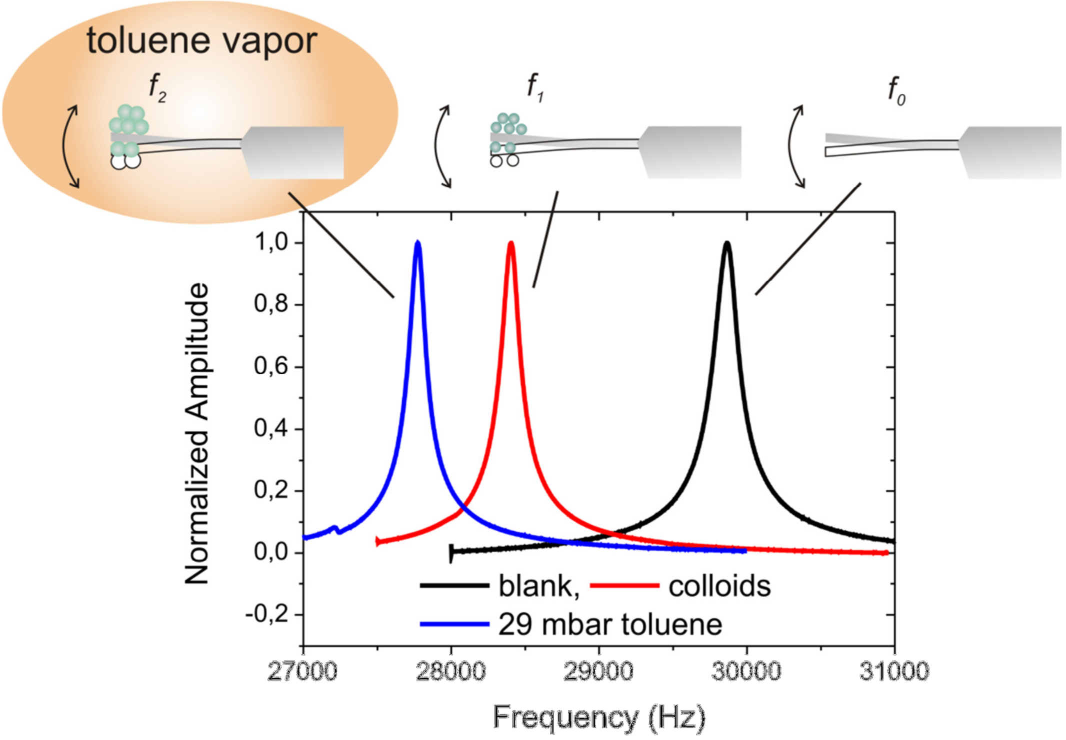

Figure 63: Resonance frequency measurement of blank cantilever (black curve), cantilever coated with PS colloids at the end (red curve), and cantilever with swollen PS colloids during exposure to toluene vapor (blue curve).

To be able to compare the amount of toluene absorbed by different colloids, the relative mass increase (RMI) is introduced, which is defined as the ratio of the mass of colloids and toluene together to the colloids:

$$RMI = \frac{m_{PS} + m_{toluene}}{m_{PS}} = \frac{f_0^{-2} - f_2^{-2}}{f_0^{-2} - f_1^{-2}} \qquad (6.2)$$

The RMI of the representative cantilever (Figure 63) is (16+8)/16 =1.5. The RMI of non crosslinked, 1% and 10% crosslinked PS colloids during exposure to toluene vapor (*a*=1) is recorded and the relative mass increase is obtained based on the resonance frequency measurements and plotted as a function of time (Figure 64). Two phases in the uptake of toluene can be identified. In the first 15 minutes the toluene uptake undergoes a fast process, the rate of toluene uptake is determined to be 6.7%/min. After 15 minutes till the 110 minute, the RMI is slowed down with a rate of 0.1%/min.

What factors influence the toluene uptake in PS? First, the diffusion of toluene in PS plays an important role and it has been already investigated by different methods, for instance by pulsed-field-gradient spin-echo NMR[94] forward recoil spectroscopy,[95] gravimetric sorption [96] and magnetic resonance imaging.[97] The diffusion coefficients obtained from these experiments vary from 10^{-10} to 10^{-17} m^2/s in dimension. Roughly, toluene molecules need 1 s up to 80 s to go through a distance of 400 nm, which is the diameter of the non crosslinked PS colloids. However, the RMI needs much longer (about 120 minutes) to reach the maximum. It is obvious that the diffusion of toluene in PS is not the only factor has to be considered for the toluene uptake of PS. During the toluene uptake, PS experienced the transition from glassy state to viscoelastic state. In viscoelastic state the polymers relax and the polymer relaxation is a slow process which also influences the transport of solvent molecules.[98]

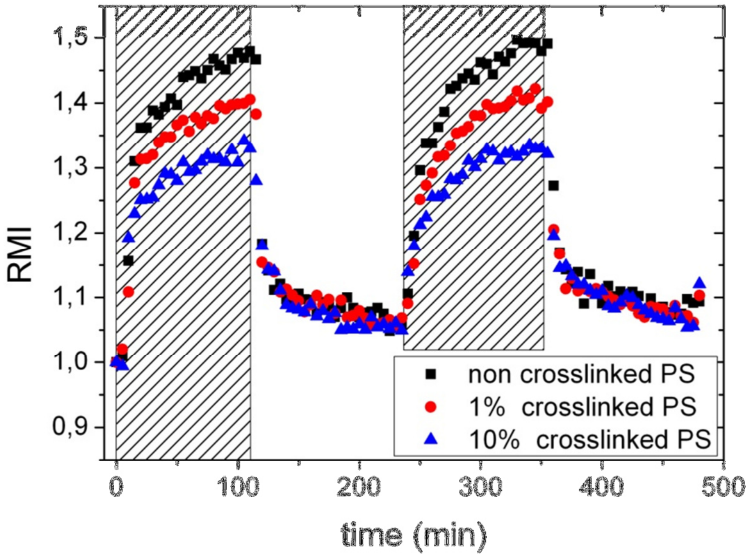

Figure 64: Relative mass increase (RMI) of non crosslinked PS particles (black squares), 1% crosslinked PS particles (red spheres) and 10% cross linked PS particles (blue triangles) during exposure to toluene with vapor pressure at 29 mbar plotted as function of time.

The two regions of toluene uptake can also be recognized in the resonance frequency shift of cantilever coated with PS colloidal monolayer during exposure to toluene (Figure 62). The first region, where the fast uptake of toluene takes places, takes 25 minutes for the monolayer. The same process for end coated PS takes only 15 minutes. In both case, the increase of mass on the cantilever reduces its resonance frequency. In case of monolayer, as we have learned from the study of film formation via thermal annealing, the resonance frequency increased during the film formation. The two contra effects of toluene uptake in the monolayer on the cantilever can be the reason for slower process of resonance frequency shift.

The mass fraction of absorbed toluene to PS decreases with increasing crosslinking degree, which has already been observed by other scientists,[92, 99] since the higher the crosslinking degree, the less flexible are the polymer chains, which decreases the possible space to uptake the toluene.

To have a quantitative estimation of the toluene uptake of the PS colloids, the half-time of the three particles is during toluene uptake is introduced. The half-time is defined as the time the particles need to reach the half of the maximum of the RMI. The half-time of non-crosslinked and 1% crosslinked PS colloids is 10 minutes and of the 10% crosslinked colloids is 9 minutes.

6.2 Static Mode

By measuring the resonance frequency of the end-coated cantilever, the toluene uptake of PS induced resonance frequency can be estimated. The next effect has to be studied is elastic property change in the film during the film formation via organic vapor annealing. The deflection of the cantilever is very sensible of the elastic property change of the cantilever (E_0) according to the equation (2.19) for thin coating layer and equation (2.20) for thick coating layer.

$$\sigma = \frac{E_0 h_0^2}{6(1-\upsilon_0)} \cdot \frac{2Z}{Z^2 + L^2} \tag{2.19}$$

$$\sigma = \frac{E_0 h_0^3}{6(1-\upsilon_0) h_1^2 (1 + h_0/h_1)} \cdot \frac{2Z}{Z^2 + L^2} \tag{2.20}$$

As we have learned from the study of the resonance frequency shift upon film formation of the colloids monolayer via thermal annealing (section 6.1.2), the spring constant and therefore also the *Young's* modulus of the cantilever increases during the film formation. This should be detectable by measuring the deflection of the cantilever.

The deflection of cantilever coated with non crosslinked, 1% crosslinked and 10% crosslinked PS colloidal monolayer is recorded during toluene vapor annealing first with toluene activity *a* at 1.

6.2.1 Non crosslinked PS Colloidal Monolayers

First I would like to discuss the case of non crosslinked PS colloidal monolayer during toluene uptake (Figure 65a, striped regions). During each toluene exposure, three phases in the uptake of toluene can be identified. The first two fast phases for the first cycle are shown in the close-up view (Figure 65b). In the first 3 minutes, the cantilever bends about 40 nm away from the colloidal monolayer. Between 3 and 50 minutes, the cantilever bends towards to the coating layer and bends over the zero deflection to a higher position, indicates that the cantilever is already deformed after the coating with colloidal monolayer. This can be induced by the capillary force between the coating layer and the cantilever, which bends the cantilever to the coating layer. In the following time (50-120 minutes) the deflection of cantilever is almost constant at about 350 nm.

Deflection in the first cycle (40 nm) is much lower than in the cycles afterwards (350 nm). This effect can be addressed to the film formation in the first cycle, which is confirmed by SEM image (Figure 66). Before the continuous film forms, the volume increase of the colloids induced by uptake of toluene cannot exert all the expanding stress in the monolayer to bend cantilever. Here, the contact between colloids and cantilever is confined. After film formation, the force can be transferred to cantilever completely due to the well accomplishes contact area of coating layer and cantilever. Since film formation is complete after the first cycle exposure to toluene vapor, the deflection curves of cantilever are identical for the following cycles and this fact reflects a continuous film behavior of PS during solvent vapor annealing.

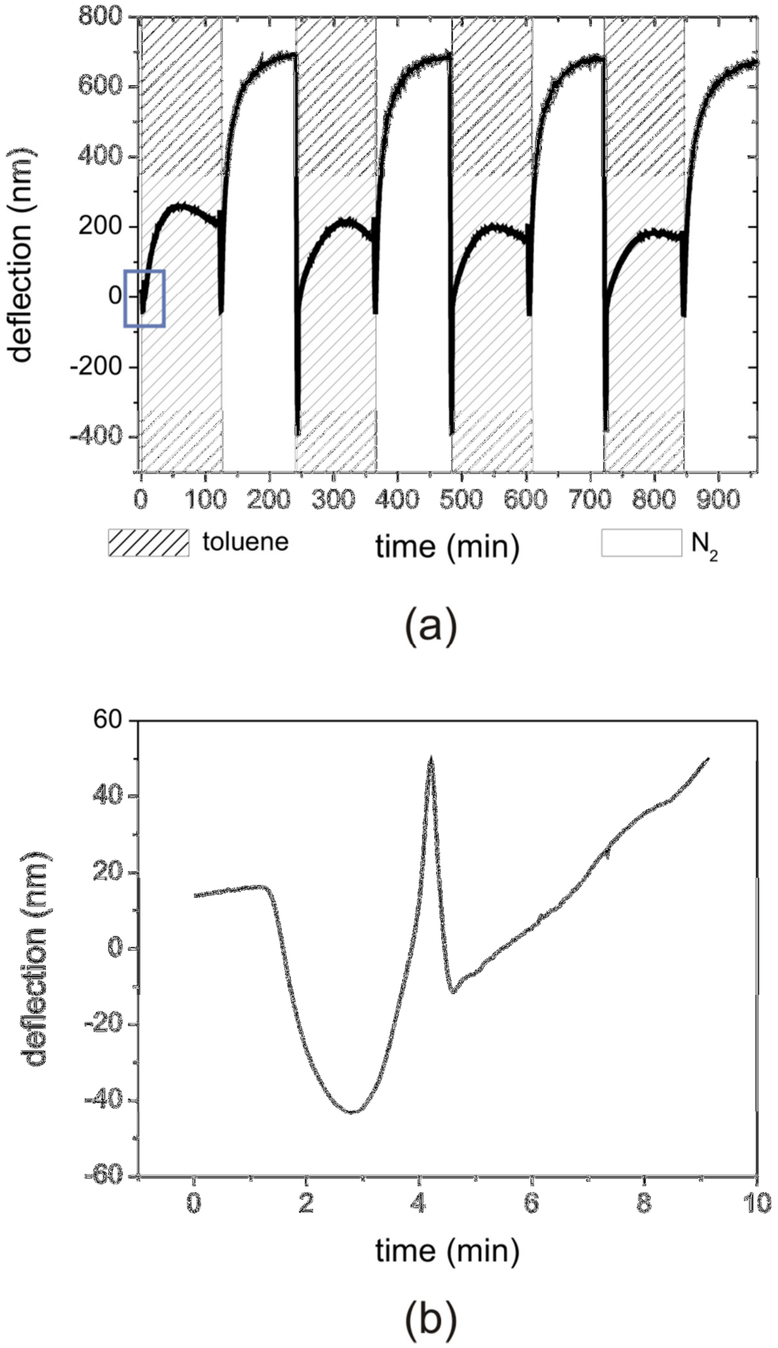

Figure 65: (a) Deflection of a cantilever coated with non crosslinked PS colloidal monolayer during toluene exposure(b) the close-up view of the highlight region in (a).

The bending of the cantilever is affected by three contributions. First, the expansion of colloids in volume upon uptake of toluene induces compressive stress in the film and bends the cantilever away from the monolayer. Second, the stress in the film relaxes since the free volume in the colloids increases by absorption of toluene molecules. Hence the polymer chains can move more easily and hence rearrange into a configuration of lower energy. As a consequence, the amplitude of deflection of the cantilever reduces. Third, as a result of the plasticization (softening) of PS upon absorption of toluene molecules, the stress in the film cannot be transduced to the cantilever, which means the stress cannot bend the cantilever anymore.

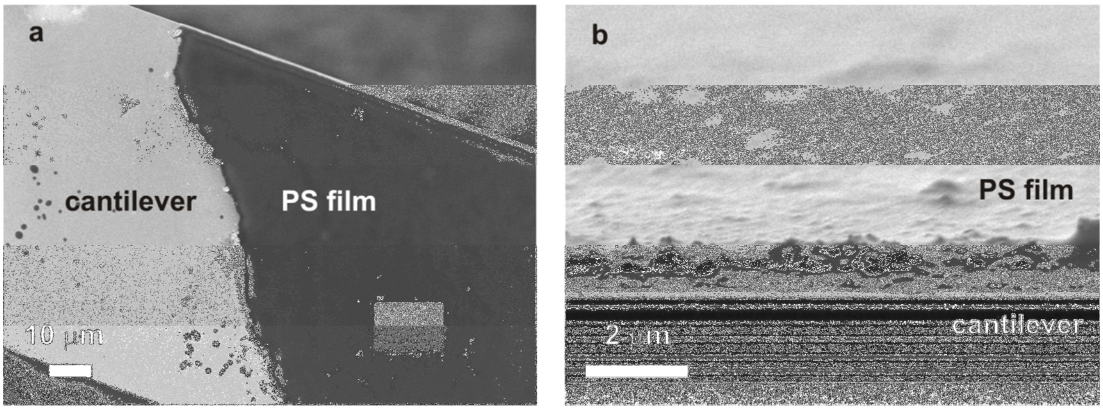

Figure 66: SEM images of the formed PS film upon toluene vapor annealing (a) the top view, bright part is the cantilever and dark part is the PS film; (b) the side view.

The deflection evolution of the cantilever is therefore dependent on the rate/duration of the three processes. It is complicated to analyze all the three effects together, so first only two effects were considered: the sorption effect and the relaxation effect. These two effects can be easily recognized in the deflection process, because they bend cantilever in opposite direction. If we assume a sorption time τ_s for the sorption process and a relaxation time τ_r for the relaxation process, Wenzel et al.[54] have suggested that for low sorption ($\tau_s < \tau_r$), the formed stress can be always considered at its relaxed state and the deflection history reflects the absorption history (Figure 67, τ_s =30 s, 60 s); for fast sorption ($\tau_s > \tau_r$), the cantilever bends to a maximum position due to the sorption of target molecules (Figure 67, τ_s =5 s, 10 s). Meanwhile a buildup of the unrelaxed stress can occur and the deflection reduces as a result of the relaxation of the stress.

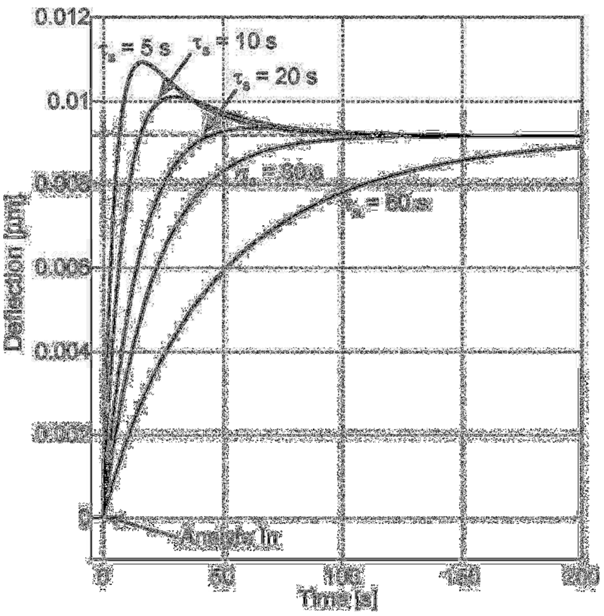

Figure 67: Calculated deflection response for a polymer coated cantilever during the absorption of target molecules for various sorption time with constant relaxation time.[54]

The relaxation process and the plasticization process are hard to separate since they accompany each other and both effects bend cantilever in the same direction, namely to the coating layer. Also, the plasticization process can accelerate the relaxation process. To simplify the interpretation of the data, I first considered these two effects together and introduced a definition of effective relaxation time to describe the duration of the combined process. The effective relaxation time is read as the time, the cantilever needed to bend from the maximum deflection back to the zero stress state.

For the non crosslinked PS film, overshoots are observed in the deflection evolution for each cycle (Figure 65), which indicates for the non crosslinked PS film, the sorption process is faster than the relaxation process. Also the effective relaxation time was constant in each cycle, which took 55±5 minutes. The dimension of time here is in minutes, which is much longer than the simulation data shown in Figure 67 with dimension of time in second. The simulation is carried out for a completely different system: the coating layer is polyisobutylene, and the cantilever is exposed to various hypothetical analytes and the parameter used for the simulation such as the diffusion coefficient of the analytes in the coating layer is also hypothetical.

After the overshoot, the cantilever bends back to the initial deflection, since the stress relaxed to zero. The zero stress state has also been observed during heating of PS film on a cantilever to about 103°C by Jung et al.[69b] The glass transition of the PS with T_g at 103°C is suggested to be the reason for the zeros stress. Glass transition of a polymer can also be induced by absorption of a good organic solvent vapor, the glass transition of PS induced by sorption of toluene has already been observed at toluene activity of 0.4.[100]

I suppose that the zero stress state observed in this work for the PS film during the toluene exposure is also a result of the glass transition of PS, induced by toluene vapor absorption. The deflection of the cantilever is plotted against temperature in Jung's work. In my work, the deflection of the cantilever is plotted against exposure time. The temperature, at which the zero stress state starts, is considered as the T_g of the coating layer by Jung et al. Therefore, the exposure time, at which the zero stress state starts in this work, is considered as the glass transition time t_g. This glass transition time gives the information about how long the film needs to be exposed to toluene vapor to reach the glass transition. The corresponding mass of absorbed toluene, which is necessary to induce the glass transition of PS, can be read from the RMI (black) curve shown in Figure 64:at t=8 minutes, the mass of toluene in the coating layer is about 10% relative to the polymer mass. In other words, the non crosslinked PS film undergoes the glass transition, when the mass of absorbed toluene in the film reaches 10% of the mass of the film.

During the drying process of non crosslinked PS (Figure 65a, not striped regions), cantilever bends away from the PS film very shortly to position zero and then towards the coating layer with an amplitude of about 700 nm. At the beginning of the drying process toluene molecules left the PS film, the film became harder; hence the residual compressive stress in the film can be transduced to bend the cantilever away from the coating layer. After this fast process, the tensile stress in the film during the drying process bent the cantilever towards PS film. The toluene release process of PS film is identical for every cycle.

6.2.2 Crosslinked PS Colloidal Monolayers

As shown in the last section, information about the sorption and effective relaxation time of the polymer coating film during exposure to organic solvent vapor can be obtained by measuring the deflection of the cantilever. In addition, the amount of toluene to induce the glass transition the polymer can be estimated. In this section, the deflection of cantilever coated with 1% and 10% crosslinked PS colloidal monolayer is measured and the results will be discussed.

The deflection of the cantilever coated with monolayer consisting of 1% crosslinked PS colloids is shown in Figure 68a. In the first cycle of exposure to toluene (striped regions) cantilever bends first away from monolayer for 16 minutes to reach the deflection maximum of 850 nm and in total 120 minutes till the cantilever bends to the zero stress state. The corresponding amount of toluene absorbed in PS film at t_g = 120 minutes is about 40% of polymer mass (Figure 64, red curve). After the first cycle exposure, a similar PS film as obtained from thermal annealing is formed (Figure 69 a, b). The SEM images show a flat PS film with hexagonal boundary between the particles. The voids between the colloids are mostly filled.

Also overshoots of the deflection are observed for the measured cycles. This fact indicates that the 1% crosslinked PS film also has a longer sorption time than effective relaxation time. However, the effective relaxation time is shortened from in each cycle, concretely from 105 minutes in the first cycle to 50 minutes in the second cycle, to 40 min in the third cycle and finally to 25 min in the fourth cycle. The larger decrease of effective relaxation time from the first cycle to second cycle is due to film formation in the first cycle. In the first cycle, the film formation takes place, more precisely for crosslinked PS, the particles swell due to absorption of toluene and start to merge and connect to each other. Owing to the crosslinkers in the polymers, the mobility of the polymers is confined compared to the non crosslinked polymers. Despite of the film formation, the maximum deflection is reached in the first cycle. Also the relaxation of the polymer is hampered by the crosslinkers, which explains the significant long relaxation time in the first cycle. The shortened relaxation time in each cycle means the relaxation became faster in each cycle. Probably, the film formation is not complete after two or three time toluene vapor annealing. With each additional toluene exposure, the connection between the deformed particles increases and hence benefits the relaxation of the polymers.

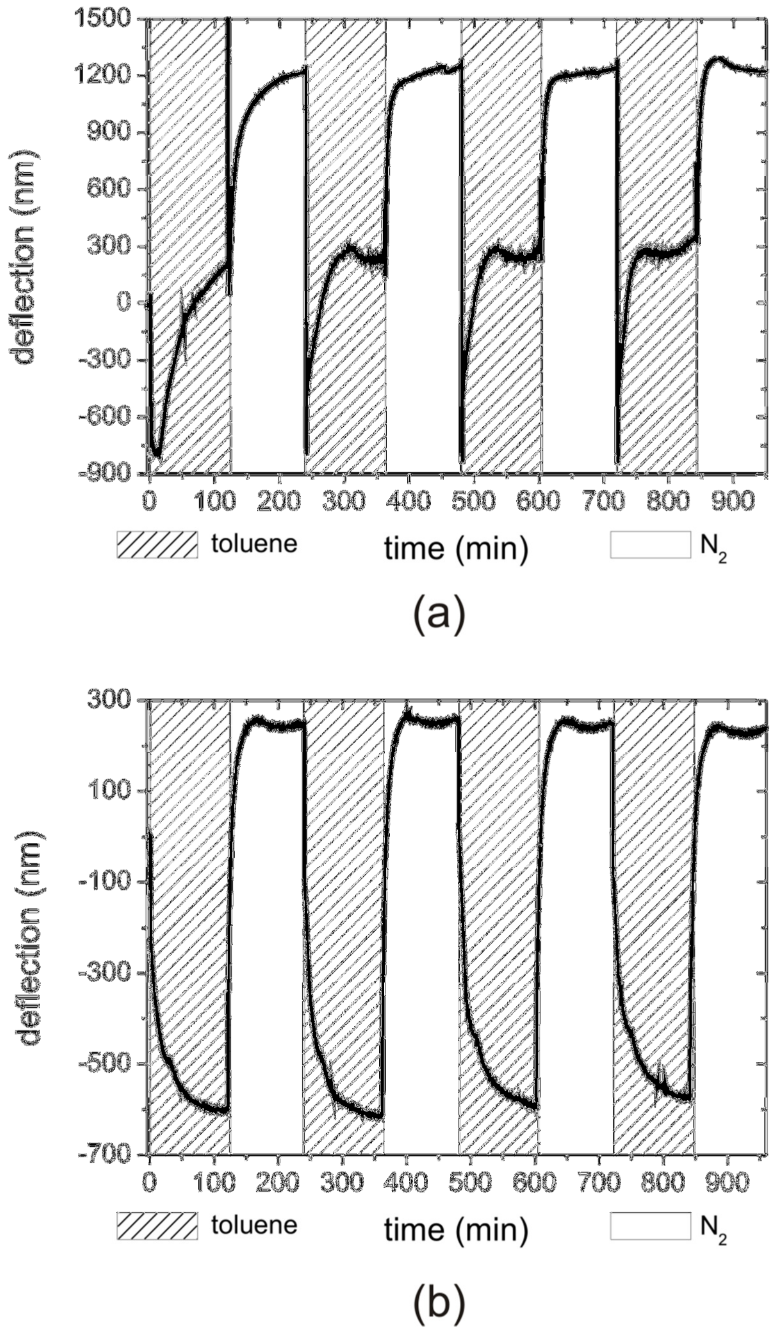

Figure 68: Deflection of cantilevers coated with a) 1% crosslinked and b) 10% crosslinked PS colloidal monolayer during exposure to toluene.

With decrease in effective relaxation time, the t_g of the colloidal film also decreases. The corresponding amount of toluene absorbed in PS decreased from 35% in the second cycle to 20% in the fourth cycle. In summary, the amount of toluene for the film to reach glass transition decreased with increasing exposure cycles.

As for the 10% crosslinked colloidal monolayer, the observed deflection curves (Figure 68b) are different than those of non- and 1% crosslinked PS monolayer. The cantilever bends the whole two hours away from the colloidal monolayer and the deflection trend stays the same. The plasticization does not take place in the 10% crosslinked film, since the cantilever does not bend back to the stress zero state. The high crosslinking of the PS muss have prevented the softening of the PS, despite of the absorption of toluene.

Now there are only two processes need to be considered: the sorption process and the relaxation process. There is no overshoot of the deflection observed, which means that either the effective relaxation time is shorter than the sorption time or no relaxation took place. In order to assess whether the relaxation takes place, I compare the reflection curve and the mass increase curve (Figure 64, blue curve), since the sorption process correlates with the amount of absorbed toluene. The half-time of the deflection curve and the RMI curve can be obtained by fitting the curves with an exponential function and takes the value of 15 minutes and 9 minutes, respectively. Comparing to the mass increase, the deflection needed longer to reach the half amplitude, which can be the result of the relaxation of the polymer. The absence of overshoot indicates that the relaxation time is shorter than the sorption time.

This short relaxation process is not observed for non- and 1% crosslinked colloidal monolayer. On one hand the relaxation and the plasticization cannot be separated, on the other hand the sorption process was so fast that they cannot be compared with the mass increase of toluene in the film.

The SEM images of the film formed from 10% crosslinked PS particles show (Figure 69c, d) a wavy film and the colloids deformed from spherical to hexagonal. The side view shows that the spaces between the colloids are not all filled, since the crosslinks hampered the polymer to move cross the interfaces of the colloids. The short relaxation of the 10% crosslinked colloids may only occur inside each individual colloid, since the polymers were not able to move out of the colloids owing to the higher crosslinking degree. On the contrary, the PS in the non- and 1% crosslinked colloids can diffuse across the interface between two colloids, therefore the relaxations of the polymers take longer. In principle, the overshoots of the deflection curve observed for non- and 1% crosslinked colloidal monolayer signalize the diffusion of polymers cross the interfaces.

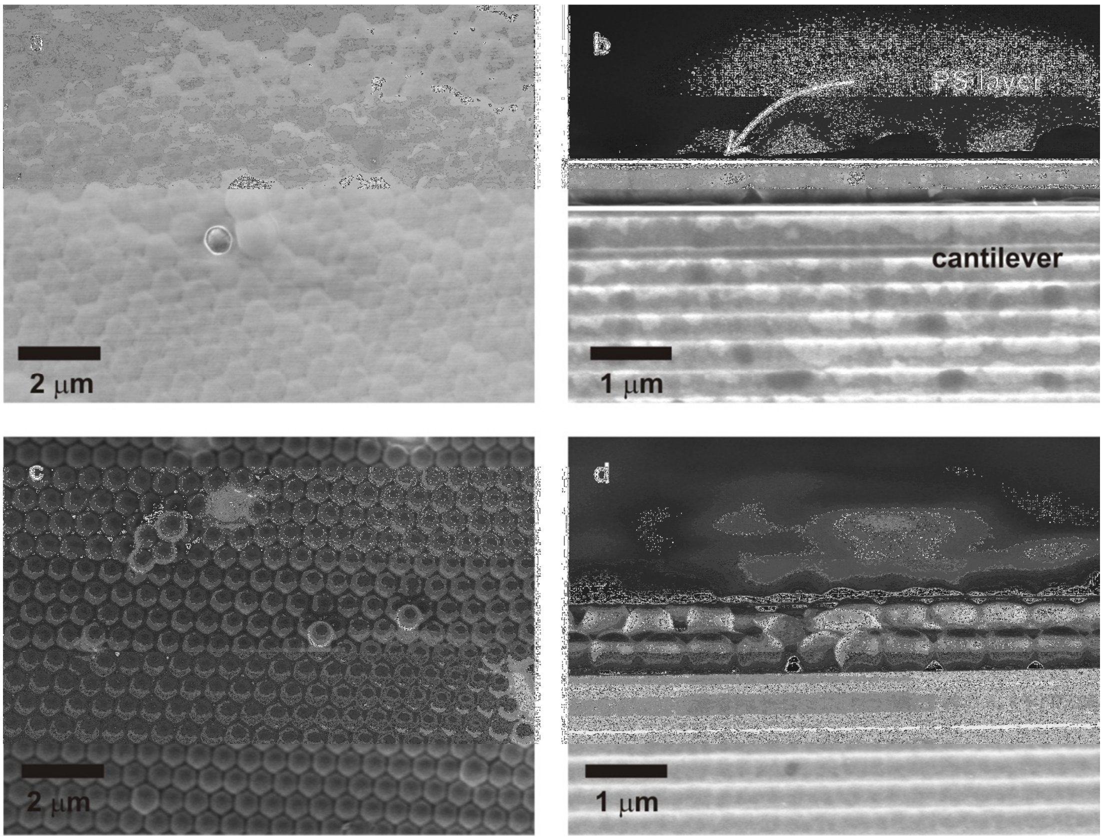

Figure 69: SEM images of the film formed from 1% crosslinked PS (a, b) and 10% crosslinked PS (c, d) colloidal monolayer after toluene solvent annealing.

The drying process of 1% crosslinked PS (Figure 68a, not striped regions) and 10% crosslinked PS (Figure 68b, not striped regions), resembles that of non crosslinked PS, the tensile stress in the film bends the cantilever towards the coating layer.

In general, crosslinked particles induces a stronger deflection (700 nm for 1% crosslinked colloids and 600 nm for 10% crosslinked colloids) of cantilever than the non crosslinked particles (400 nm), although the non crosslinked PS absorbed more toluene, since crosslinked polymers can transduce the stress in the polymer film better than the lower one due to their higher stiffness.[71]

In summary, during swelling a compressive stress between the polymer film and cantilever bends the cantilever away till the film becomes so soft that it cannot bend the cantilever any more. For glass transition of non crosslinked PS colloids, the polymer has to absorb about 10% toluene vapor; for transition of 1% crosslinked colloids, about 40% toluene of polymer weight is needed, but the softening process run faster, if often exposed to toluene vapor. The highly crosslinked particles does not become so soft as non crosslinked and slightly crosslinked particles at the same temperature. The magnitude of deflection is affected by the contact area between the coating film and cantilever, swelling in colloids induces smaller deflection than continuous film of the same material due to their confined contact cantilever. During drying process, tensile stress bends the cantilever to the coating layer.

6.2.3 Variation of Toluene Vapor Activity

For the above mentioned measurements, the activity of toluene is kept at 1. The stress development of non-, 1%- and 10% crosslinked colloidal monolayer is investigated. Another important factor which has an impact on the toluene uptake of PS [97, 101] and thus also on the stress evolution is the amount of available toluene in the vicinity of the PS film. In order to study the stress evolution of the colloidal polymer monolayer as function of the toluene concentration, the vapor pressure of toluene was varied during the deflection measurements of the cantilever.

PS colloids crosslinked with 1% DVB is chosen for the measurement, since the film formed from these colloids is close to the continuous film in *Young's* modulus, and the film formation is not too fast. The vapor activity is varied from 0.05 to 0.5, before each input of toluene vapor the sample cell is pumped with $N_2$to dry the samples. The exposure time is kept for 1 hour for both toluene and N_2 exposure.

The deflection is plotted against time (Figure 70) and the toluene activity of each toluene exposure is shown above the diagram. Similar to the deflection measured during constant toluene vapor pressure, the cantilever bends away from the coating layer during uptake of toluene (striped regions) and bends towards the coating layer during drying process (not striped regions).

The deflection of the cantilever shows that in the first three cycles the deflection has not reached the equilibrium in one hour and the deflection at the end of exposure increased with the vapor pressure. After these three cycles, the deflections of cantilever all have a magnitude of about 1200 nm. The evolution of the stress curves resembles that of the 10% crosslinked PS monolayer during toluene exposure with toluene activity at 1. Probably the movement of polymers is also limited in the colloids at lower concentration of toluene.

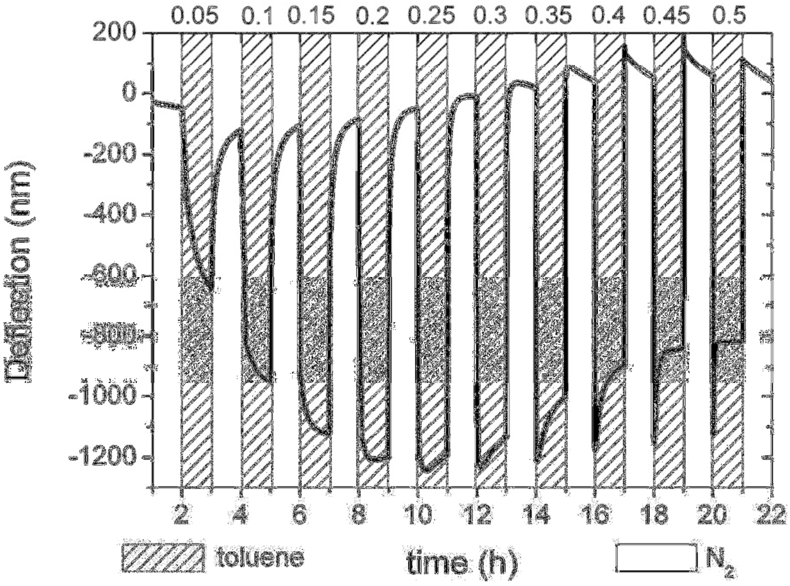

Figure 70: Deflection of a typical cantilever coated on one side with 1% crosslinked PS colloidal monolayer during exposure to toluene plotted against time (axis at the bottom) and vapor activity of toluene (axis at the top). The deflections are recorded after one hour exposure.

With vapor activity above 0.3, the cantilever starts to bend back to the coating layer after the deflection maximum is reached in each cycle. With increasing vapor pressure, the bending back process becomes faster. This effect very much resembles the observation for deflection measurements during exposure toluene vapor with activity at 1. The overshoots of the deflection curve imply a longer relaxation of polymer and also the diffusion of the polymer cross the colloid interfaces. However, the cantilever does not completely bend back to stress zero state, which means the stress was not completely released upon relaxation and plasticization of the film due to the smaller amount of available toluene.

As declared in last section, the overshoot of the cantilever is related to the glass transition of the PS coating layer and the time the cantilever needs to bend to equilibrium after the overshoot is defined as t_g. The overshoots occur after vapor activity reaches 0.3. However, at vapor activity 0.3 and 0.35, the deflection of the cantilever does not reach the equilibrium after the overshoot. As reported for PS brushes, the glass transition takes places with toluene activity at 0.4.[100] Therefore, I consider in my work the glass transition takes place also toluene activity at 0.4, where the equilibrium of the deflection was reached.

Comparing the film formed after exposure to toluene with vapor activity at 0.5 (Figure 71) to the film formed after exposure to toluene with vapor activity at 1, the former one is not so flat and part of the film break apart, probably during the drying process. Both effects indicate that in the former case the amount of the polymers, which undergo interface diffusion, is less than in the latter case.

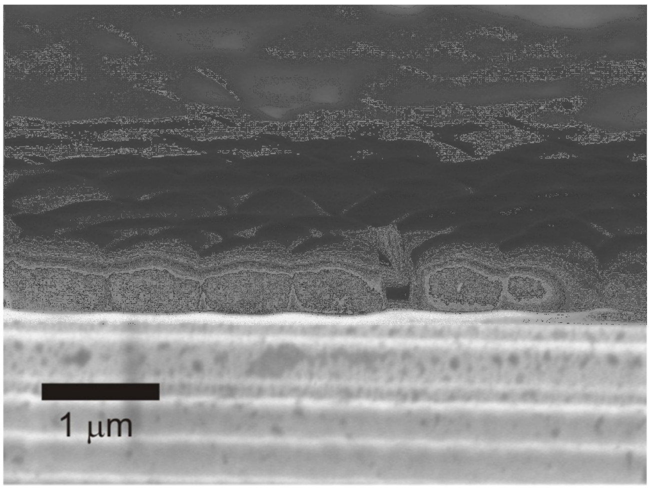

Figure 71: SEM image of the film formed 1% crosslinked colloidal monolayer after the toluene vapor annealing.

6.3 Summary

The monolayer coated on a cantilever can undergo film formation through thermal and organic vapor annealing. Hence an elegant method to coat cantilever with film with thickness of a few hundred nanometer has been realized.

By measuring the resonance frequency during the thermal annealing the film formation process could be monitored. During the film formation, the resonance frequency of the cantilever increases due to the elasticity contribution of the homogenous film. The film formation takes places after the glass transition starts. After the polymer changes from a glass state to a viscoelastic state, the resonance frequency decreases due to the softening of the polymer. After the cantilever and the coating film is cooled down to the ambient temperature, the resonance increases to a value, which is higher than the starting resonance frequency. This increase in resonance frequency can be used to estimate the *Young's* modulus of the film. For PS film with thickness of about 300 nm formed via thermal annealing, a *Young's* modulus of 2.7 GPa is obtained. This modulus is consistent with bulk PS. For a Ps film via toluene vapor annealing with similar thickness, a *Young's* modulus of 2.3 GPa is obtained. The lower *Young's* modulus is a consequence of the residual toluene in the PS film.

In the future, this method can be employed to study the variation of elastic modulus of polymer films during external stimuli: for instance UV light crosslinking and plasticizer.[102]

By applying the micromechanical cantilever to investigate crosslinked PS colloids and the resulting films, it is observed that the glass transition temperature increases with the crosslinking degree and *Young's* modulus of the resulting film decreases with crosslinking degree. Both effects can be explained by the restricted mobility of the polymer chains in the crosslinked colloids.

By measuring the deflection of the cantilever during the organic vapor annealing, the film formation can also be monitored. In addition, the stress evolution in the polymer film with during uptake of solvent molecule has been measured. The stress evolution is characteristic for each polymer colloids monolayer and the film they form. In principle, the sorption of toluene induces compressive stress and bends the cantilever away from coating layer. Relaxation and plasticization of the film reduce the stress and bend the cantilever towards the coating layer. All the three effects are dependent on the amount of available toluene.

Since all the three effects are also time dependent, it is challenging to analyze them separately, here simulation and theory has to be developed. The scientists tried to develop such theory often have had difficulties to compare the theory with experimental data, since the viscoelastic properties of the most of the suitable coating layers for cantilever (for instance plasma polymer) are unknown. In contrast, both the viscoelastic properties of PS and the interaction between toluene and PS have been elaborately investigated. Hence PS coating layers can be used as a model system to study the stress evolution of coating films of cantilever upon organic vapor absorption.

By combining the dynamic and static measurements of cantilever, the amount of toluene needed to induce glass transition of the different crosslinked PS can be estimated. As for the 1% crosslinked PS colloids, the toluene need to induce the glass transition is three times more for the non crosslinked colloids. Similar as during the glass transition induced by heating, the mobility of crosslinked polymers is more restricted than the non crosslinked polymers and therefore need more solvent to reach the glass transition.

7 Polymeric Functionalized Cantilevers as Glucose Detectors

For the application as sensor the cantilever has to be first coated with an active layer and the active layer should exhibit considerable affinity to the target molecules. Recently, scientist started to focus on coating of the cantilever with polymer brushes. Grafted polymer brushes have several advantages: I) grafted brushes cannot be washed away from the surface by solvent; II) they are cheap and convenient to synthesize; III) they induce larger deflection of the cantilever due to the relatively large conformational or volume change in the polymer chains; IV) functional moieties can be incorporated in the polymer brushes via copolymerization or subsequent chemical reaction, which multiplies the possibilities to detect more different target molecules. The sensing ability of cantilevers coated with polyelectrolyte brushes such as polyaniline (PAn),[103] polypyrrole (PPy)[104] and poly[2-(methacrylolyoxy)ethyl] trimethyl ammonium chloride (PMEAC) brushes[105] has already been tested.

Among the coating polymers, poly(N-isopropylacrylamide) (PNIPAAM) has great potential to serve as a sensing layer. PNIPAAM is a stimuli-responsive polymer and can change from water soluble to water insoluble. The polymer swells in aqueous solution in soluble state and collapses in insoluble state.[106] The transition of the polymer from soluble to insoluble state can be triggered by temperature variation of the system. PNIPAAM has a lower critical solution temperature (LCST) of approximately 32°C in aqueous solution. Below the LCST, the polymer is water soluble; above the LCST, the polymer is water insoluble. Additionally, the transition of PNIPAAM can also be triggered by adding co-solvents, or varying the pH or ionic strength of the solution.[107] Recently, synthesis of thin layer of PNIPAAM onto one side of the cantilever sensor has been demonstrated to be successful.[108]

The collapse of the polymer upon heating can be monitored by measuring the deflection of the coated cantilever and the LCST of PNIPAAM thin layer is close to that reported for the bulk material.[109]

In particular, during heating of the polymer from room temperature to LCST, the water molecules are released from the polymer films as it collapses. As a result, the cantilever bends towards the polymer film (Figure 72 a to b). During heating above the LCST, the cantilever bends away from the collapsed polymer film due to bimetal effect, i.e. the polymer expands stronger during heating than the cantilever (Figure 72c).

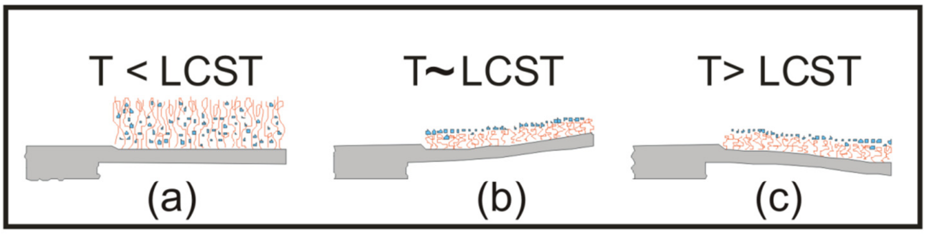

Figure 72: Illustration of the deflection of cantilever coated with PNIPAAM brushes as response to temperature. [109]

Conformational change of PNIPAAM can be reflected by the deflection of the cantilever. Is that possible to use this effect to detect target molecule? To answer this question, affinity of the coating layer and the target molecule has to be achieved first. This can be realized by incorporation of a compound, which has strong affinity of the target molecule, into the PNIPAAM brushes. A good candidate is phenylboronic acid (PBA), since it can bind glucose through reversible boronate ester formation (Figure 73) in aqueous media.[91b, 110] PBA can also be incorporated into PNIPAAM brushes via radical polymerization.[111] Different polymers incorporated with PBA have often been employed to detect glucose.[112] The binding of glucose to PBA increases the mass and volume of the polymer. Therefore the binding can be transduced to a physical signal by means of weighing with quartz microbalance[113] or by means of volume detection with light diffraction.[112a]

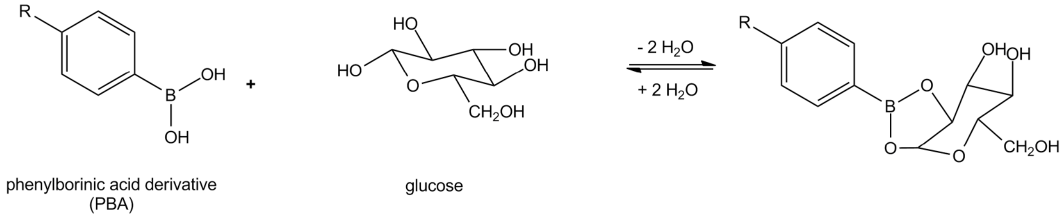

Figure 73: Scheme of reversible binding between PBA and glucose.

In this work, PNIPAAM brushes incorporated with PBA is used to functionalize cantilever and serves as a model system to demonstrate sensing ability of polymer coated cantilever by means of glucose detection. In addition, the signal amplifying effect of the polymer brushes compared to the self-assembled monolayers (SAM) has been investigated. Most of the SAM coating are based on the gold-thiol chemistry. The cantilever is first deposited with a thin layer of gold. Alkanethiols, thiolated nucleic acid and proteins can self-assemble to a monolayer on the gold film due to the strong affinity of thiols to gold.

The PBA moieties exhibit the function to bind glucose, while the PNIPAAM-PAA copolymer can tune the amplitude of the cantilever deflection via varying temperature, pH, and ionic strength of the environment. Using a cantilever, the bending due to glucose on one side of the cantilever induces a surface stress change and thus can be detected by measuring the deflection of the cantilever.

In particular, eight cantilevers on one array were divided into four groups and functionalized with gold, self-assembled monolayer of 4-Mercaptophenylboronic acid (MPBA-SAM), PNIPAAM-co-PAA brushes and PNIPAAM-co-PAA-PBA brushes, respectively (Figure 74).

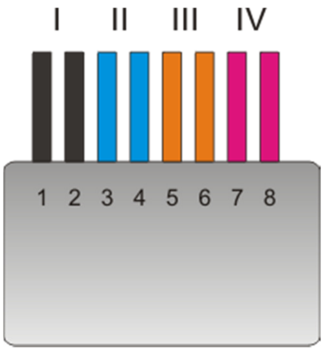

Figure 74: Schematic topside view of the micromechanical cantilever array. Cantilevers of the first group are coated with gold (I), of the second group (II) with MPBA-SAM, of the third group (III) with PNIPAAM-co-PAA, and of the fourth group (IV) with PNIPAAM-co-PAA-PBA.

The surface stress response of the functionalized cantilevers to glucose in phosphate buffered saline (PBS) solution is recorded. Comparing the deflection of cantilever group I with II and III with IV, the specific binding of glucose to PBA can be evaluated; comparing group II and IV it is possible to assess the effect of the polymer brushes on the amplitude of deflection. In addition, the stimulus-response of these polymer brushes to variation in glucose concentration and pH of the solution is evaluated by measuring concomitant brush height changes by SFM.

7.1 Mass of Coating Layer

In order to obtain the mass of PNIPAAM coated on the cantilever, the resonance frequency of blank cantilever and functionalized cantilever is measured. The mass of the coating layer on cantilever was calculated with equation (2.16) and the results are shown in Table 3.

All the cantilevers are first coated with a 45 nm thick gold layer, which has a mass of about 37 pg. The weight of the MPBA monolayer is negligible compared to the weight of the gold layer. In contrast, the polymer brushes PNIPAAM-co-PAA and PNIPAAM-co-PAA-PBA with the gold layer has a mass of 56 pg and 70 pg, respectively, meaning there are about 20 pg PNIPAAM-co-PAA and 33 pg and PNIPAAM-co-PAA-PBA coated on the cantilever.

Table 3: Mass *m* of different coating layers on cantilever obtained by resonance frequency measurement.

	m / pg
gold	37±2
MPBA-SAM on gold	37±2
PNIPAAM-co-PAA on gold	57±8
PNIPAAM-co-PAA-PBA on gold	70±9

7.2 Topological Analysis

Topological analysis of both side of the cantilever is carried out first to check if the asymmetrical coating was successful, second to estimate surface change of cantilever upon coating with polymer brushes (Figure 75). The coated sides of cantilever (Figure 75 a) reveal spots and islands on the surfaces, in contrast the uncoated sides show smooth surfaces (Figure 75 b).

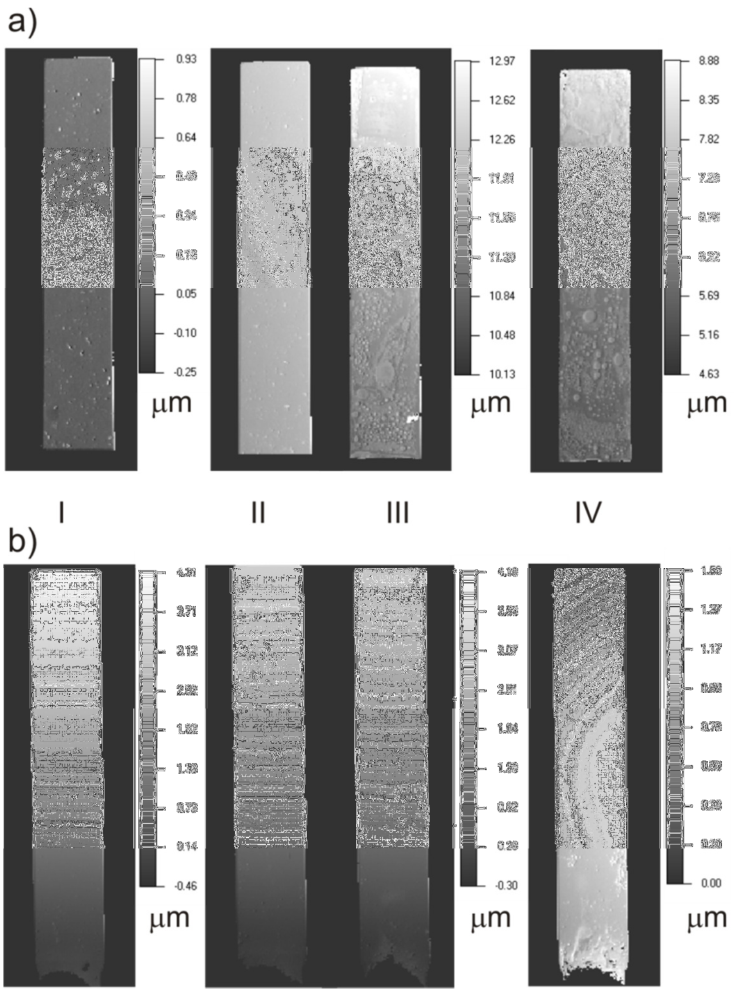

Figure 75: Topological images of cantilevers: a) coated sides; b) uncoated sides. The cantilever was coated with gold (I), with MPBA-SAM (II); with PNIPAAM-co-PAA (III); and with PNIPAAM-co-PAA-PBA (IV).

According to the roughness analysis (Table 4), the uncoated side has a similar roughness to the side coated with gold (group I) and the monolayer of MPBA (group II). Upon coating with polymer brushes, the roughness of the cantilever surfaces increased dramatically, which can be attributed to the islands formation on the surface.

Table 4: Averaged root mean square roughness obtained by profiles of cantilever functionalized with different coating layers.

	Coated side	Uncoated side
	roughness/nm	roughness/nm
Gold (I)	47 ± 13.5	42 ± 2.1
MPBA-SAM (II)	49 ± 4.6	39 ± 6.5
PNIPAAM-co-PAA (III)	192 ± 24.8	44 ± 9.2
PNIPAAM-co-PAA-PBA (IV)	211 ± 9.7	65 ± 22.3

7.3 Surface Stress Change upon Glucose Binding

To study effects of glucose binding on the bending response of micromechanical cantilevers, the deflection of functionalized cantilever array is measured. Once mounted into a flow cell, deflection measurements are started immediately after injection of PBS buffer solution. A 50 mM solution of glucose in PBS buffer is injected once the cantilevers reached an equilibrium deflection in PBS. Measurements are carried out at two different pH values. The averaged deflection response of the cantilevers in response to the solvent conditions (PBS buffer and 50 mM glucose in PBS) at two different pH conditions is plotted as a function of time (Figure 76).

The approximate differential surface stress between the top and underside side of the micromechanical cantilever σ was calculated using Stoney's formula introduced in chapter 2 (equation (2.19)).

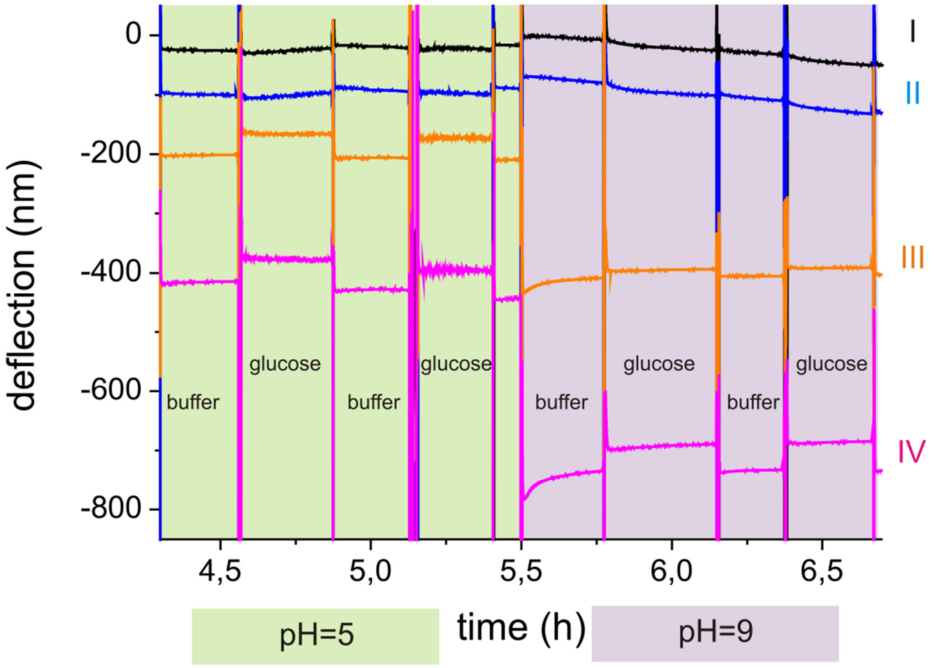

Figure 76: Average deflection response of the micromechanical cantilevers as schematically shown in Figure 5 at different solution conditions and at two pH values.

First the effect of pH on cantilever deflection in absence of glucose is considered. Changing the pH from 5 to 9, the deflection response of cantilevers coated with gold (Group I) and the MPBA-SAM (Group II) changes little, 11 nm and < 1 nm, respectively. However, the cantilevers coated with PNIPAAM-co-PAA (Group III) and PNIPAAM-co-PAA-PBA (Group IV) bend away from the polymer brushes by 208 nm and 280 nm. The corresponding surface stress changes are calculated to be 1.26 N/m and 1.69 N/m, respectively. At pH 9 both PAA and PBA are ionized and the repulsive interaction of charges caused by the increase of the ion concentration in the polymer chains leads to an increase in swelling.[114]

Next the effect of exposure to 50 mM glucose on the cantilever bending response at both pH values is studied. The cantilevers coated with PNIPAAM-co-PAA (Group III) and PNIPAAM-co-PAA-PBA (Group IV) bend towards the polymer brushes upon injecting glucose solution in the cell. As seen in Figure 76, the cantilever bending response is reversible upon sequentially changing the solvent conditions from PBS buffer to 50 mM glucose in PBS at both pH values. To obtain geometry independent data, the surface stress change of the cantilevers is calculated by using equation (2.19) and the results are shown in Figure 77**.** At pH 5, the surface stress change of the cantilevers coated with gold (Group I) and MPBA-SAM (Group II) was small, indicating no significant glucose adsorption. The cantilevers coated with PNIPAAM-co-PAA (Group III) and with PNIPAAM-co-PAA-PBA (Group IV) bent towards the polymer brushes during exposure to glucose, with a surface stress decrease of about 0.20 N/m. Since both cantilevers responded about equally, there is no obvious evidence of specific binding of glucose to PNIPAAM-co-PAA-PBA at pH 5.

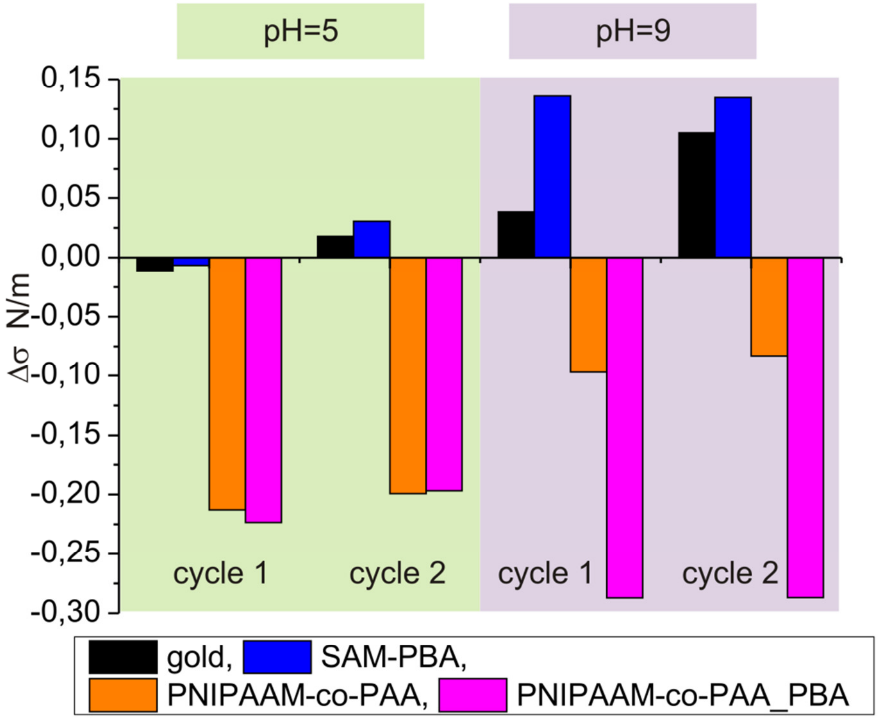

Figure 77: Surface stress response upon exposure to 50 mM glucose in PBS at pH=5 and pH=9. Black column (Group I): cantilevers coated with gold; blue column (Group II): cantilevers coated with PBA-SAM; red column (Group III): cantilevers coated with PNIPAAM-co-PAA; pink column (Group IV): cantilevers coated with PNIPAAM-co-PAA-PBA.

At pH 9, the cantilevers coated with gold (Group I) and MPBA-SAM (Group II) bend away from the coated side with a concomitant surface stress change of 0.075 N/m and 0.14 N/m, respectively. The cantilevers coated with PNIPAAM-co-

PAA (Group III) and with PNIPAAM-co-PAA-PBA (Group IV) again bend towards the coating layer, but the surface stress decreases by 0.09 N/m and by 0.27 N/m, respectively. The apparent bending difference and the concomitant change of surface stress between these two cantilevers indicate a specific binding of glucose to PNIPAAM-co-PAA-PBA. Furthermore, reading from Figure 77 the magnitude of the surface stress change of the PNIPAAM-co-PAA-PBA coated cantilevers is about twice as large as that of cantilevers coated with MPBA-SAM.

7.4 Height Response of Polymer Brushes to Glucose

Contact mode SFM images are recorded at Duke University to investigate the height variation of PNIPAAM-co-PAA-PBA brushes as response to glucose binding. At pH 9 (Figure 78A, B) the height increase during exposure to 50 mM glucose in PBS solution indicates binding of glucose to the PNIPAAM-co-PAA-PBA brushes in PBS buffer. As shown in the profile (Figure 78) the height of the polymer brushes increased by approximately 150 nm after the injection of PBS with glucose. Soluble glucose binds to the tetrahedral, ionized boronate species within the brush and causes the observed additional swelling response.[112e, 115] The swelling of the polymer brushes induced by the complexation of glucose has two causes: i) the incorporation of a hydrophilic molecule, and ii) the increase in negative charge within the brushes, which increases Coulombic repulsive interactions and osmotic pressure due to the increase in counter ion concentration within the brushes. These results confirm PBA’s ability to complex glucose and as a result, the conformation of PNIPAAM-co-PAA-PBA brushes changes.

To demonstrate the specific binding between PBA and glucose, the height of PNIPAAM-co-PAA brushes is also measured by SFM during exposure to air, pure PBS solution and to glucose solution in PBS buffer (Figure 78C). The height of PNIPAAM-co-PAA brushes increase from 150 nm to 420 nm as the environment of the brushes changes from air to PBS buffer, indicates that the polymer change from a collapsed state in air to a swollen state in an aqueous environment. The PBS buffer with glucose is injected into the sample cell after the pure PBS buffer and there is no height variation of PNIPAAM-co-PAA observed, which indicates that without PBA moieties incorporated in PNIPAAM-co-PAA brushes, the copolymer brushes do not change in height or conformation with exposure to glucose.

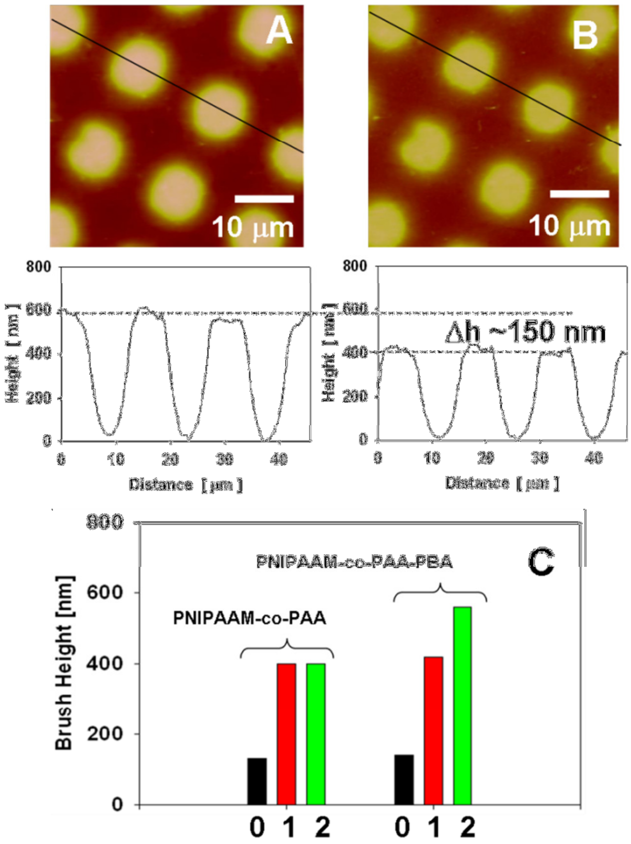

Figure 78: Contact mode SFM height images of PNIPAAM-co-PAA-PBA brushes at room temperature in PBS buffer solution (A) with 50 mM glucose (B) without glucose) at pH 9. **(C)** Brush height of PNIPAAM-co-PAA and PNIPAAM-co-PAA-PBA in different conditions (0: in air, 1: in PBS buffer at pH 9.0, and 2: in PBS buffer at pH 9.0 with 50mM glucose).

7.5 Summary

Micromechanical cantilevers have been functionalized with glucose-responsive PNIPAAM-co-PAA-PBA brushes and their potential as glucose sensors has been evaluated. Glucose-responsive PNIPAAM-co-PAA-PBA brushes show a large, reversible swelling response in the presence of free glucose in aqueous solution. According to SFM height measurement at pH=9, the polymer brushes increase in height during the exposure to glucose solution.

The study of the deflection and the surface stress response of cantilevers functionalized with PNIPAAM-co-PAA-PBA brushes is more complex than the study of the height of polymer brushes alone. On one hand, at pH=9, cantilevers functionalized with PNIPAAM-co-PAA-PBA brushes show specific binding to glucose in solution and have larger response to glucose than MPBA-SAM functionalized cantilevers. This shows the potential of PNIPAAM-co-PAA-PBA brushes for micromechanical cantilever glucose sensing applications, and demonstrates more generally the possibility of responsive polymer brushes to sense and transduce changes into deflection of cantilever in a solution environment efficiently. On the other hand, at pH=5,based on the deflection of cantilever, there is no specific binding of glucose to PNIPAAM-co-PAA brushes observed, although according to the SFM results the height of the brushes increases during exposure to glucose.

8 Experimental

8.1 FCS Investigation of Shape of DNA Hybrid Aggregates

8.1.1 Materials

The ssDNA-PDI molecules used in this work are synthesized by Milena Anaya in Professor Klaus Müllen’s group via a “syringe synthesis technique”.[116] The ssDNA conjugated with PDI is chosen as a 22mer and has the following sequence: 5’-CCTCGCTCTGCTAATCCTGTTA-3’ with molecular a weight M_w of 6612g/mol. The template ssDNA is a 88mer (5’-(TAACAGGATTAGCAGAGCGAG)$_4$-3’), which consists of four complementary units to ssDNA-PDI. The ratio of the ssDNA-PDI and template ssDNA is adjusted to 4:1, allowing complete hybridization. The dsDNA helix twists 360° per 10.6 base pairs,[117] which means that the 22 base pairs complete 2 turns. Both the ssDNA22mer and the ssDNA88mer are purchased from the company Sigma-Aldrich and measured without any further treatment.

8.1.2 Hybridization of ssDNA

The hybridization procedure of ssDNA to dsDNAs are all carried out in a Tris buffer (20 mMtris(hydroxymethyl)aminomethane-HCl, pH 7.4; 10 mM acetic acid, 0.5 mMEthylenediaminetetraacetic acid) containing Na^+ (100 mM) and Mg^{2+} (60 mM). The mixture of ssDNAs is heated to 95°C and then slowly cooled to room temperature over 3 days (1 degree per hour) by using a thermocycler (Biometra GmbH, Germany). The final concentration of dsDNA is around 2 µM.

8.1.3 FCS Measurements

A commercial FCS setup manufactured by Carl Zeiss (Jena, Germany) consisting of the module ConfoCor 2 and an inverted microscope, model Axiovert 200 is used. About 300 µL solution of the sample is placed in an eight-well, polystyrene chambered cover-glass (Lab-Tek, NalgeNunc International, Rochester, USA).The chambered cover glass is then placed above a water immersion objective (UPlanSapo 40xW, 1.2 n.a., Olympus, Hamburg). Alexa488 labeled samples are excited by an Argon laser (Spectra Physics) at 488 nm and the Fluorescence emission was collected after filtering with bandpass BP505-550 nm. PDI labeled samples were excited at 543 nm by a HeNe laser(Spectra Physics) and the fluorescence signal is collected after filtering with long pass long-pass LP560 nm.A diluted Rhodamine-110 (diffusion coefficient: 2.8 $\mu m^2/s$[118]) solution in pure water was used as the reference to yield the optical parameters of the confocal detection volume. For each solution a series of 10 measurements with total duration of 5 minutes is performed.

8.2 FCCS Investigation of the Residence Time of Unimers

Solutions containing 10 µM dsDNA22mer-*b*-PPO labeled with Alexa488 and Alexa633 are obtained from Deepak K. Prusty in Professor Andreas Hermann's group in Groningen, Netherland. The molecular weight M_w of PPO is about 6800 g/mol and the dsDNAs own 22 base pairs. The solutions with Alexa488 and Alexa633 labelled dsDNA-*b*-PPO at concentration of 10 µM mixed in ratio of 1:1 at 37°C for 2 days to give a mixture A. Solution containing not labelled dsDNA-*b*-PPO at concentration of 30 µM is then added to mixture A with a volume ratio of 10:1 to give a mixture B. The mixture B is diluted with water by 100 fold to achieve a proper fluorescent intensity for FCCS measurement.

The FCCS is performed on the same setup as described for FCS. To excite Alexa488 and Alexa633 labeled samples, two collinear laser beams of wavelength 488 nm (Argon laser) and 633 nm (HeNe laser) are coupled to generate two superimposed focal spots of excitation laser light in the sample. The fluorescence light emitted by the samples is led through a 50 µm pinhole to block the out-of-focus fluorescence.

Behind the pinhole the light emitted by the two samples are spitted by a dichroic mirror. Residual laser excitation light and Ramen scattered light of water molecules are removed by bandpass filter BP505-550 nm and longpass filter LP 650, respectively. At the end, the two emission signals are focused on two photodiodes operated in the photon counting mode. The cross-correlation of the output signals is calculated by a two-channel correlation in a PC board (ALV 5000^{M}, ALV).

Diluted aqueous solution of Rhodamine-6G and Atto 647 (both with diffusion coefficient: 2.8 $\mu m^2/s$[118-119]) are used as the reference to yield the optical parameters of the confocal observation volume at wavelength of 488nm and 633 nm, respectively.

8.3 Coating Cantilever with Colloids

8.3.1 PS Particles

All the PS colloids are synthesized in house via surfactant free emulsion polymerization.[120] The colloids are charge stabilized with acrylic acid. The non crosslinked PS colloids are solved in tetrahydrofuran and characterized by Gel Permeation Chromatography (GPC). The molecular weight M_n was 20 038 g/mol and the polydispersity of 5.2.For the crosslinked PS colloids, DVB is added in the reaction in ratio of 1wt% and 10wt% to styrene to produce 1% and 10% crosslinked PS colloids.[121]

8.3.2 Plasma Treatment of Colloids

The etching of PS colloids is carried out in commercially available plasma cleaner (Model femto, Diener electronic, Nagold, Germany). After placing the cantilever array coated with PS colloidal monolayer into the plasma chamber, the chamber is evacuated and flushed with the 5 sccmO_2 for three consecutive cycles. The temperature of the bottom plate of the plasma chamber is controlled by a cryostat with a water/ethylene glycol mixture. The power of the plasma oven is set at 50 watt. The etching duration can be varied by an internal time switch.

8.4 Study of Film Formation of Colloidal Monolayer by Cantilever

8.4.1 Micromechanical Cantilever Sensors

Custom made silicon micromechanical cantilever sensor arrays are obtained from Mcriomotive GmbH (Octosensis®). Cantilever with two different lengths 500 nm and 750 nm were purchased. The thickness of the cantilever varies from 1 µm to 5 µm.

8.4.2 Deflection Measurement

The deflection of cantilever is measured by Scentris (Veeco, Santa Barbara, CA) -a multiplexed beam deflection setup at 23°C simultaneously during the exposure to toluene vapor. The cantilever is mounted on a piezo actuator and fixed with a clip in a fluid cell, which is made of steel and the cell is sealed with a quartz slice. The fluid cell possesses an input and an output. The input is connected with a mass flow controller via a Teflon tube for access of N_2 and toluene vapor; the output is connected to another mass flow controller via another Teflon tube, and this line is ended with a pump. Thus it is feasible to draw the gas in controlled rate through the fluid cell. The light from super-luminescent diodes (SLD) is focused on the free end of the cantilevers; the reflected light is collected by a PSD.

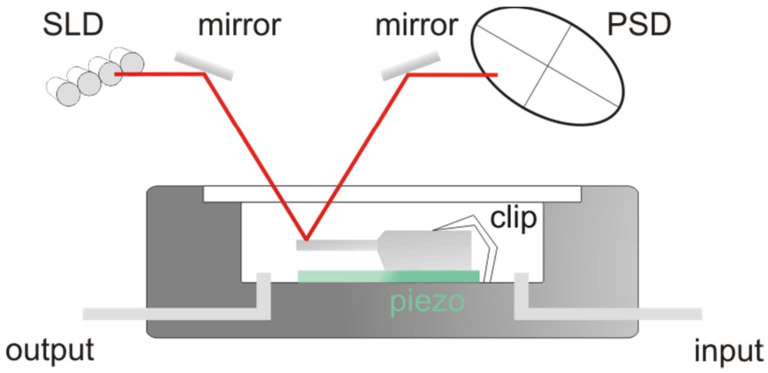

Figure 79: Illustration of the working principle of a multiplexed beam deflection setup (Scentris).

For the measurement in static mode, the cantilevers are asymmetrically coated as introduced in section 5.1. The colloidal monolayers are all deposited on the upper side of the cantilever (Figure 80, red line). Here, the recorded deflection goes to negative when the cantilever bends downwards, and the deflection goes to positive direction when the cantilever bends upwards (Figure 80). The deflection measured here is all relative to the start position of the cantilevers, which is denoted as zero deflection.

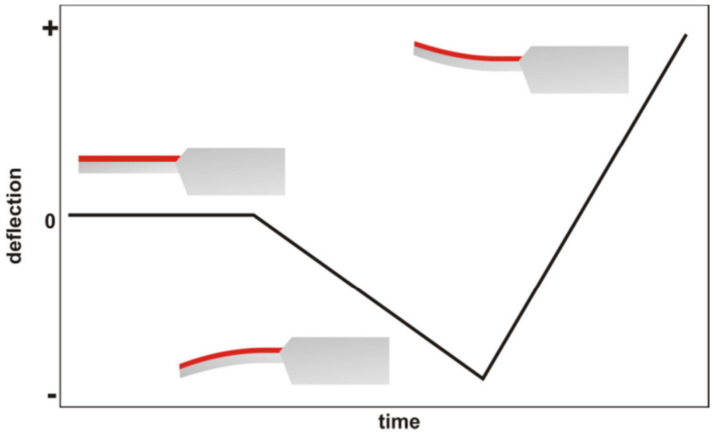

Figure 80: Illustration of the cantilever coated with a colloidal monolayer (red line) on the upper side and recorded deflection signal and the corresponding bending direction of cantilever.

8.4.3 Resonance Frequency Measurement

The resonance frequency of the cantilever is measured with an EnviroScope SFM (Veeco Instrument, Plainview New York). All the measurements in dynamic mode are carried out in a vacuum chamber at 2 mbar to avoid noise during heating. The cantilever mounted on a piezo-driven cantilever holder in the EnviroScope SFM chamber. The temperature is adjusted by the sample holder in SFM with integrated LakeShore 331 Temperature Controller (LakeShore, Westerville, USA) from room temperature (~25 °C) to 210 °C with the heating/cooling rate set as high, which is about 5°C/ min. The cantilever is placed about 2-3 mm above the sample holder and thus a temperature decline of about 5°C from the sample holder to cantilever could arise.

8.4.4 Mass Flow Controller

The house built mass flow controller setup is illustrated in Figure 81. The setup consists of two main gas lines. Gas line A is filled only with pure N_2 (99.9997%). Gas line B is used to generate toluene vapor and is split into gas line B1 and B2. Gas line B1 is also only filled with pure N_2. In gas line B2, N_2 flows through a container filled toluene (99.97% Fischer Scientific, UK) as a carrier gas. The temperature of toluene is maintained at 30 °C. Thus the N_2 in gas line B2 is saturated with toluene vapor. To avoid vapor pressure fluctuation of the toluene upon condensation on the tube wall or sample cell at room temperature (22-24 °C), the gas flows through a compensating flask cooled to 20 °C. Thus, the outgoing gas in line B2 is not saturated at room temperature and has a constant vapor pressure. Each gas line is connected with a mass flow controller (McMillan Company, Georgetown, USA) to control the flow rate of the gas. By varying the flow rate of line B1 and B2, the vapor pressure of toluene vapor can be adjusted.

Since the measurement of deflection and resonance frequency of cantilever is very sensible to the gas flow in the fluid cell, it is important to keep the flow constant during changing the gas composition in the sample cell. Therefore a switch is used to connect line A and B with the output 1 and 2. The output 2 is connected to the fluid cell, where the cantilever is mounted. Using the switch, the output 2 can be connected to line A first and switched to line B within one second. Thus it is possible to change the gas flowing into the fluid cell from pure N_2 to toluene vapor within a second. With both lines A and B adjusted at the same final flow rate, the gas composition can be changed with negligible influence on the measurement of the cantilever.

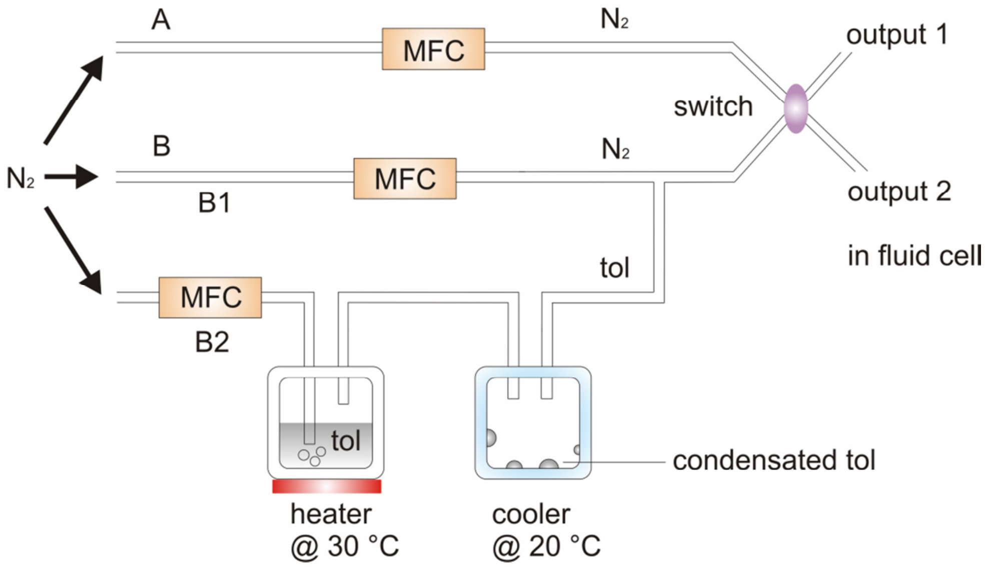

Figure 81: Sketch of the mass flow controller. Tol is an abbreviation for toluene.

The mass flow control setup can be operated with a LabView™ program. It is possible to set the flow rate of each gas line and to switch gas line to output 2 at given time and with given duration (Figure 82). The columns to set different parameters are denoted.

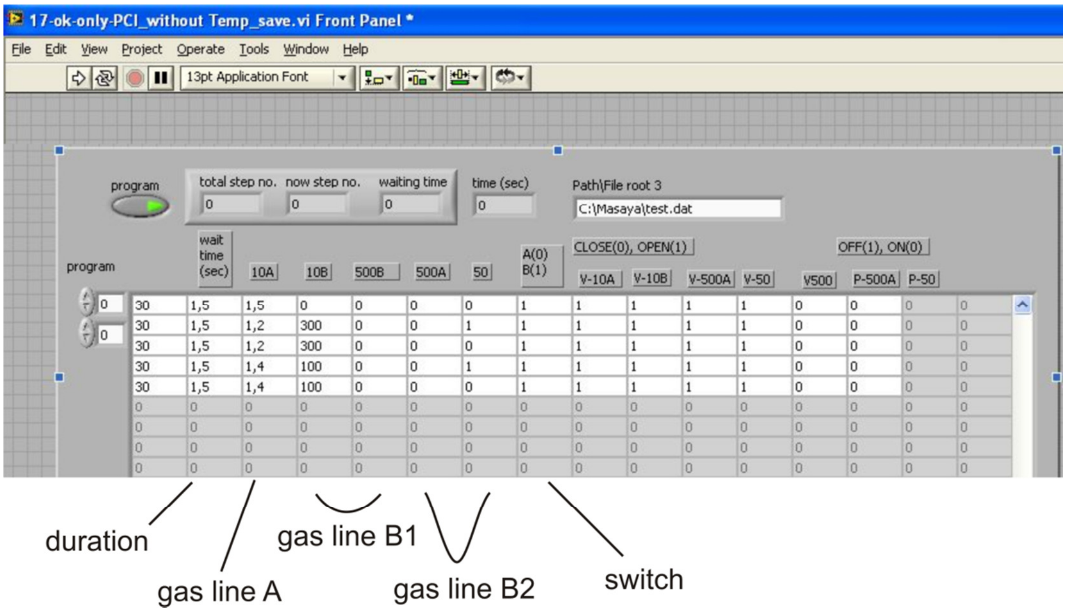

total step no. 0
now step no. 0
waiting time 0
time (sec) 0
Path\File root 3 C:\Masaya\test.dat
program 0 0

								CLOSE(0), OPEN(1)				OFF(1), ON(0)			
	wait time (sec)	10A	10B	500B	500A	50	A(0) B(1)	V-10A	V-10B	V-500A	V-50	V500	P-500A	P-50	
30	1,5	1,5	0	0	0	0	1	1	1	1	1	0	0	0	0
30	1,5	1,2	300	0	0	1	1	1	1	1	1	0	0	0	0
30	1,5	1,2	300	0	0	0	1	1	1	1	1	0	0	0	0
30	1,5	1,4	100	0	0	1	1	1	1	1	1	0	0	0	0
30	1,5	1,4	100	0	0	0	1	1	1	1	1	0	0	0	0
0	0	0	0	0	0	0	0	0	0	0	0	0	0	0	0
0	0	0	0	0	0	0	0	0	0	0	0	0	0	0	0
0	0	0	0	0	0	0	0	0	0	0	0	0	0	0	0
0	0	0	0	0	0	0	0	0	0	0	0	0	0	0	0

Figure 82: Screenshot of the LabView™ operation panel.

The fluid cell, in which the cantilever is mounted, has a volume of 30 μL and the flow of toluene vapor is set at 0.5 cm^3/min. That means theoretically in a few seconds the vapor can fill the fluid cell and the connecting Teflon tubes.

8.4.5 Dynamic Mechanical Analysis

The Dynamic Mechanical Analysis of the PS particles was carried out by a rheometer (ARES, Rheometric Scientific, Piscataway, USA). About 30 mg of the non crosslinked PS particles were dried at 60°C in vacuum for overnight. The PS particles were then pressed in to a pellet with diameter of 6 mm and thickness of 1 mm. The pellet was placed in the rheometer between two parallel plates with distance of 1 mm. To achieve good contact between the pellet and the plates, the pellet was heat to about 200°C first. The sample was measured in a controlled strain process, where the strain of the sample was kept constant and the sinusoidal stress applied to the sample to achieve this strain was measured. The measurement was carried our during the cooling from 190°C to 100°C in frequency from 0.1 rad/s to 100 rad/s. Since the stress was applied sinusoidally, the phase shift between the stress and strain can be analyzed. The storage modulus G’ expresses the in-phase component and the loss modulus G’’ expresses the out of plane component. According to Williams-Landel-Ferry (WLF) model, time and temperature can be mathematically interchanged under certain circumstances, and hence it is possible to predict the G’ and G’’ from collected data at a range of temperature and frequency, which are not directly measurable.

8.5 Glucose Detection by Polymeric Functionalized Cantilever

8.5.1 Polymer Brush Synthesis

The polymer synthesis of glucose-responsive poly(N-isopropylacrylamide)-co-poly(acrylic acid)-(3-aminophenyl-boronic acid) (PNIPAAM-co-PAA-PBA) brushes was carried out by Dr. Tao Chen in Duke University. The synthesis is already published.[122]

8.5.2 Cantilever Arrangement

The cantilever arrays used in these experiments have thickness of 5 µm, length of 500 µm and width of 90 µm (Octosensis®). The eight cantilevers on the cantilever array are divided into four groups (two adjacent levers in each group) and each group had a different coating on the cantilever top surface (Figure 74). For the analysis, the deflection of the two cantilevers in any one group is averaged. All cantilevers are first coated with a 50 nm gold film. Levers in Group I are not further treated; levers in Group II are coated with SAM of Methylphenylboronic acid (MPBA-SAM) with a micropipette manipulation system (Signatone, Gilory, CA) while monitoring with an optical microscope. Levers in Group III are coated with PNIPAAM-co-PAA, which is an intermediate product in the synthesis of PNIPAAM-co-PAA-PBA.

8.5.3 Resonance Frequency Measurement of Cantilever

The mass loading of the cantilevers can be estimated by measuring the resonance frequency shift. The frequency measurements are carried out for the cantilever using Scentris^{TM} (Veeco, USA) before and after coating.

8.5.4 Confocal Profilometer

Topological microscope analysis was performed by a µ Surf white light confocal profilometer (Nanofocus AG, Germany) with an Olympus UMPLFL 20× objective.

8.5.5 Scanning Force Microscopy

The SFM measurements were all carried out at Duke University. The SFM images are performed in contact mode using V-shaped silicon nitride cantilevers (Nanoprobe, Veeco, spring constant 0.12 N/m; tip radius 20-60 nm) using a Multi Mode atomic force microscope (Digital Instruments, Santa Barbara, CA). SFM images (40 µm ×

40 µm) of polymer brushes in air, in PBS solution with and without glucose (50 mM) are recorded.

8.5.6 Deflection Measurement of Cantilever

The functionalized cantilever array is mounted in a fluid cell. The pure PBS buffer and glucose solution in PBS buffer in different concentrations and pH values are filled in different beakers. The input tube is placed in the beaker with needed solution and the solution is drawn through the fluid cell with a syringe at the end of the circuit.

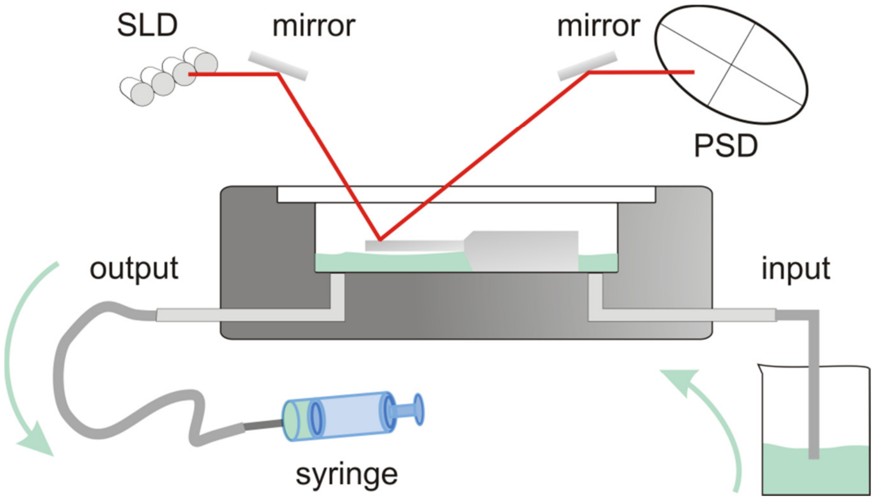

Figure 83: Sketch of the fluid cell to illustrate the solution input and output for glucose detection.

9 Summary and Conclusion

In this thesis, I have characterized different soft materials. The size and the shape of aggregates of amphiphilic DNA hybrid molecules and their residence time in micelles were investigated by means of Fluorescence Correlation Spectroscopy (FCS) and Fluorescence Cross-Correlation Spectroscopy (FCCS). I also studied the mechanical properties of polystyrene (PS) colloidal monolayers and homogenous films generated from such monolayers using micromechanical cantilevers. Finally, I tested whether polymeric functionalized micromechanical cantilevers could be used as sensors to detect small amounts of glucose in aqueous solution.

9.1 Aggregation Analysis by FCS

An aqueous solution containing DNA dye conjugate dsDNA-4PDI has been investigated by FCS. As visualized by SFM, two dsDNA-4PDIs can aggregate to dimmers with rod-like structures on a mica surface. An advantage of FCS as compared to SFM is that the measurements are carried out in an application relevant environment, e.g. in solution. Here, the existence of dsDNA-4PDI dimers could not be verified by FCS (chapter 3). Since the diffusion coefficient (according to equation (2.9)) of dsDNA-4PDI (38 $\mu m^2/s$) and the dimeric aggregates (27 $\mu m^2/s$) are considerably close to each other, distinguishing between both components during analysis of the autocorrelation curve obtained by FCS is difficult. In addition, the chance of the dsDNA88mer-4PDIs to meet each other is low in the solution. Aggregate formation of dsDNA-4PDI on a surface does not guarantee aggregate formation in the solution. This fact indicates that a substrate surface has an impact on the self-assembly of soft matter. When the application of these soft materials is in solution, a direct characterization in solution, for instance by FCS, is necessary.

A system containing two or more components with similar diffusion coefficients is challenging for the data analysis. The FCS investigation of dsDNA-*b*-PPO micelles also encountered such problems.[7b] Here, the spherical micelles were supposed to have a hydrodynamic radius of about 5.5 nm, which seems unlikely because it corresponds to only half of the length of a single dsDNA-*b*-PPO (11 nm) molecule with rod-like structure. The components detected by FCS were probably not the dsDNA-*b*-PPO micelles, but the single dsDNA-*b*-PPO molecules present in the solution containing micelles.

In order to study dsDNA-*b*-PPO micelles directly, FCCS was utilized (chapter 4). FCCS only measures components which are labeled with two different dyes. For this purpose, dsDNA-*b*-PPOs, labeled with either Alexa488 or Alexa633, have been used and micelles containing both dyes have been generated. Using FCCS, the existence of dsDNA-*b*-PPO micelles with a hydrodynamic radius of 11 nm could be confirmed. This radius corresponds to the length of single dsDNA-*b*-PPO molecules and is thus considered as more reasonable than the hydrodynamic radius obtained by FCS. To study systems including more components, FCCS should be preferentially considered.

As reported, the dsDNA-*b*-PPO micelle shape can be tailored by template ssDNAs (Figure 3). Using dsDNA-*b*-PPO as model molecules, micelles with dimeric structures could be investigated by FCCS. When this investigation is successful, the dimeric aggregates of DNA-PDI could also be further investigated by FCCS.

9.2 Mechanical Analysis of Polymer Films by Cantilever

I have demonstrated an elegant method for the deposition of homogenous polymer films onto micromechanical cantilevers by using colloidal monolayers as preliminary coating layers. Film formation from such colloidal monolayer can be induced either by thermal annealing and or by organic vapor annealing.

By operating the cantilever in dynamic mode, the film formation via thermal annealing can be monitored. According to the resonance frequency versus temperature diagram, the temperature at which the film formation starts can be detected. After thermal annealing, the resonance frequency of the cantilever increased although the loaded mass did not change during the transition of the colloidal monolayer into a homogenous film. The resonance frequency increase was induced by the elastic contribution of the homogenous film to the spring constant of the cantilever and can therefore be used to estimate the *Young's* modulus of the film. For a PS homogenous film with a thickness of about 300 nm generated from non crosslinked colloids, the *Young's* modulus is consistent with bulk PS. Hence, the micromechanical cantilever has been qualified as a convenient tool to characterize the mechanical properties of homogenous polymer films.

The mechanical properties of films formed from colloids with different crosslinking degrees have also been estimated by the resonance frequency shift of cantilever. The *Young's* modulus of the polymer film decreases with increasing crosslinking degree. The polymer film formed from crosslinked colloids resembles the films formed from non crosslinked colloids at low temperature (for instance lower than glass transition temperature of polymers). In both cases, the interface diffusion of polymer chains is limited due to their restricted mobility. In the future, the correlation between film formation temperature and the *Young's* modulus of the corresponding film could be studied by utilizing micromechanical cantilevers. I would expect a lower *Young's* modulus for PS film formed at temperature lower than the annealing temperature (220°C) used in this thesis. By varying the film formation conditions, polymer films with different mechanical properties could be generated and characterized by cantilevers simultaneously.

By plotting the *Young's* modulus of the film as a function of temperature, the glass transition temperature of the homogenous film can also be estimated. The *Young's* modulus changes dramatically during glass transition. Here, the glass transition temperature T_g of PS with a molecular weight of 20 kg/mol has been observed at 150 °C, which is about 40°C higher than T_g of PS estimated by differential scanning calorimetry. The increase of T_g is a consequence of the high operation frequency of the cantilever (~12 kHz). The resonance frequency of cantilevers can vary from a few thousand Hertz to a few hundred thousand Hertz, depending on their geometry, mainly on the thickness of the cantilever. Measuring T_g at different resonance frequencies might enable better insight into the interdependence between T_g and the resonance frequency in the future. This investigation would be of great interest regarding the application of polymer films as coating layers under different conditions.

I also see a potential for applying a micromechanical cantilever to investigate the *Young's* modulus and the glass transition temperature of polymer thin films as a function of their thickness. For this purpose, the size of the colloids can be varied to generate polymer films of different predefined thicknesses. There is still intense interest in characterizing and understanding the correlation between the *Young's* modulus, glass transition temperature and polymer film thickness.[123]

9.3 Application of Polymeric Functionalized Cantilevers as Sensors

The deflection of functionalized cantilevers due to binding of target molecules into an active layer can be used as positive feedback for sensing applications. I have used a micromechanical cantilever coated with grafted PNIPAAM-PBA brushes as a glucose sensor. The preliminary experiments carried out in this thesis showed a promising potential of functionalized cantilevers as sensors (chapter 7). The cantilever functionalized with PNIPAAM-PBA brushes bent upon exposure to a solution containing glucose at lower of 50 mM. In addition, the deflection of the cantilever coated with PNIPAAM-PBA was twice as large as that of a cantilever functionalized with self-assembled monolayers (SAM) of MPBA. This result confirms the advantages of using polymer grafted cantilevers as sensors as compared to using SAM functionalized cantilevers. Hence, the target molecules can be detected at even lower concentration. For instance with glucose concentrations of approximately 10 mM, which is a typical concentration of glucose in human blood.[124]

Also, the effect of temperature on the micromechanical cantilever sensor should be investigated at physiologically relevant conditions. As reported by Bradley et al[109] the PNIPAAM brushes did not bend the cantilever in swollen state, but rather bent cantilever after the brushes collapse. It will be interesting to study whether the collapsed PNIPAAM can amplify the deflection of cantilever upon glucose binding as compared to the swollen PNIPAAM (Figure 84).

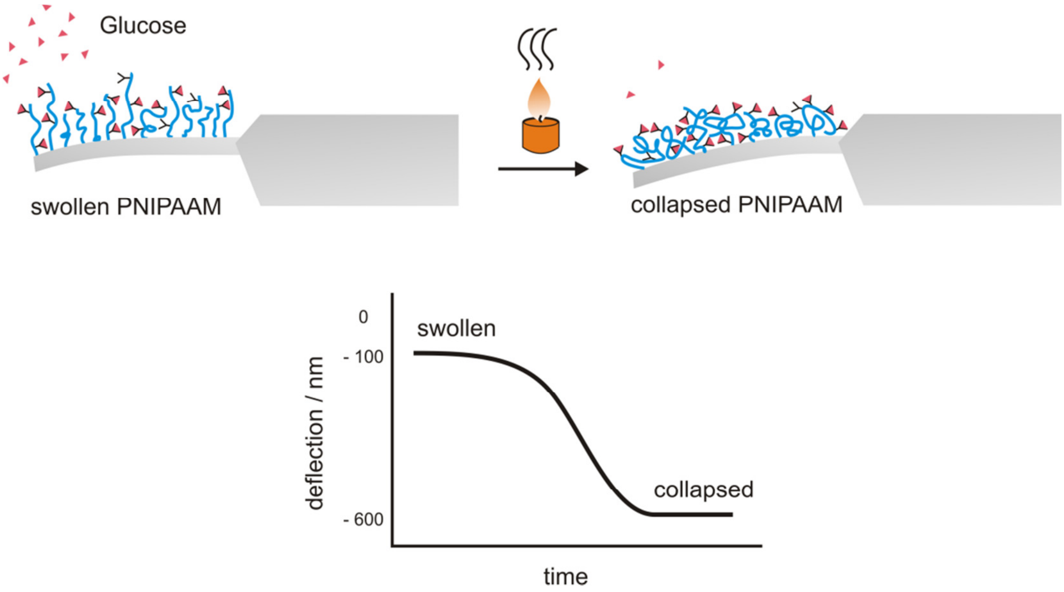

Figure 84: Sketch of the transition of PNIPAAM-PBA from swollen state to collapsed state after binding of glucose by increase the temperature of the solution (illustrated by the candle). The deflection should increase due to the bimetal effect between the collapsed PNIPAAM and cantilever.[109]

10 Reference

[1] I. W. Hamley, *Introduction to Soft Matter* **2007**.

[2] R. A. L. Jones, *Soft Condensed Matter* **2002**.

[3] N. C. Seeman, *Journal of Theoretical Biology* **1982**, *99*, 237.

[4] N. C. Seeman, *Trends in Biotechnology* **1999**, *17*, 437.

[5] F. E. Alemdaroglu, A. Herrmann, *Organic & Biomolecular Chemistry* **2007**, *5*, 1311.

[6] a)D. E. Discher, A. Eisenberg, *Science* **2002**, *297*, 967; b)S. Forster, V. Abetz, A. H. E. Muller, in *Polyelectrolytes with Defined Molecular Architecture Ii, Vol. 166*, Springer-Verlag Berlin, Berlin, **2004**, pp. 173; c)E. A. Simone, T. D. Dziubla, V. R. Muzykantov, *Expert Opinion on Drug Delivery* **2008**, *5*, 1283.

[7] a)Z. Li, Y. Zhang, P. Fullhart, C. A. Mirkin, *Nano Letters* **2004**, *4*, 1055; b)K. Ding, *Dissertation Thesis* **2006**; c)K. Ding, F. E. Alemdaroglu, M. Boersch, R. Berger, A. Herrmann, *Angewandte Chemie-International Edition* **2007**, *46*, 1172; d)J. Wang, F. E. Alemdaroglu, D. K. Prusty, A. Herrmann, R. Berger, *Macromolecules* **2008**, *41*, 2914.

[8] B. Tinland, A. Pluen, J. Sturm, G. Weill, *Macromolecules* **1997**, *30*, 5763.

[9] S. Brinkers, H. R. C. Dietrich, F. H. de Groote, I. T. Young, B. Rieger, *Journal of Chemical Physics* **2009**, *130*.

[10] F. E. Alemdaroglu, J. Wang, M. Borsch, R. Berger, A. Herrmann, *Angewandte Chemie-International Edition* **2008**, *47*, 974.

[11] F. E. Alemdaroglu, K. Ding, R. Berger, A. Herrmann, *Angew. Chem. Int. Ed.* **2006**, *45*, 4206.

[12] a)J. H. Jeong, S. W. Kim, T. G. Park, *Bioconjugate Chemistry* **2003**, *14*, 473; b)J. H. Jeong, S. W. Kim, T. G. Park, *Journal of Controlled Release* **2003**, *93*, 183; c)Y. H. Bae, T. Okano, R. Hsu, S. W. Kim, *Makromolekulare Chemie-Rapid Communications* **1987**, *8*, 481.

[13] M. D. Costioli, I. Fisch, F. Garret-Flaudy, F. Hilbrig, R. Freitag, *Biotechnology and Bioengineering* **2003**, *81*, 535.

[14] G. Tong, J. M. Lawlor, G. W. Tregear, J. Haralambidis, *Journal of Organic Chemistry* **1993**, *58*, 2223.

[15] F. Wurthner, A. Sautter, *Chemical Communications* **2000**, 445.

[16] E. A. G. Aniansson, S. N. Wall, M. Almgren, H. Hoffmann, I. Kielmann, W. Ulbricht, R. Zana, J. Lang, C. Tondre, *Journal of Physical Chemistry* **1976**, *80*, 905.

[17] S. Creutz, J. vanStam, S. Antoun, F. C. DeSchryver, R. Jerome, *Macromolecules* **1997**, *30*, 4078.

[18] G. Riess, *Progress in Polymer Science* **2003**, *28*, 1107.

[19] a)N. Abedinov, C. Popov, Z. Yordanov, T. Ivanov, T. Gotszalk, P. Grabiec, W. Kulisch, I. W. Rangelow, D. Filenko, Y. Shirshov, *Journal of Vacuum Science & Technology B* **2003**, *21*, 2931; b)M. K. Baller, H. P. Lang, J. Fritz, C. Gerber, J. K. Gimzewski, U. Drechsler, H. Rothuizen, M. Despont, P. Vettiger, F. M. Battiston, J. P. Ramseyer, P. Fornaro, E. Meyer, H. J. Guntherodt, *Ultramicroscopy* **2000**, *82*, 1; c)J. Fritz, *Analyst* **2008**, *133*, 855; d)H. P. Lang, M. K. Baller, R. Berger, C. Gerber, J. K. Gimzewski, F. M. Battiston, P. Fornaro, J. P. Ramseyer, E. Meyer, H. J. Guntherodt, *Analytica Chimica Acta* **1999**, *393*, 59.

[20] a)T. Y. Kwon, Y. B. Kim, K. Eom, D. S. Yoon, H. L. Lee, T. S. Kim, *Applied Physics a-Materials Science & Processing* **2007**, *88*, 627; b)H. Muro, H. Kaneko, S. Kiyota, P. J. French, *Sensors and Actuators a-Physical* **1992**, *34*, 43.

[21] N. L. Privorotskaya, W. P. King, *Microsystem Technologies-Micro-and Nanosystems-Information Storage and Processing Systems* **2009**, *15*, 333.

[22] a)S. Lenz, S. K. Nett, M. Memesa, R. F. Roskamp, A. Timmann, S. V. Roth, R. Berger, J. S. Gutmann, *Macromolecules* **2010**, *43*, 1108; b)A. Bietsch, J. Y. Zhang, M. Hegner, H. P. Lang, C. Gerber, *Nanotechnology* **2004**, *15*, 873.

[23] a)K. Landfester, *Macromolecular Rapid Communications* **2001**, *22*, 896; b)K. Landfester, *Annual Review of Materials Research* **2006**, *36*, 231.

[24] W. D. Harkins, *Journal of the American Chemical Society* **1947**, *69*, 1428.

[25] N. D. Denkov, O. D. Velev, P. A. Kralchevsky, I. B. Ivanov, H. Yoshimura, K. Nagayama, *Langmuir* **1992**, *8*, 3183.

[26] a)J. Aizenberg, P. V. Braun, P. Wiltzius, *Physical Review Letters* **2000**, *84*, 2997; b)P. A. Kralchevsky, N. D. Denkov, *Current Opinion in Colloid & Interface Science* **2001**, *6*, 383; c)P. A. Kralchevsky, K. Nagayama, *Langmuir* **1994**, *10*, 23.

[27] M. A. Winnik, *Current Opinion in Colloid & Interface Science* **1997**, *2*, 192.

[28] D. Magde, W. W. Webb, E. Elson, *Physical Review Letters* **1972**, *29*, 705.

[29] a)M. Kinjo, R. Rigler, *Nucleic Acids Research* **1995**, *23*, 1795; b)N. G. Walter, P. Schwille, M. Eigen, *Proceedings of the National Academy of Sciences of the United States of America* **1996**, *93*, 12805.

[30] B. Rauer, E. Neumann, J. Widengren, R. Rigler, in *ZiF-Workshop and Poster Sessions on Dynamics of Polyelectrolytes, Colloids and Interfaces - Electro-optical Methods in (Bio-)Technology and Medicine (Electro-opto 94)*, Elsevier Science Bv, Bielefeld, Germany, **1994**, pp. 3.

[31] a)R. Rigler, A. Pramanik, P. Jonasson, G. Kratz, O. T. Jansson, P. A. Nygren, S. Stahl, K. Ekberg, B. L. Johansson, S. Uhlen, M. Uhlen, H. Jornvall, J. Wahren, *Proceedings of the National Academy of Sciences of the United States of America* **1999**, *96*, 13318; b)M. Henriksson, A. Pramanik, J. Shafqat, Z. H. Zhong, M. Tally, K. Ekberg, J. Wahren, R. Rigler, J. Johansson, H. Jornvall, *Biochemical and Biophysical Research Communications* **2001**, *280*, 423.

[32] P. Liu, T. Sudhaharan, R. M. L. Koh, L. C. Hwang, S. Ahmed, I. N. Maruyama, T. Wohland, *Biophysical Journal* **2007**, *93*, 684.

[33] a)T. B. Bonne, K. Ludtke, R. Jordan, C. M. Papadakis, *Macromolecular Chemistry and Physics* **2007**, *208*, 1402; b)T. B. Bonne, K. Ludtke, R. Jordan, P. Stepanek, C. M. Papadakis, *Colloid and Polymer Science* **2004**, *282*, 833.

[34] K. Troll, A. Kulkarni, W. Wang, C. Darko, A. M. B. Koumba, A. Laschewsky, P. Muller-Buschbaum, C. M. Papadakis, *Colloid and Polymer Science* **2008**, *286*, 1079.

[35] H. T. Chen, S. W. Kim, L. Li, S. Y. Wang, K. Park, J. X. Cheng, *Proceedings of the National Academy of Sciences of the United States of America* **2008**, *105*, 6596.

[36] R. Leung, D. O. Shah, *Journal of Colloid and Interface Science* **1986**, *113*, 484.

[37] M. Borsch, P. Turina, C. Eggeling, J. R. Fries, C. A. M. Seidel, A. Labahn, P. Graber, *Febs Letters* **1998**, *437*, 251.

[38] K. Koynov, G. Mihov, M. Mondeshki, C. Moon, H. W. Spiess, K. Mullen, H. J. Butt, G. Floudas, *Biomacromolecules* **2007**, *8*, 1745.

[39] R. Rigler, Z. Foldes-Papp, F. J. Meyer-Alme, C. Sammet, M. Volcker, A. Schnetz, *Journal of Biotechnology* **1998**, *63*, 97.

[40] G. Binnig, C. F. Quate, C. Gerber, *Physical Review Letters* **1986**, *56*, 930.

[41] R. Garcia, R. Perez, *Surface Science Reports* **2002**, *47*, 197.

[42] J. K. Gimzewski, C. Gerber, E. Meyer, R. R. Schlittler, *Chemical Physics Letters* **1994**, *217*, 589.

[43] T. Thundat, R. J. Warmack, G. Y. Chen, D. P. Allison, *Applied Physics Letters* **1994**, *64*, 2894.

[44] a)H. J. Butt, *Journal of Colloid and Interface Science* **1996**, *180*, 251; b)G. Y. Chen, T. Thundat, E. A. Wachter, R. J. Warmack, *Journal of Applied Physics* **1995**, *77*, 3618; c)R. Berger, E. Delamarche, H. P. Lang, C. Gerber, J. K. Gimzewski, E. Meyer, H. J. Guntherodt, *Science* **1997**, *276*, 2021.

[45] G. Y. Chen, R. J. Warmack, T. Thundat, D. P. Allison, A. Huang, *Review of Scientific Instruments* **1994**, *65*, 2532.

[46] a)M. Alvarez, L. G. Carrascosa, M. Moreno, A. Calle, A. Zaballos, L. M. Lechuga, C. Martinez-A, J. Tamayo, *Langmuir* **2004**, *20*, 9663; b)J. Fritz, M. K. Baller, H. P. Lang, H. Rothuizen, P. Vettiger, E. Meyer, H. J. Guntherodt, C. Gerber, J. K. Gimzewski, *Science* **2000**, *288*, 316; c)G. H. Wu, H. F. Ji, K. Hansen, T. Thundat, R. Datar, R. Cote, M. F. Hagan, A. K. Chakraborty, A. Majumdar, *Proceedings of the National Academy of Sciences of the United States of America* **2001**, *98*, 1560.

[47] R. McKendry, J. Y. Zhang, Y. Arntz, T. Strunz, M. Hegner, H. P. Lang, M. K. Baller, U. Certa, E. Meyer, H. J. Guntherodt, C. Gerber, *Proceedings of the National Academy of Sciences of the United States of America* **2002**, *99*, 9783.

[48] P. Vettiger, J. Brugger, M. Despont, U. Drechsler, U. Durig, W. Haberle, M. Lutwyche, H. Rothuizen, R. Stutz, R. Widmer, G. Binnig, *Microelectronic Engineering* **1999**, *46*, 11.

[49] G. G. Bumbu, M. Wolkenhauer, G. Kircher, J. S. Gutmann, R. Berger, *Langmuir* **2007**, *23*, 2203.

[50] H.-J. Butt, B. Cappella, M. Kappl, *Surf. Sci. Rep.* **2005**, *59*, 1.

[51] R. Raiteri, H. J. Butt, *Journal of Physical Chemistry* **1995**, *99*, 15728.

[52] G. G. Stoney, *Proceedings of the Royal Society of London Series a-Containing Papers of a Mathematical and Physical Character* **1909**, *82*, 172.

[53] a)C. A. Klein, *Journal of Applied Physics* **2000**, *88*, 5487; b)J. D. Schafer, H. Nafe, F. Aldinger, *Journal of Applied Physics* **1999**, *85*, 8023.

[54] M. J. Wenzel, F. Josse, S. M. Heinrich, E. Yaz, P. G. Datskos, *Journal of Applied Physics* **2008**, *103*.

[55] Y. Geng, P. Dalhaimer, S. S. Cai, R. Tsai, M. Tewari, T. Minko, D. E. Discher, *Nature Nanotechnology* **2007**, *2*, 249.

[56] F. E. Alemdaroglu, N. C. Alemdaroglu, P. Langguth, A. Herrmann, *Macromolecular Rapid Communications* **2008**, *29*, 326.

[57] M. A. Abdalla, J. Bayer, J. O. Radler, K. Mullen, *Angewandte Chemie-International Edition* **2004**, *43*, 3967.

[58] a)F. Wurthner, *Chemical Communications* **2004**, 1564; b)S. Bevers, S. Schutte, L. W. McLaughlin, *Journal of the American Chemical Society* **2000**, *122*, 5905; c)E. A. Meyer, R. K. Castellano, F. Diederich, *Angewandte Chemie-International Edition* **2003**, *42*, 1210; d)J. C. Nelson, J. G. Saven, J. S. Moore, P. G. Wolynes, *Science* **1997**, *277*, 1793; e)C. Wagner, H. A. Wagenknecht, *Organic Letters* **2006**, *8*, 4191; f)W. Wang, W. Wan, H. H. Zhou, S. Q. Niu, A. D. Q. Li, *Journal of the American Chemical Society* **2003**, *125*, 5248.

[59] D. Baumstark, H. A. Wagenknecht, *Chemistry-a European Journal* **2008**, *14*, 6640.

[60] M. Mandelkern, J. G. Elias, D. Eden, D. M. Crothers, *Journal of Molecular Biology* **1981**, *152*, 153.

[61] a)M. C. Murphy, I. Rasnik, W. Cheng, T. M. Lohman, T. Ha, *Biophys. J* **2004**, *86*, 2530; b)S. B. Smith, Y. Cui, C. Bustamante, *Science* **1996**, *271*, 795; c)W. K. Olson, *Macromolecules* **1975**, *8*, 272.

[62] a)D. F. Siqueira, S. P. Nunes, B. A. Wolf, *Macromolecules* **1994**, *27*, 4561; b)G. Wanka, H. Hoffmann, W. Ulbricht, *Macromolecules* **1994**, *27*, 4145.

[63] T. Cherdhirankorn, A. Best, K. Koynov, K. Peneva, K. Muellen, G. Fytas, *Journal of Physical Chemistry B* **2009**, *113*, 3355.

[64] P. Schwille, I. Hausstein.

[65] J. Wang, *Dissertation Thesis* **2008**.

[66] K. Mortensen, *J. Phys.* **1996**, *A*, 103.

[67] E. B. Cho, D. Kim, *Macromolecular Symposia* **2007**, *249*, 437.

[68] a)M. Maute, S. Raible, F. E. Prins, D. P. Kern, U. Weimar, W. Gopel, *Microelectronic Engineering* **1999**, *46*, 439; b)B. H. Kim, F. E. Prins, D. P. Kern, S. Raible, U. Weimar, *Sensors and Actuators B-Chemical* **2001**, *78*, 12; c)D. Lange, C. Hagleitner, A. Hierlemann, O. Brand, H. Baltes, *Analytical Chemistry* **2002**, *74*, 3084.

[69] a)N. Jung, H. Seo, D. Lee, C. Y. Ryu, S. Jeon, *Macromolecules* **2008**, *41*, 6873; b)J. H. Zhao, M. Kiene, C. Hu, P. S. Ho, *Applied Physics Letters* **2000**, *77*, 2843.

[70] N. Jung, S. Jeon, *Macromolecules* **2008**, *41*, 9819.

[71] S. Igarashi, A. N. Itakura, M. Toda, M. Kitajima, L. Chu, A. N. Chifene, R. Forch, R. Berger, *Sensors and Actuators B-Chemical* **2006**, *117*, 43.

[72] T. Thundat, S. L. Sharp, W. G. Fisher, R. J. Warmack, E. A. Wachter, *Applied Physics Letters* **1995**, *66*, 1563.

[73] T. M. Mayer, M. P. de Boer, N. D. Shinn, P. J. Clews, T. A. Michalske, *Journal of Vacuum Science & Technology B* **2000**, *18*, 2433.

[74] E. A. Beam, Y. C. Kao, J. Y. Yang, *Applied Physics Letters* **1991**, *58*, 152.

[75] C. D. Bain, G. M. Whitesides, *Journal of the American Chemical Society* **1989**, *111*, 7164.

[76] G. G. Bumbu, G. Kircher, M. Wolkenhauer, R. Berger, J. S. Gutmann, *Macromolecular Chemistry and Physics* **2004**, *205*, 1713.

[77] T. Shimoda, K. Morii, S. Seki, H. Kiguchi, *Mrs Bulletin* **2003**, *28*, 821.

[78] S. Ugur, A. Elaissari, O. Pekcan, *Journal of Colloid and Interface Science* **2003**, *263*, 674.

[79] a)E. Arda, S. Kara, A. Sarac, O. Pekcan, *Journal of Colloid and Interface Science* **2006**, *297*, 520; b)D. Juhue, J. Lang, *Macromolecules* **1994**, *27*, 695.

[80] M. Retsch, *Dissertation Thesis* **2009**.

[81] M. Retsch, Z. C. Zhou, S. Rivera, M. Kappl, X. S. Zhao, U. Jonas, Q. Li, *Macromolecular Chemistry and Physics* **2009**, *210*, 230.

[82] M. Fujii, S. Sugisawa, K. Fukada, T. Kato, T. Shirakawa, T. Seimiya, *Langmuir* **1994**, *10*, 984.

[83] a)J. H. Zhang, Y. F. Li, X. M. Zhang, B. Yang, *Advanced Materials* **2010**, *22*, 4249; b)A. Plettl, F. Enderle, M. Saitner, A. Manzke, C. Pfahler, S. Wiedemann, P. Ziemann, *Advanced Functional Materials* **2009**, *19*, 3279.

[84] Y. C. Wang, M. A. Winnik, *Journal of Physical Chemistry* **1993**, *97*, 2507.

[85] a)D. K. Yi, U. Paik, *Journal of Nanoscience and Nanotechnology* **2010**, *10*, 4943; b)E. Harel, S. E. Meltzer, A. A. G. Requicha, M. E. Thompson, B. E. Koel, *Nano Letters* **2005**, *5*, 2624.

[86] G. Strobl, *The Physics of Polymers* **1996-1997**.

[87] C. E. Wilkes, J. W. Summers, C. A. Daniels, *PVC Handbook* **2005**.

[88] a)R. D. Andrews, J. F. Rudd, *Journal of Applied Physics* **1957**, *28*, 1091; b)J. F. Rudd, E. F. Gurnee, *Journal of Applied Physics* **1957**, *28*, 1096.

[89] S. Nayak, L. A. Lyon, *Angewandte Chemie-International Edition* **2005**, *44*, 7686.

[90] a)R. Pelton, *Advances in Colloid and Interface Science* **2000**, *85*, 1; b)V. Nerapusri, J. L. Keddie, B. Vincent, I. A. Bushnak, *Langmuir* **2006**, *22*, 5036; c)L. G. Guerrero-Ramirez, S. M. Nuno-Donlucas, L. C. Cesteros, I. Katime, *Materials Chemistry and Physics* **2008**, *112*, 1088.

[91] a)M. J. Serpe, K. A. Yarmey, C. M. Nolan, L. A. Lyon, *Biomacromolecules* **2005**, *6*, 408; b)K. Kataoka, H. Miyazaki, M. Bunya, T. Okano, Y. Sakurai, *Journal of the American Chemical Society* **1998**, *120*, 12694.

[92] W. Kangwansupamonkon, S. Damronglerd, S. Kiatkamjornwong, *Journal of Applied Polymer Science* **2002**, *85*, 654.

[93] a)A. Zosel, G. Ley, *Macromolecules* **1993**, *26*, 2222; b)J. W. Taylor, M. A. Winnik, *Jct Research* **2004**, *1*, 163.

[94] S. Pickup, F. D. Blum, W. T. Ford, M. Periyasamy, *Journal of the American Chemical Society* **1986**, *108*, 3987.

[95] T. P. Gall, E. J. Kramer, *Polymer* **1991**, *32*, 265.

[96] K. M. Kruger, G. Sadowski, *Macromolecules* **2005**, *38*, 8408.

[97] P. J. McDonald, J. Godward, R. Sackin, R. P. Sear, *Macromolecules* **2001**, *34*, 1048.

[98] a)J. S. Vrentas, J. L. Duda, *Journal of Polymer Science Part B-Polymer Physics* **1977**, *15*, 441; b)S. A. Stern, H. L. Frisch, *Annual Review of Materials Science* **1981**, *11*, 523.

[99] Z. Y. Ding, J. J. Aklonis, R. Salovey, *Journal of Polymer Science Part B-Polymer Physics* **1991**, *29*, 1035.

[100] A. Laschitsch, C. Bouchard, J. Habicht, M. Schimmel, J. Ruhe, D. Johannsmann, *Macromolecules* **1999**, *32*, 1244.

[101] F. Mueller, B. Heuwers, F. Katzenberg, J. C. Tiller, G. Sadowskit, *Macromolecules* **2010**, *43*, 8997.

[102] J. M. Torres, C. M. Stafford, B. D. Vogt, *Acs Nano* **2010**, *4*, 5357.

[103] M. Lahav, C. Durkan, R. Gabai, E. Katz, I. Willner, M. E. Welland, *Angewandte Chemie-International Edition* **2001**, *40*, 4095.

[104] V. Tabard-Cossa, M. Godin, P. Grutter, I. Burgess, R. B. Lennox, *Journal of Physical Chemistry B* **2005**, *109*, 17531.

[105] F. Zhou, P. M. Biesheuvel, E. Y. Chol, W. Shu, R. Poetes, U. Steiner, W. T. S. Huck, *Nano Letters* **2008**, *8*, 725.

[106] D. E. Bergbreiter, B. L. Case, Y. S. Liu, J. W. Caraway, *Macromolecules* **1998**, *31*, 6053.

[107] a)R. B. Fong, Z. L. Ding, C. J. Long, A. S. Hoffman, P. S. Stayton, *Bioconjugate Chemistry* **1999**, *10*, 720; b)Q. He, A. Kueller, S. Schilp, F. Leisten, H. A. Kolb, M. Grunze, J. B. Li, *Small* **2007**, *3*, 1860; c)T. Chen, J. M. Zhang, D. P. Chang, A. Garcia, S. Zauscher, *Advanced Materials* **2009**, *21*, 1825 ; d)S. J. Ahn, M. Kaholek, W. K. Lee, B. LaMattina, T. H. LaBean, S. Zauscher, *Advanced Materials* **2004**, *16*, 2141.

[108] N. I. Abu-Lail, M. Kaholek, B. LaMattina, R. L. Clark, S. Zauscher, *Sensors and Actuators B-Chemical* **2006**, *114*, 371.

[109] C. Bradley, N. Jalili, S. K. Nett, L. Q. Chu, R. Forch, J. S. Gutmann, R. Berger, *Macromolecular Chemistry and Physics* **2009**, *210*, 1339.

[110] K. Kataoka, H. Miyazaki, T. Okano, Y. Sakurai, *Macromolecules* **1994**, *27*, 1061.

[111] X. Yin, A. S. Hoffman, P. S. Stayton, *Biomacromolecules* **2006**, *7*, 1381.

[112] a)S. A. Asher, V. L. Alexeev, A. V. Goponenko, A. C. Sharma, I. K. Lednev, C. S. Wilcox, D. N. Finegold, *Journal of the American Chemical Society* **2003**, *125*, 3322; b)C. W. Gray, T. A. Houston, *Journal of Organic Chemistry* **2002**, *67*, 5426; c)V. V. Karnati, X. M. Gao, S. H. Gao, W. Q. Yang, W. J. Ni, S. Sankar, B. H. Wang, *Bioorganic & Medicinal Chemistry Letters* **2002**, *12*, 3373; d)A. Kikuchi, K. Suzuki, O. Okabayashi, H. Hoshino, K. Kataoka, Y. Sakurai, T. Okano, *Analytical Chemistry* **1996**, *68*, 823; e)A. Matsumoto, R. Yoshida, K. Kataoka, *Biomacromolecules* **2004**, *5*, 1038; f)A. J. Tong, A. Yamauchi, T. Hayashita, Z. Y. Zhang, B. D. Smith, N. Teramae, *Analytical Chemistry* **2001**, *73*, 1530.

[113] Y. Kanekiyo, M. Sano, R. Iguchi, S. Shinkai, *Journal of Polymer Science Part a-Polymer Chemistry* **2000**, *38*, 1302.

[114] G. Gerald, G. Margarita, S. Gunnar, S. Joerg, A. Karl-Friedrich, R. Andreas, *Macromolecular Symposia* **2004**, *210*, 403.

[115] a)T. Hoare, R. Pelton, *Macromolecules* **2007**, *40*, 670; b)F. Xia, H. Ge, Y. Hou, T. L. Sun, L. Chen, G. Z. Zhang, L. Jiang, *Advanced Materials* **2007**, *19*, 2520.

[116] D. M. Anaya, *Dissertation Thesis* **2010**.

[117] a)F. H. C. Crick, A. Klug, *Nature* **1975**, *255*, 530; b)M. Levitt, *Proceedings of the National Academy of Sciences of the United States of America* **1978**, *75*, 640.

[118] M. Borsch, P. Turina, C. Eggeling, J. R. Fries, C. A. M. Seidel, A. Labahn, P. Graber, *FEBS Lett.* **1998**, *437*, 251.

[119] K. L. Wang, X. Qiu, C. Q. Dong, J. C. Ren, *Chembiochem* **2007**, *8*, 1126.

[120] F. K. Hansen, J. Ugelstad, *Journal of Polymer Science Part a-Polymer Chemistry* **1978**, *16*, 1953.

[121] A. Eshuis, H. J. Leendertse, D. Thoenes, *Colloid and Polymer Science* **1991**, *269*, 1086.

[122] T. Chen, D. P. Chang, T. Liu, R. Desikan, R. Datar, T. Thundat, R. Berger, S. Zauscher, *Journal of Materials Chemistry* **2010**, *20*, 3391.

[123] a)C. J. Ellison, J. M. Torkelson, *Nature Materials* **2003**, *2*, 695; b)Z. Ao, S. Li, *Nanoscale Research Letters* **2011**, *6*.

[124] a)S. A. Jaffari, A. P. F. Turner, *Physiological Measurement* **1995**, *16*, 1; b)E. Wilkins, P. Atanasov, B. A. Muggenburg, *Biosensors & Bioelectronics* **1995**, *10*, 485.

List of Publications

Ting Liu, Sascha Pihan, Marcel Roth, Rüdiger Berger, Hans-Jürgen Butt, Micromechanical cantilever sensors coated with colloidal monolayers of nanoparticles, in preparation.

Milena Anaya, Ting Liu, Jia Gao, Carla Spagnuolo, Jie Wang, Maria A. Loi, Kaloian Koynov, Rüdiger Berger,Klaus Müllen and Andreas Herrmann, Dye system induce aggregation of DNA nanostructures, in preparation.

Tao Chen, Debby P. Chang, Ting Liu, Ramya Desikan, Ram Datar, Thomas Thundat, Rüdiger Berger and Stefan Zauscher, Glucose-Responsive Polymer Brushes for Microcantilever Sensing, *Journal of Materials Chemistry* **2010**, *20*, 3391, published.

Conference Contribution

Ting Liu, Jie Wang, Ke Ding, Milena Anaya, Carla Spagnvolo, Deepak K. Prusty, Andreas Herrmann, Klaus Müllen, Hans-Jürgen Butt, Kaloian Koynov, Rüdiger Berger; Investigation of aggregates formed by amphiphilic DNA block copolymers and DNA templates; poster presentation at 5. Zsigmondy Kolloquium 2009, Bayreuth.

Ting Liu, Tao Chen, Debby P. Chang, Ramya Desikan, Thomas Thundat, Ram Datar, Rüdiger Bergerand Stefan Zauscher;Micromechanical cantilever array for glucose sensing; poster presentation at nanomechanical cantilever workshop 2010, Banff.

Ting Liu, Hans-Jürgen Butt, Rüdiger Berger; Asymmetrical deposition of polystyrene colloidal monolayerand study of interaction between interfaces; poster presentation at nanomechanical cantilever workshop 2010, Banff.

List of Abbreviations

A	adenine
C	cytosine
CMC	critical micelle concentration
DNA	deoxyribonucleic acid
DLS	dynamic light scattering
ds	double stranded
FCS	fluorescence correlation spectroscopy
FCCS	fluorescence cross-correlation spectroscopy
FRET	fluorescenceresonance energy transfer
G	guanine
LCST	lower critical solution temperature
MFC	mass flow controller
M_w	molecular weight
ODN	oligodeoxynucleotide
PBA	phenyl boronic acid
PDI	perylenediimide
PNIPAAM	poly(N-isopropylacrylamide)
PS	polystyrene
PPO	polypropylene oxide

RF	resonance frequency
Rh6G	Rhodamine 6G
SAM	self-assembled monolayers
SEM	scanning electron microscopy
SFM	scanning force microscopy
SLS	static light scattering
ss	single stranded
T	Thymine
T_g	glass transition temperature
TGA	thermal gravimetric analysis
Tris	tris(hydroxymethyl)aminomethane